Characterizing a dc-SQUID and a Mo/TiW/Cu -trilayer transition-edge sensor array

Author:

ARI HELENIUS

Supervisors:

ILARI MAASILTA AND KIMMO KINNUNEN

JYVÄSKYLÄN YLIOPISTO
FYSIIKAN LAITOS

Abstract

A new superconducting quantum interference device and a transition-edge sensor from a 256 pixel chip was characterized in this thesis. In order to reach superconducting transition the components need extremely low temperatures and shielding from high magnetic fields. Important quantities measured were the amplification factor and the noise floor of the superconducting quantum interference device and the transition temperature, the normal state resistance, the current-voltage-characteristics, and the noise of the transition-edge sensor. The motivation for this research was to find the sensitivity limits of the measurement system and fit a theoretical model to better understand the noise properties of the transition-edge sensor. A unified theory is not yet determined for the high frequency noise, but there are a few different models.

Tiivistelmä

Helenius, Ari
DC-SQUID:n ja Mo/TiW/Cu -kolmikerros transitioreunailmiaisimin matriisin karakterisointi
Pro Gradu-tutkielma
Fysiikan laitos, Jyväskylän yliopisto, 2017, 97 sivua

Tutkielmassa määritettiin uuden suprajohtavan kvantti-interferenssilaitteen ja 256 pikseliä sisältävän sirun transitioreunailmaisimien ominaisuuksia. Komponentit vaativat erittäin matalia lämpötiloja ja suojauksen suurilta magneettikentiltä muuttuakseen suprajohtaviksi. Tärkeimmät mitatut ominaisuudet olivat suprajohtavan kvantti-interferenssilaitteen signaalin vahvistuskerroin sekä kohina ja transitioreunailmaisimen transitiolämpötila, normaalitilan vastus, virta-jännite-käyttäytyminen, sekä kohina. Motivaationa tutkimukselle oli etsiä käytetyn mittalaite kokonaisuuden herkkyyden rajat sekä pyrkiä sovittamaan teoreettista mallia transitioreunailmaisimen kohinan ymmärtämiseksi. Korkean taajuuden kohinassa on käytössä erilaisia olettamuksia, mutta yhtenäistä teoriaa ei ole vielä yleisesti hyväksytty.

Avainsanat: Transitioreunailmaisin, TES, Suprajohtava kvantti-interferenssilaite, SQUID

Preface

The research reported in this Master's thesis has been done between September 2016 and July 2017 at Nanoscience Center, University of Jyväskylä.

First, I would like to thank my supervisor Professor Ilari Maasilta for the theoretical advice and giving me the opportunity to research this interesting topic under his experimental nanophysics group. I also would like to thank my supervisor Dr. Kimmo Kinnunen as well as Mr. Tarmo Suppula for their help and advice with low temperature measurements. The working atmosphere and the facilities as well as the group members and other staff at Nanoscience Center has made this experience enjoyable, for which I'm thankful of.

Finally, this project was also made possible by the superconducting quantum interference devices provided by National Institute of Standards and Technology (NIST, Boulder) and the transition-edge sensors acquired from an earlier collaboration between Professor Ilari Maasilta and VTT Technical Research Centre of Finland Ltd (VTT, Micronova, Espoo).

Jyväskylä, 20.11.2017
Ari Helenius

Contents

1 Introduction

Superconductors have been a subject of interest ever since Kamerlingh Onnes found that mercury loses all electrical resistance when cooled down to liquid helium temperatures [1]. In the following decades many new superconducting materials have been found, some of them with high transition temperatures T_c. While having more easily achieved operating temperatures, the high transition temperature superconductors and radiation detectors made out of these materials are not sensitive enough to achieve the theoretical limits of the low T_c superconducting detectors [2, 3]. For superconducting detectors it took quite a few years to surpass the sensitivity of semiconductor detectors. Even to this day the difficulty using superconducting detectors is the readout system rather than the manufacturing of large scale arrays [3]. Using superconducting quantum interference devices (SQUID) as the readout of large superconducting transition-edge sensor (TES) arrays has become more feasible. The problem in the readout is not the amount of components, TESs and SQUIDs, but the increased complexity, cost and power load from wiring if every pixel has its own SQUID readout. SQUID multiplexing, time division, frequency division or code division multiplexing, has increased the number of TES pixels per SQUID [3]. The number of TES bolometers per readout chain for a current project SPICA Safari is planned to be 160, for a total of 4100-6400 pixels [4] and the number of x-ray TESs for ATHENA satellite mission is planned to be 40 pixels per SQUID, for a total of 3600 pixels [5]. Lastly a hybrid based multiplexing scheme could be used to read out in total in the 100,000-pixel-range for microcalorimeters [3].

The principles of the SQUIDs were hypothetized by Josephson [6] by the theoretical introduction of the Josephson effect in superconducting tunneling junctions. In the paper it was shown that there is a finite possibility for the supercurrent to tunnel through a superconductor-insulator-superconductor junction. The SQUID is a very sensitive magnetic field flux detector, and if coupled to an input coil, it can be used to measure very small changes in input circuit current, which the input coil transforms into magnetic flux through the SQUID. The supercurrent through the SQUID is dependent on the flux through it, and the change of the total current through the SQUID can be measured as a voltage drop across the SQUID when the SQUID is biased. There are two kinds of SQUIDs, the dc-SQUID and the radiofrequency (rf)-SQUID. The main difference physically is that the dc-SQUID is made of two Josephson junctions in parallel, connected to a biasing and readout circuit, while the rf-SQUID is only made of one junction in a closed superconducting loop coupled to an rf-readout circuit. Both of the SQUIDs have their strengths and can be used as highly sensitive gradiometers and magnetometers, with high and low Tc

superconductors [7], and have applications in biological studies [8], brain activity studies [9] and as TES signal amplifiers [10, 11], to name a few, but I will only discuss the dc-SQUID in detail in this thesis.

The multiplexing readout for TES detectors is a method to distinguish different pixels from the SQUID signal even when the TES pixels are connected in series. This can be done for example by measuring the readout of the SQUID only at pre-determined time intervals. The multiplexing circuits, in order of technical maturity, are the time division- (TDM), the code division- (CDM) and the frequency division multiplexing (FDM). In TDM the signals are separated into different time domains, where a row of TESs is measured by a single SQUID. A signal from one pixel is measured at time t_1 and saved, then the next pixel is measured at time t_2 and so on. Only one pixel is measured at a time. CDM measures all the pixels all the time, but the distinction between rows of pixels are applied by a time- and row dependent polarity function, so called Walsh codes [12]. Lastly in FDM, all the pixels are measured all the time and the separation of signals is done by applying a distinct ac bias for each pixel, thus providing every pixel with a different signal frequency [3].

TES is not the only superconducting detector. Superconducting tunnel junction (STJ) and in recent years microwave kinetic inductance detectors (MKID) have introduced competition to the TES detectors. MKIDs are promising for IR and sub-mm bolometers with similar sensitivities as TESs, but comparable performance has not yet been demonstrated for x-rays, MKID's strong point is that it scales well for large scale systems due to the readout even for thousands of pixels [3]. The readout can be done by using a single high electron mobility transistor (HEMT) [13]. At the time when MKIDs were first introduced, a new readout scheme for TESs has also been proposed by Irwin *et al* [14], using microwave resonator-based multiplexing. The resonant frequency is modulated with an rf-SQUID coupled to the resonators, and the SQUID current dependent inductance determines the resonant frequency. Thus by coupling the TES current inductively to the rf-SQUID, microwave resonances for each pixel are modulated and read simultaneously by one microwave amplifier.

This thesis focused on characterization of two different superconducting device applications. The first task was to characterize the two stage dc-SQUID system, where the input SQUID is coupled to an input coil and the input SQUID is coupled to the SQUID series array by another coil. The array consists of 100 SQUIDs connected in series. The measured characteristics were the mutual inductance of the input and feedback coils of the input SQUID, which are needed to be able to calculate the measurement dependent amplification factor of the SQUID. The noise floor of the SQUID system was also measured. The second application for superconducting devices was a transition-edge sensor. The measured TES characteristics were the transition temperature for multiple pixels, the IV-characteristics and the noise of a single pixel.

2 Basics of superconductivity, SQUIDs and TESs

2.1 Superconductivity

Superconductivity is a phenomenon where a material loses its electrical resistance in a sharp manner at a well defined temperature and the superconductor becomes a perfect conductor without measurable losses at low frequencies, see Figure 1, [15].This behaviour is due to Cooper pairing, which means that electrons, fermions, form a new correlated quantum state, where pairs of electrons form a macroscopic quantum state. This pairing happens when the net interaction between two electrons is attractive, such interaction is possible in solids at low temperatures [16]. Secondly, superconductors also start expelling the magnetic field from inside the material. This is called the Meissner effect, where a type I superconductor becomes a perfect diamagnet expelling all field [15], and type II superconductors also show diamagnetic properties, but depending on the field strength it can also partially penetrate the superconductor leading to other properties such as levitation, see Figures 2 and 3. For type I superconductor there is a thermodynamic critical field H_c that suppresses superconductivity

$$\frac{H_c^2(T)}{8\pi} = f_n(T) - f_s(T), \tag{1}$$

where f_n and f_s are the Helmholtz free energies per unit volume in the respective phases in zero field, for type II superconductors superconductivity survives to a even higher field H_{c2}. The decay of the magnetic field inside of the superconductor takes place within the so called penetration depth λ, having the typical values $\lambda(0) \approx 500$ Å at $T << T_c$ [15]. Empirically the approximate description for the temperature dependent λ is

$$\lambda(T) \approx \lambda(0)\Big[1 - \Big(\frac{T}{T_c}\Big)^4\Big]^{-1/2}, \tag{2}$$

where T_c is the transition temperature of the superconductor [15]. We see that penetration depth diverges at $T \to T_c$ as it should when entering the normal state.

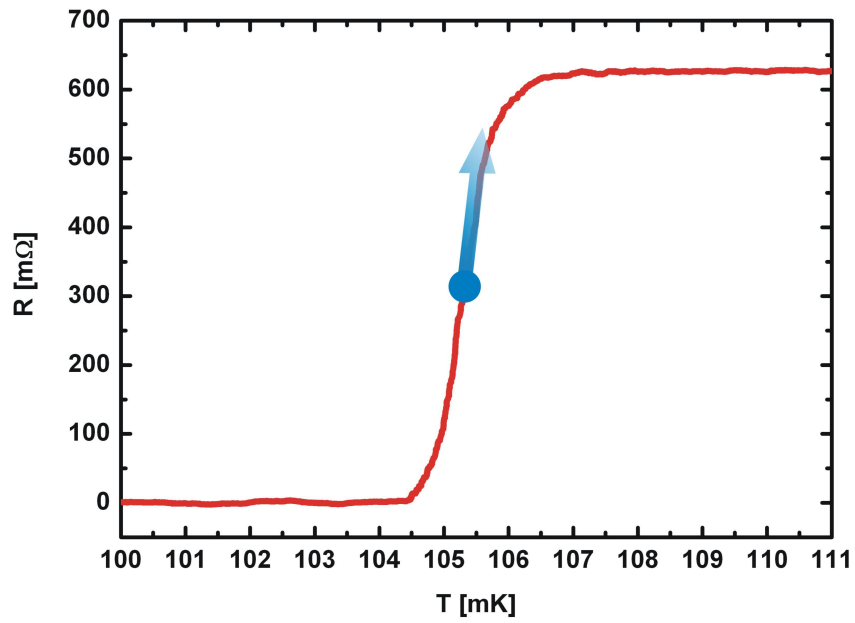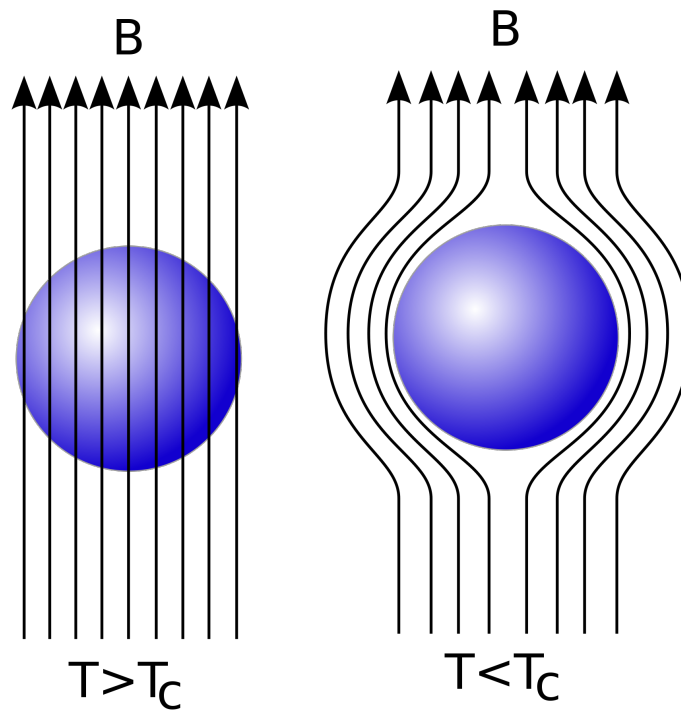**Figure 1.** The superconducting transition, resistance as a function of temperature.

Figure 2. The Meissner effect in a superconductor. The superconductor becomes a perfect diamagnet at temperatures below T_c.

Figure 3. Demonstration of the Meissner effect of type II superconduction. Superconductor is levitating on top of a magnet. Photo by Mike Bell `https://www.flickr.com/photos/mikedbell/4131403101/`

2.2 Josephson Junction

A Josephson junction is formed when two superconductors are connected by a weakly coupling link. Examples of these are superconductor-insulator-superconductor (SIS), superconductor-normal metal-superconductor (SNS) and superconductor-constriction-superconductor (S-c-S) junctions. Josephson showed that tunneling of electron pairs is possible for closely placed superconductors that form a tunnel junction [6]. This pair tunneling depends on the phases of the effective wavefunctions of both super-conductors. Hence a current could flow through the junction and no voltage would develop across it until the critical current is reached. If the distance between the superconductors is small enough so that the wavefunctions penetrate the barrier sufficiently, the superconductors become coupled, which in turn reduces the system energy. If the coupling energy exceeds the thermal fluctuation energy, the phases of the two superconductors become locked, which allows pair tunneling across the junction with no energy loss. The derivation of pair tunneling relations, the Joseph-son relations, can be found in literature [17], so I shall present the relations as is:

$$J = J_c \sin\phi, \tag{3}$$

where J and J_c are the current and critical current densities, respectively, and ϕ is the phase difference across the junction, and

$$\frac{\partial \phi}{\partial t} = \frac{2e}{\hbar}V, \tag{4}$$

where t is the time, e is the elementary charge, $\hbar$ is reduced Planck's constant and V is the voltage across the junction. Let's consider the electrical work done

by a current source. The work done by the source in changing the phase can be integrated with equations (3) and (4) to derive the coupling free energy F stored in the junction, $\int I_s V dt = \int I_s(\hbar/2e)d\phi$,

$$F = \text{const.} - E_J \cos\phi,$$
$$E_J \equiv \frac{\hbar I_c}{2e}, \tag{5}$$

where I_s is the supercurrent, E_J is the Josephson energy, and I_c is the critical current of the junction. Here the current density J in equation (3) has been changed to current I, since for a given Josephson junction, if the dimensions of the junction are known the current can be integrated from the current density. It can be seen that if $\phi = 0$, the coupling free energy has a minimum, which is similar to the case of bulk superconductor in the absence of phase gradients. Another interesting result from equation (4) is the effect of dc voltage across the junction. When dc voltage is applied across the junction, integration of equation (4) shows that

$$\phi = \phi_0 + \frac{2e}{\hbar}Vt, \tag{6}$$

where ϕ_0 is an arbitrary phase and substituting this into equation (3) gives

$$I = I_c \sin(\omega_J t + \phi_0), \tag{7}$$

where

$$f_J = \frac{\omega_J}{2\pi} = \left(\frac{1}{2\pi}\right)\frac{2e}{\hbar}V, \tag{8}$$

is the Josephson frequency. The coefficient in equation (8) is $483.6 \cdot 10^{12}\frac{\text{Hz}}{\text{V}}$. This shows that there is an ac current if a dc voltage is applied. However, as can be seen in Figure 4, it is possible to increase current without developing voltage across the junction. Equation (4) is defined by using a simple coupling constant between the superconductors, which is not specific to the physics of tunneling [17]. As long as the coupling between the superconductors is weak enough, they obey the Josephson relations.

2.2.1 Effects of magnetic field

There are two important properties that need to be considered how magnetic field affects the current across a Josephson junction. Also an assumption is made that for the remainder of the section 2, the junction size is negligible to the size of the coupling coil that is used to create the external flux penetrating the junction.

The gauge invariant phase
Current density is a function of the phase difference across the junction, see equation (3). The phase difference can be defined in such a way, see [17, 18], that the mathematical formulation (gauge), for any magnetic field present, does not affect
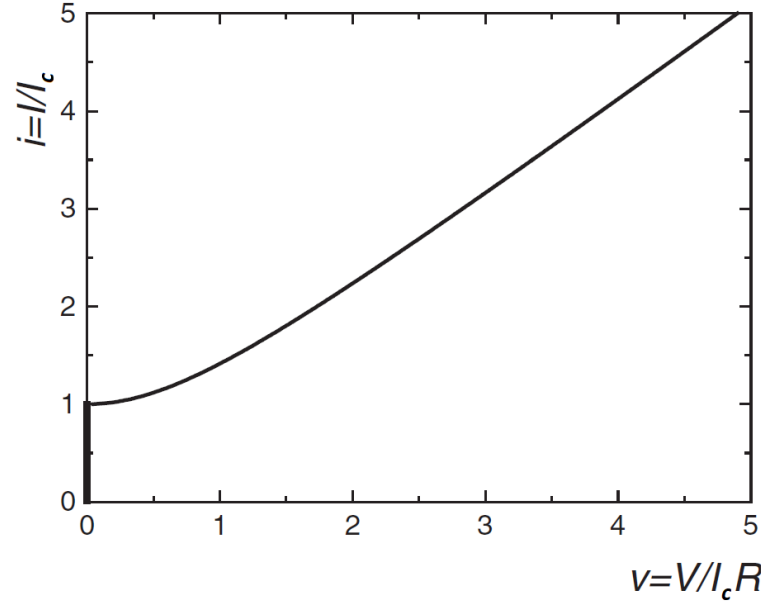
Figure 4. The IV-characteristics of a damped Josephson junction, where it can be seen that there can be current in the zero-voltage region.

the value of the current density. This applies for both tunnel junctions (SIS) as well as conductive barrier junctions (SNS, S-c-S).

In Figure 5, the phase difference between points P1 and P2 can be defined as

$$\phi = \theta_{P2} - \theta_{P1} + \frac{2e}{\hbar} \sum_{P1}^{P2} \vec{A}(x,t) \cdot \vec{dl}, \tag{9}$$

where θ_{P1} and θ_{P2} are the phases of the wavefunction at position P1 and P2, and $\vec{A}$ is the magnetic vector potential. By choosing the London gauge [17], where $\nabla\theta = 0$ inside the superconducting electrodes, we have $\theta_{P1} = \theta_{Q1}$, and the phase difference between the points P and Q gives a result

$$\phi(P) - \phi(Q) = \frac{2e}{\hbar}\Phi_{\perp}, \tag{10}$$

where $\phi(i)$ are the phase differences at different sections of the superconductor and $\Phi_{\perp}$ is the magnetic flux perpendicular to the pair tunneling direction, see Figure 5 and [17]. It can be seen that the phase difference along a junction is proportional to the magnetic flux passing between the chosen points in the superconductors.

Zero-voltage-current dependency
In section 2.2, to get to equation (3) it was assumed that the phase difference across
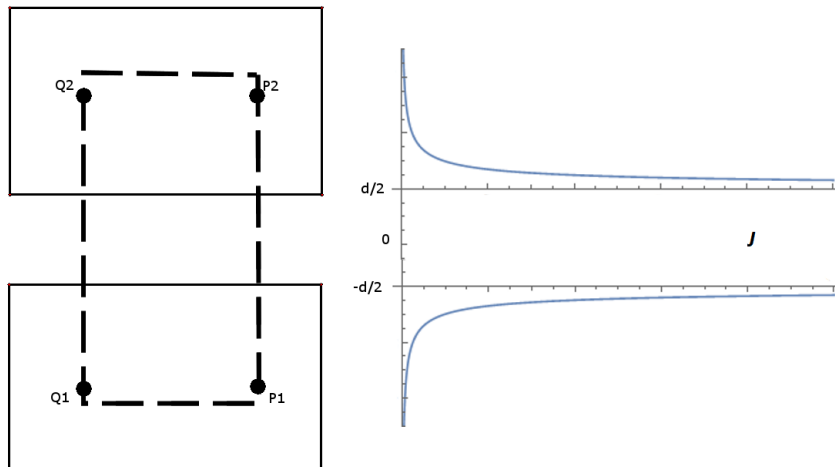
Figure 5. Two superconducting electrodes with a barrier in between. The current density is shown as function of superconductor thickness, d is the barrier thickness. The integration path is shown with the dashed line. Points P and Q represent arbitrary positions in the two superconducting electrodes where the current density is zero.

the junction is the same at all points, however this is not always true. It can vary due to magnetic field passing through the junction as was just demonstrated above. It can be shown, see [17], that the critical current across the junction then behaves as

$$I_c(\Phi) = I_c(0) \left| \frac{\sin(\pi\Phi/\Phi_0)}{\pi\Phi/\Phi_0} \right|, \tag{11}$$

where Φ and Φ_0 are the total magnetic flux through the junction and magnetic flux quantum, respectively. $\Phi_0 = \frac{h}{2e} = 2.068 \cdot 10^{-15}\,\text{Wb}$. Plot of equation (11) is shown in Figure 6. The maximum of the critical current is in multiples of $\Phi_0/2$. This assumes the uniformity of the tunnel barrier and neglects the magnetic field produced by the tunneling current. Lastly the magnetic flux cannot be increased indefinitely due to the suppression of superconductivity.

2.2.2 Circuit modeling of Josephson junctions

A Josephson junction can be modeled with a resistively and capacitively shunted junction (RCSJ)-model [15, 17]. The model is shown as a diagram in Figure 7. The Kirchhoff's laws can be applied to find that

$$C\dot{V} + \frac{V}{R} + I_c\sin\phi = I + I_N(t), \tag{12}$$

where C is the junction capacitance, V is the voltage across the junction, R is the junction resistance, I_c, I, and $I_N(t)$ are the maximum dc supercurrent, the junction
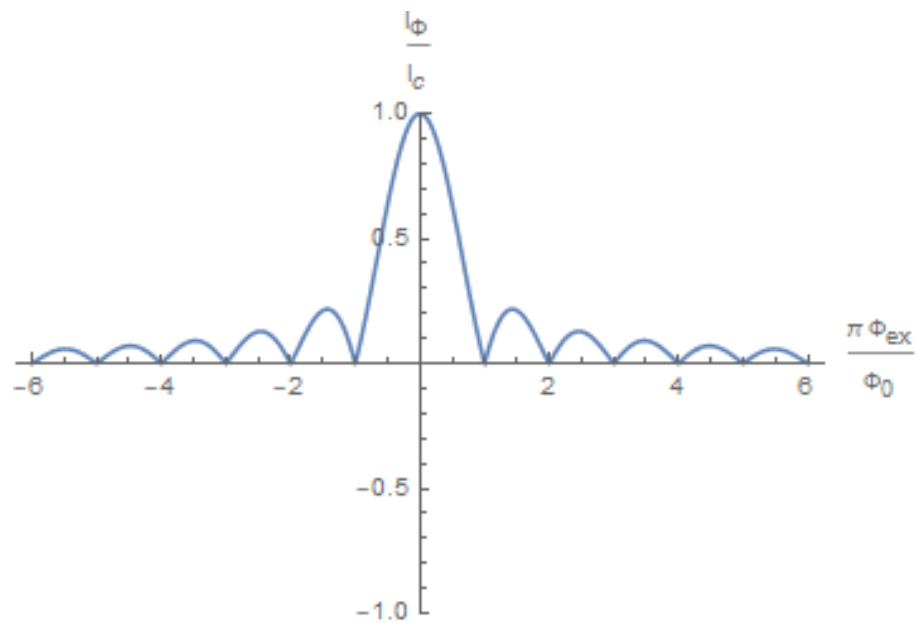
Figure 6. Maximum zero-voltage current behaviour of a Josephson junction, with a uniform barrier, as a function of flux through the barrier.
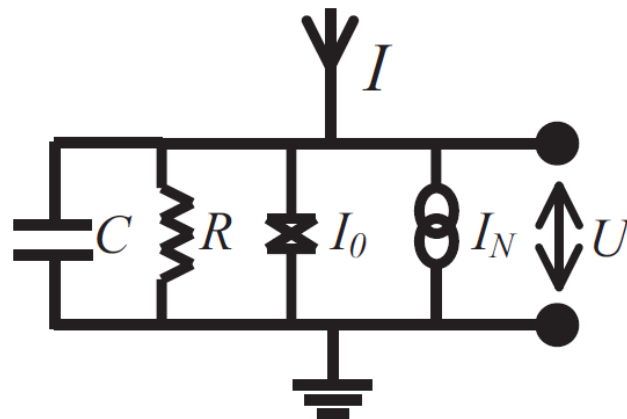

Figure 7. RCSJ-model of a Josephson junction. A driving current is applied through the junction, which is modeled with a capacitance, a resistance, a supercurrent and a noise current source in parallel.
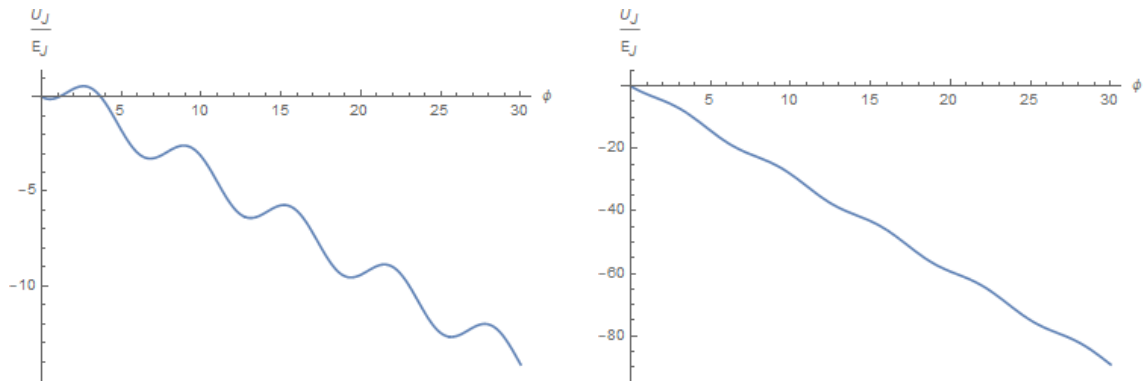
Figure 8. Tilted washboard potential, showing the behaviour of gauge invariant phase as analogue to the particle with mass. On the left, the case where $I < I_c$ and on the right $I > I_c$. When $I < I_c$, the "particle" (=phase) will be trapped inside a potential minimum, but as the current increases the slope becomes steep enough and the "particle" (=phase) can move freely.

current, and the noise current, respectively. Now using the equations (4) and (12) and assuming a dc source and neglecting the noise term we find

$$\frac{\hbar C}{2e}\frac{d^2\phi}{dt^2} + \frac{\hbar}{2eR}\frac{d\phi}{dt} = I - I_c\sin\phi = -\frac{2\pi}{\Phi_0}\frac{\partial U_J}{\partial\phi}, \tag{13}$$

where $U_J \equiv \frac{\Phi_0}{2\pi}[I_c(1-\cos\phi) - I\phi] = E_J(1-\cos\phi - \frac{I}{I_c}\phi)$ is a tilted washboard potential, see Figure 8. It is a useful tool to create a mechanical analogue for the gauge invariant phase difference equation for the RCSJ-model, where equation (13) can be explained in terms of the equation of motion of a particle with mass in a tilted washboard potential, see Figure 8, with equation of motion

$$m\ddot{x} + \xi\dot{x} = -\frac{\partial w(x)}{\partial x} + F_d, \tag{14}$$

where m is the mass of the particle, ξ is the friction coefficient, and $w(x)$ is the potential which is titled by force F_d. Starting from equation (14), the Josephson junction can be described by the following analogues: the coordinate x is replaced by ϕ, and the velocity $\dot{x}$ by $\dot{\phi} \sim V$. Mass and friction coefficient of the particle correspond to the capacitance C and conductance $\frac{1}{R}$, respectively. However, this analogue is feasible only in the small-area junctions where the internal inductances are negligible, i.e. where the junction can be modeled by the circuit in Figure 7.

2.2.3   Hysteresis in a Josephson junction

To study the hysteretic behaviour of the Josephson junctions, a new variable will be defined, the so called Stewart-McCumber parameter β_c. Now continuing from equation (13) and defining a new variable

$$\omega_c = \frac{2e}{\hbar} I_c R = \frac{2\pi I_c R}{\Phi_0},$$
(15)

which is the characteristic frequency, the Josephson frequency at a characteristic voltage $V_c \equiv I_c R$. Hence equation (13) becomes

$$\frac{I}{I_c} = \beta_c \frac{d^2\phi}{dt^2} + \frac{d\phi}{dt} + \sin\phi,$$
(16)

where $\beta_c = \omega_c C R = \frac{2e}{\hbar} I_c R^2 C$. The parameter β_c can be used to define two limits, $\beta_c << 1$, the strongly overdamped limit and $\beta_c >> 1$, the strongly underdamped limit. In the strongly overdamped limit the inertial term in equation (16) becomes negligible and the IV-characteristics becomes non-hysteretic, see Figure 4. In the strongly underdamped limit the dynamics of the junction are solely determined by the RC-circuit, which leads to a simple ohmic response. This means that when a larger current than I_c is applied and then lowered the dc voltage stays finite until the current is reduced to zero, but starting from zero voltage, the current can be increased without increasing the voltage until I_c is reached. This leads to noticeable hysteresis in the junction, which can be seen in Figure 9.

In practical low-T_c tunnel junctions a shunt resistor is typically used to reduce β_c to less than unity and to obtain non-hysteretic I-V-characteristics. In order for the parameter $\beta_c \leq 1$, we must have $\frac{\hbar}{2e} \geq I_c R^2 C$. Thus, there is a limit how large the capacitance across the junction can be, as the critical current is material and dimension related quantity, which is not so easy to change drastically in applications. But considering that resistance changes as R^2 in the function, adding a small shunt resistor can lower the β_c value below unity easily.

2.3   The dc-SQUID theory

As stated in the Introduction, the dc-SQUID measures the magnetic flux through the SQUID loop. Now let's start by calculating what the relation is between the gauge invariant phases of the two connected Josephson junctions, see Figure 10, and the total current through the parallel combination of junctions. Assuming the path of integration is deep enough in the superconductor to let the supercurrent density J_c to be zero, integrating clockwise following the arrowed path in Figure 10 results in

$$\int_A^B \nabla\theta \cdot \vec{dl} + \int_C^D \nabla\theta \cdot \vec{dl} = -\frac{2e}{\hbar} \int_A^B \vec{A} \cdot \vec{dl} - \frac{2e}{\hbar} \int_C^D \vec{A} \cdot \vec{dl},$$
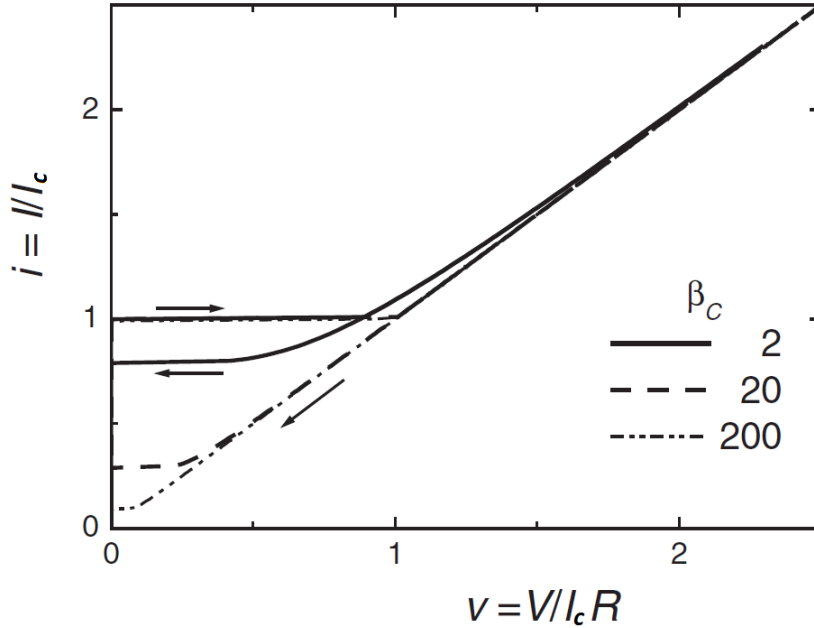(17)

Figure 9. Strongly underamped case of IV-characteristics of a Josephson junction with three different β_c values, 2, 20, and 200. Hysteretic behaviour becomes more obvious the higher the parameter β_c value is.

where junction gaps were excluded. Here $\vec{A}$ is the magnetic vector potential and θ is the phase of the pair wavefunction. Equation (17) can also be written as

$$\oint \nabla\theta \cdot \vec{dl} - (\theta_A - \theta_D) - (\theta_C - \theta_B) = -\frac{2e}{\hbar} \oint \vec{A} \cdot \vec{dl} + \frac{2e}{\hbar} \int_D^A \vec{A} \cdot \vec{dl} + \frac{2e}{\hbar} \int_B^C \vec{A} \cdot \vec{dl}. \quad (18)$$

The first closed loop integral gives $\oint \nabla\theta \cdot \vec{dl} = -2n\pi$, where the negative sign is taken for convenience. Using Stoke's theorem, the second closed loop integral gives $\oint \vec{A} \cdot \vec{dl} = \Phi$ the magnetic flux in the loop directed into the page. Now applying the definition of gauge invariant phase difference from section 2.2.1

$$\phi = \theta_B - \theta_A + \frac{2e}{\hbar} \int_A^B \vec{A} \cdot \vec{dl}, \quad (19)$$

equation (18) can be written in the form

$$\phi_2 = \phi_1 + 2n\pi - 2\pi \frac{\Phi}{\Phi_0}, \quad (20)$$

where the flux Φ would get values from $-\frac{\Phi_0}{2}$ to $\frac{\Phi_0}{2}$. Including the $2n\pi$ term into the total flux lets the flux Φ have any value resulting in

$$\phi_2 = \phi_1 - 2\pi \frac{\Phi}{\Phi_0}. \quad (21)$$
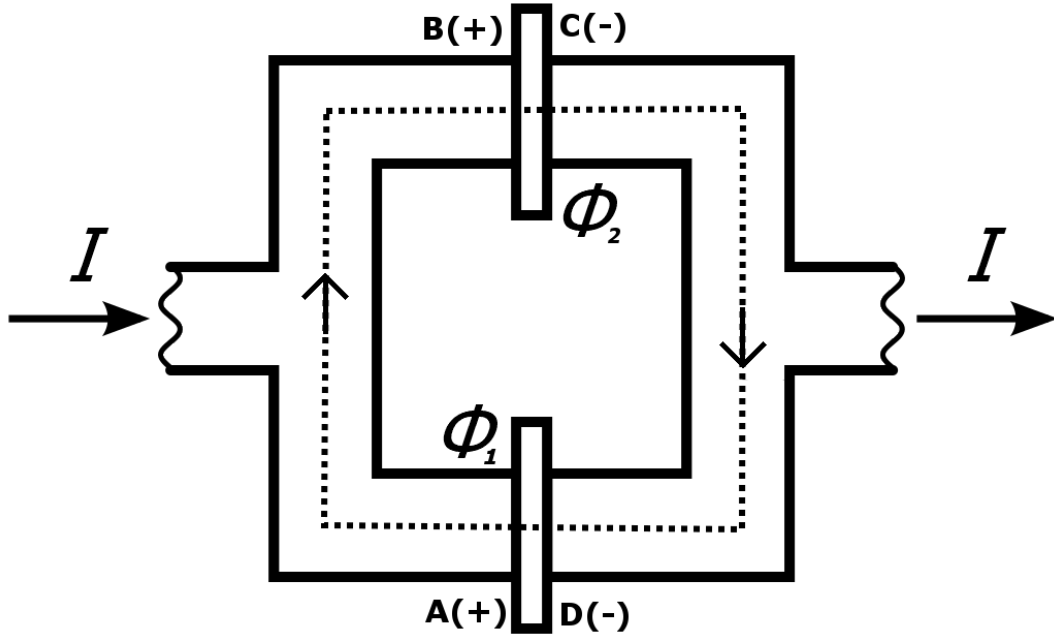
Figure 10. The schematic of a dc-SQUID. Two superconductors are connected by two tunnel junctions to form a loop. The integration path is shown by the dashed dots and direction is clockwise shown by the arrows.

The total current through the SQUID is then

$$I_{SQ} = I_1 + I_2 = I_{c1}\sin\phi_1 + I_{c2}\sin\phi_2 = I_{c1}\sin\phi_1 + I_{c2}\sin\left(\phi_1 - \frac{2\pi\Phi}{\Phi_0}\right), \qquad (22)$$

where I_{c1}, ϕ_1 and I_{c2}, ϕ_2 are the critical current and the gauge invariant phase difference of the two junctions.

2.3.1 Effects of self-induced flux and asymmetries

Self-induced flux Φ_{self} is the flux produced by the circulating current I_{circ} flowing around the physical SQUID loop with inductance L. It can be defined as

$$\Phi_{self} = LI_{circ}. \qquad (23)$$

Let's now consider equation (22) in terms of the total flux Φ with and without self-induced flux. Generally, the critical currents I_{c1} and I_{c2} are unequal. Assuming the self-induced flux is negligible and maximizing equation (22) with respect to ϕ_1 gives

$$I_{SQ}(\Phi_{ex}) = \left[(I_{c1} - I_{c2})^2 + 4I_{c1}I_{c2}\cos^2\left(\frac{\pi\Phi_{ex}}{\Phi_0}\right)\right]^{1/2}, \qquad (24)$$
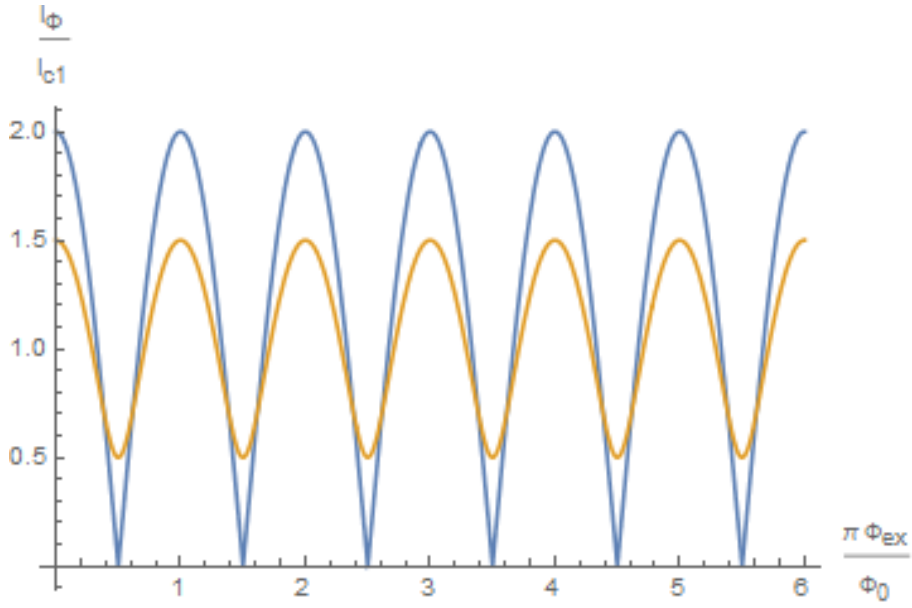
Figure 11. The dc-SQUID total critical current modulation with equal critical currents (blue line) and with $I_{c1} = 2I_{c2}$ (orange line).

where Φ_{ex} is the external flux through the SQUID and relates to the total flux as $\Phi = \Phi_{ex} + \Phi_{circ}$. In the case where $I_{c1} = I_{c2}$, equation (24) becomes

$$I_{SQ}(\Phi_{ex}) = 2I_{c1}\left|\cos\frac{\pi\Phi_{ex}}{\Phi_0}\right|. \tag{25}$$

Both equations (24) and (25) are plotted in Figure 11 to see the critical current dependence on the external flux.

Now let's add the self-induced flux in the following way, assuming identical junctions ($I_{c1} = I_{c2}$):

$$\Phi_{self} = \frac{1}{2}L(I_2 - I_1) = \frac{1}{2}LI_{c1}(\sin\phi_2 - \sin\phi_1). \tag{26}$$

Substituting $\Phi = \Phi_{ex} + \Phi_{self}$ into equation (21) gives the relation between ϕ_2 and ϕ_1

$$\phi_2 = \phi_1 - \frac{2\pi}{\Phi_0}[\Phi_{ex} + \frac{1}{2}LI_{c1}(\sin\phi_2 - \sin\phi_1)]. \tag{27}$$

If two junctions are symmetrically placed and $I_{c1} = I_{c2}$, I_{SQ} divides equally to both junctions and the net self-flux through the loop is zero. When an external flux is applied, the currents I_1 and I_2 are not equal anymore, and the circulating current is finite, given by

$$I_{circ} = \frac{1}{2}(I_2 - I_1). \tag{28}$$

Adding the circulating current I_{circ} to the balanced case where $I_1 = I_2 = \frac{I_{SQ}}{2}$ gives currents in the junctions

$$I_1 = \frac{I_{SQ}}{2} - I_{circ} \tag{29}$$

$$I_2 = \frac{I_{SQ}}{2} + I_{circ}. \tag{30}$$

The effects of asymmetry, for example a displacement of the loop from the center, causing different flux linking in the loop, or unequal critical currents in the junctions, can be reduced by careful fabrication designs. The effect of asymmetrical flux linking tilts the critical current modulation so that the modulation is not symmetric [17]. Also the finite size of the junctions affects the current passing through the junction. These effects are further discussed in literature [17, 18].

2.3.2 The dc-SQUID as a flux detector

The dc-SQUID is very sensitive at detecting changes in magnetic flux. It can be used as a magnetometer [7], where external magnetic field is measured by a coil system and coupled to the SQUID by a coil inside a magnetically shielded environment. It can be also used as a gradiometer [17]. In this work, a dc-SQUID is used as an ammeter, where an external current is coupled to a input coil, which produces the external flux sensed by the SQUID.

From the results calculated in sections 2.2 and 2.3 the modulation behaviour of the IV-curves of the dc-SQUID can be plotted, see Figure 12. In Figure 12 it can be seen that if the SQUID is biased properly, above the lower critical current, its voltage is a function of flux, see right top panel. The output of the SQUID is linear in the range $\Phi/n\Phi_0 = [1.0, 1.25]$, where the change in voltage behaves $\Delta V \approx R_d \Delta I_{SQ}$, where $R_d = \frac{dV}{dI}$ is the dynamic resistance of the SQUID at a bias point V_b.

2.3.3 Noise in dc-SQUID

The noise for linear systems that fluctuate at equilibrium can be described by the fluctuation-dissipation theorem [19, 20]. From this a current fluctuation for a circuit with admittance $Y(\omega)$ can be derived [21]

$$S_I(\omega) = 2\hbar\omega \mathrm{Re}[Y(\omega)]\left[\coth\left(\frac{\hbar\omega}{2k_BT}\right) + 1\right],$$

and writing this as a function of directly measurable frequency f gives

$$S_I(f) = 2hf\mathrm{Re}[Y(f)]\left[\coth\left(\frac{hf}{2k_BT}\right) + 1\right]. \tag{31}$$

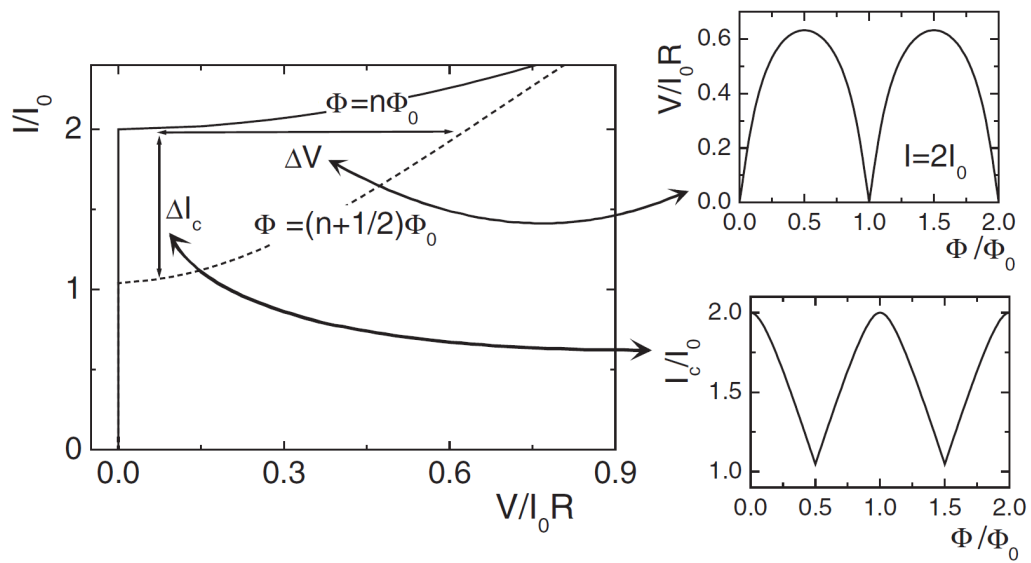**Figure 12.** Left: Part of the IV-curve of a dc-SQUID with $\Phi = n\Phi_0$ (line) and $\Phi = (n+1/2)\Phi_0$ (dashed line). The maximum of critical current modulation is the difference between these two lines, at $V = 0$ the behaviour is shown on the bottom right. $I_0 = (I_{c1} + I_{c2})/2$ represents the average of the two critical currents of the two junctions. On the top right the modulation of voltage is shown at $I = 2I_0$.

The SQUID is usually operated in a linear region. In the RCSJ-model, the dc-SQUID is comprised of two parallel sets of a parallel resistor and a capacitor. The noise producing element in this case is the resistor. Let's first consider only the low frequencies $hf << k_BT$. This results to a current noise when using the lowest order Taylor expansion of the coth function [22]

$$\coth = 1/x + \frac{1}{3}x - \frac{1}{45}x^3 + \frac{2}{945}x^5 - \frac{1}{4725}x^7 + ..., \tag{32}$$

$$S_I(f) = 4\text{Re}[Y(f)]k_BT = \frac{8k_BT}{R}, \tag{33}$$

where the total resistance of the circuit is

$$R_{tot} = \left(\frac{1}{R} + \frac{1}{R}\right)^{-1} = \frac{R}{2}. \tag{34}$$

At high frequencies $hf >> k_BT$, equation (31) becomes

$$S_I(f) = 4\text{Re}[Y(f)]hf = \frac{8hf}{R}. \tag{35}$$

For a practical measurement setup, the operating temperature is below $100\,\text{mK}$, and the condition $hf << k_BT$ results in a frequency limit $f << 2.1\,\text{GHz}$, at $100\,\text{mK}$. Equation (33) is the so called Johnson noise of a resistor, in this case two resistors connected parallel, and it is a white noise source. White noise means that it is frequency independent.

The dc-SQUIDs typically have so called $1/f$-noise or flicker noise [18], which becomes important in the low frequency range. There are two major sources of this noise whose power spectral density scales as $1/f$. First is due to the flux lines trapped in the body of the SQUID, which aren't stagnant and jump around. The motion of these thermally activated vortices induce a change in the flux Φ_a which is coupled to the SQUID. The second is due to fluctuations in the Josephson junctions barrier properties, leading to fluctuations in the critical current [23]. For a more details on vortices see [18] and on critical current fluctuations see [23].

2.4 Elements of transition-edge sensor theory

An x-ray transition-edge sensor can be modeled by calorimeter theory [2, 24, 25, 26]. The simplest model is shown in Figure 13. The transition-edge sensor with a heat capacity C is connected to a heat bath at temperature T_S through a weak thermal link with thermal conductance G. Bias current keeps the TES at an elevated temperature, at the superconducting transition, with Joule heating power P_J. This is a steady state temperature T_0, because the Joule heating and the cooling power from the bath stabilize to dynamic equilibrium. The steady state is broken when a photon with energy E_γ is absorbed, and the temperature of the TES rises by E_γ/C

and relaxes back to the steady state temperature T_0 with a time constant $\tau = C/G$.

The response of the TES can be described by differential equations for the thermal and the electrical circuits. The thermal equation, for the simplest model shown in Fig. 13, without noise terms is [2]

$$C\frac{\mathrm{d}T}{\mathrm{d}t} = -P_{out} + P_J + P_{in},\tag{36}$$

where P_{out} is the power extracted to the bath by the thermal link and P_{in} is the signal power from the incoming photon. The Joule power is heating the system due to a current driven through the TES, $P_J(I,T) = I^2R(I,T)$. The power introduced by the incoming photon can be approximated as na instantaneous power spike with the relation $P_{in}(t) = E_\gamma\delta(t - t')$, where $\delta(t - t')$ is the Dirac delta function. This approximation is valid when the relaxation time due to the thermal link between the TES and the temperature bath is much slower than the time it takes for the TES temperature to equilibriate [25]. The power law dependence of the power P_{out} extracted by the temperature bath can be written as

$$P_{out} = K(T^n - T_S^n),\tag{37}$$

from which the differential thermal conductance between the bath and the TES can be defined as

$$G \equiv \frac{\mathrm{d}P_{out}}{\mathrm{d}T} = nKT^{n-1}.\tag{38}$$

Figure 14 shows the voltage bias circuit as well as the Thevenin-equivalent representation. The electrical differential equation without noise terms is

$$L\frac{\mathrm{d}I}{\mathrm{d}t} = V_{th} - I_{TES}R_L - I_{TES}R(T,I),\tag{39}$$

where L is the inductance of the SQUID input coil, $V_{th} = V_b\frac{R_S}{R_b}$ is the Thevenin-equivalent voltage source and $R_L = R_S + R_p$ is the load resistance. The resistance of the TES is a function of both temperature and current $R(T,I)$. Let's describe the steepness of the superconducting transition by two dimensionless parameters defined as: temperature sensitivity

$$\alpha \equiv \left.\frac{\partial\log R}{\partial\log T}\right|_{I_0} = \left.\frac{T_0}{R_0}\frac{\partial R}{\partial T}\right|_{I_0}\tag{40}$$

and current sensitivity

$$\beta \equiv \left.\frac{\partial\log R}{\partial\log I}\right|_{T_0} = \left.\frac{I_0}{R_0}\frac{\partial R}{\partial I}\right|_{T_0},\tag{41}$$

where I_0, R_0, and T_0 are the steady state values of current, resistance, and temperature of the TES, respectively. Increasing α decreases the effective time constant of the system, $\tau_{eff} \propto \alpha^{-1}$, and β increases the constant-temperature dynamic resistance of the TES

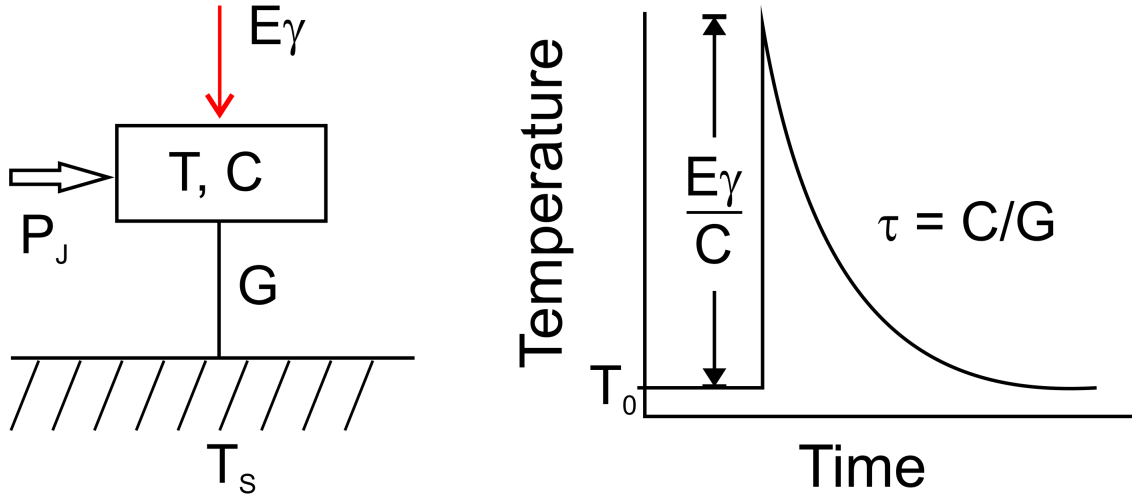$$R_{dyn} \equiv \left.\frac{\partial V}{\partial I}\right|_{T_0} = R_0(1 + \beta).$$

Figure 13. On the left, a simple one block thermal model of the TES, with heat capacity C, connected to a heat bath at temperature T_s through a thermal link G. On the right, a photon with energy E_γ is absorbed to the TES and the system reverts back to steady state within a time constant τ.

However, neither of these are directly obtained from the measured IV-curve of the TES, but the parameter from the measurement includes effects from both α and β,

$$\alpha_{tot} = \frac{T_0}{R_0}\frac{\mathrm{d}R}{\mathrm{d}T} = \frac{2\alpha + \frac{n}{\phi}\beta}{2 + \beta}, \tag{42}$$

where $\phi = 1 - \left(\frac{T_s}{T_0}\right)^n$ and the steps to derive the α_{tot} are taken in appendix A, which follows references [27, 28].

2.4.1 Negative electro-thermal feedback and pulse decay time

It is advantageous to use a TES detector in a negative electro-thermal feedback (ETF) setting, since it makes the detector bias point more stable as well as decreases recovery time from pulses. This ETF means that a voltage biased TES in its transition stabilizes itself back towards the steady state after a pulse with energy E has been absorbed. Negative ETF can be understood the following way: when the temperature of the TES increases due to absorbed energy, the resistance of the TES increases and this increased resistance decreases the Joule heating power heating the system thus lowering the temperature. The effective time constant (the pulse decay time) due to ETF is given [29] by equation

$$\tau_{eff} = \frac{\tau}{1 + \alpha\phi n}, \tag{43}$$

where $\tau = G/C$. If α is increased the time constant decreases, which in turn speeds the pulse decay, which is highly desired as applications can be limited by detector speed.
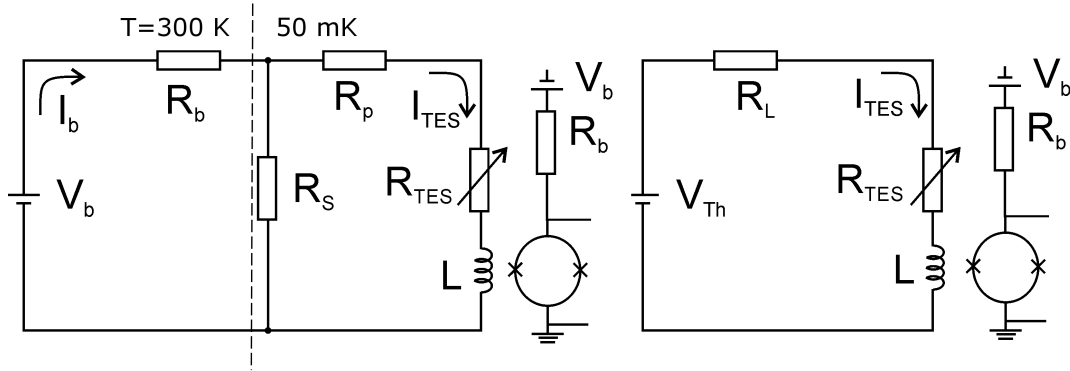
Figure 14. On the left, the TES electrical circuit as it is configured in the experiment. The bias side of the circuit is at room temperature. At the sample stage, shunt resistor $R << R_s$ produces the voltage bias, and a parasitic resistance R_p is added for modeling accuracy. A SQUID with input inductance L reads the current. On the right, the Thevenin equivalent of the circuit.

2.4.2 TES noise

Transition-edge sensor noise sources are mainly the following four: amplifier (SQUID) noise, discussed already in section 2.3.3, thermal fluctuation noise between the TES and the heat bath, Johnson noise of the TES, and Johnson noise of the load resistors. The noise not falling under these categories are labeled under excess noise. Johnson noise current of the TES gives a power spectral density of [2]

$$S_{I_{TES}} = 4k_B T_0 I_0^2 R_0 \xi(I)(1 + \omega^2 \tau^2)|s_I(\omega)|^2 / \mathcal{L}_I^2, \tag{44}$$

where $\xi(I) = 1$ for normal resistors, and for nonlinear resistors such as TESs, quadratic expansion gives $\xi = 1 + 2\beta$ [2]. Here $s_I(\omega) = dI/dP_{in}$ is the power to current responsivity, which is used to describe theoretical spectral response of the detector, and P_{in} is the input power to the TES. $\mathcal{L}_I$ is the low-frequency constant current loop gain, which is defined as

$$\mathcal{L}_I \equiv \frac{P_J \alpha}{G T_0}.$$

The power spectral density for thermal fluctuation current noise is

$$S_{I_{TFN}} = 4k_B T_0^2 G \times F(T_0, T_{bath})|s_I(\omega)|^2, \tag{45}$$

where $F(T_0, T_{bath})$ describes the nature of the thermal conductance of in the link, and is typically between 0.5 and 1. New thermal fluctuation sources might be introduced for example if the TES has an absorber on top of it. An absorber is an extra layer of material added on top of the TES. The absorber is used to transform incoming radiation into heat and couple it to the TES. This extra heat capacity will increase the amount of fluctuations due to the energy exchange between the two

heat capacity blocks. Different theories for the excess noise of the TES have been proposed in [30, 31, 32, 33]. It is possible that different designs have different excess noise sources, which means that an universal explanation or consensus on the theory cannot be found. However in Jyväskylä for Corbino TES devices it was shown [34] that all noise could be explained by the complex, multi-block thermal model. More in depth discussion of the excess noise for non-Corbino geometry TESs is found in [2]. Perhaps the most important parameter of interest for calorimeters which can be calculated from the noise is the energy resolution. If Gaussian noise sources are assumed [2], the full width half maximum energy resolution is then

$$\Delta E_{FWHM} = 2\sqrt{2\ln 2}\Big(\int_0^\infty \frac{4\mathrm{d}f}{S_{P_{tot}}(f)} \Big)^{-1/2}, \tag{46}$$

where $S_{P_{tot}}(f) = S_{I_{tot}}(\omega)/|s_I(\omega)|^2$ is the total power noise that includes all noise sources and $S_{I_{tot}}(\omega)$ is the total current noise. Theoretically this could reach values below $1\,\mathrm{eV}$ at $6\,\mathrm{keV}$, but current experimental world record is $1.8\,\mathrm{eV}$ at $6\,\mathrm{keV}$ [35].

2.4.3   Impedance of the TES circuit

Another very useful concept used to describe transition-edge sensors is the complex impedance Z_{TES}, because it depends on the thermal circuit and parameters α, β, and it can be measured separately. The complex impedance for the input circuit in Figure 14 is

$$Z_{circuit}(\omega) = Z_{TES}(\omega) + R_L + i\omega L, \tag{47}$$

where for the simple thermal model, shown in Figure 13, the complex impedance is [2]

$$Z_{TES}(\omega) = R_0(1 + \beta) + \frac{R_0\,\mathcal{L}_I}{1 - \mathcal{L}_I}\frac{2 + \beta}{1 + i\omega\tau_I}, \tag{48}$$

where $\tau_I = \tau/(1 - \mathcal{L}_I)$. Figure 15 shows the behaviour for both the simple model and a measurement from [27], where it can be seen that the simple model is not enough to describe the data in question. This leads to additional features in the impedance, which otherwise would have a semicircle in the complex plane. Equations for Z_{TES} for more complex models can be found in [26].
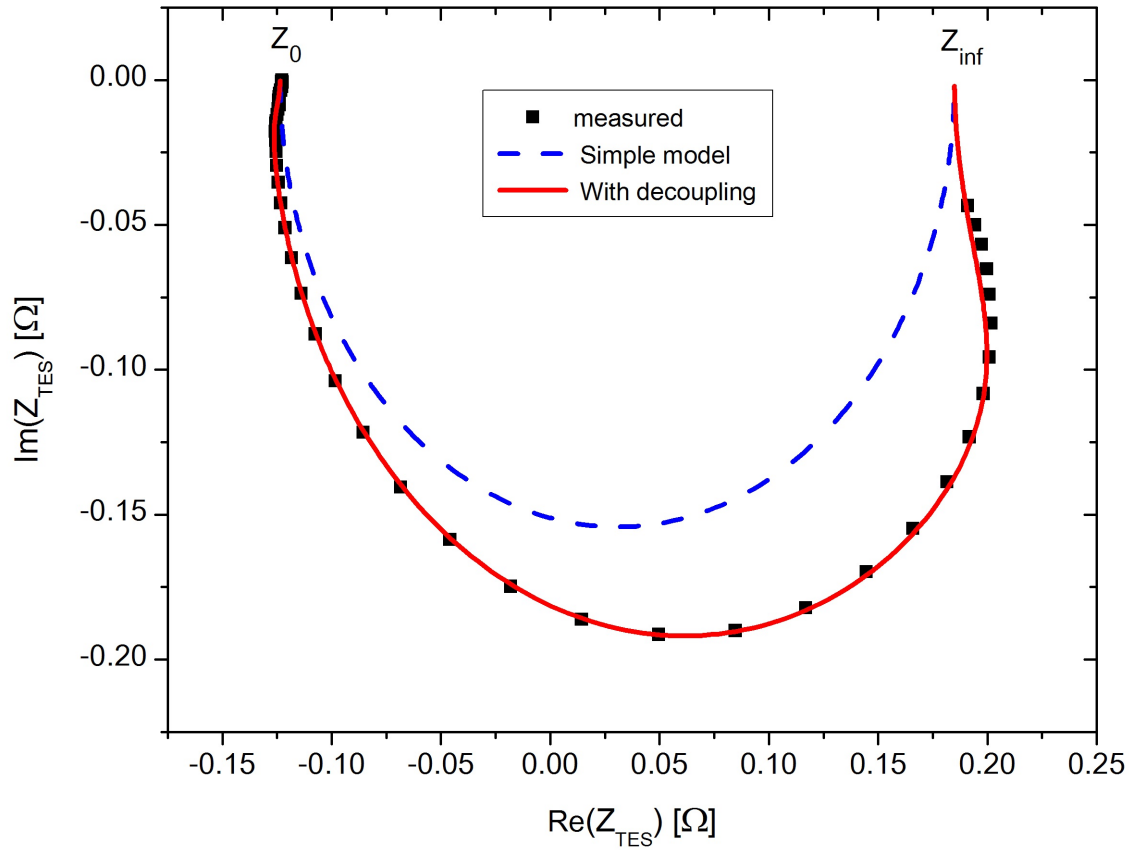
Figure 15. Theoretical complex impedance fits, with the simple one-block thermal model, blue dashed line, and with a more complex model, red line. The complex model with decoupling fits well to the experimental data. Data from [27].

3 Measurement system

3.1 Plastic dilution refrigerator

In order to measure the phenomena and characteristics of superconductors, extreme physical conditions are needed. Very low temperatures are required when measuring Molybdenum-Titanium-Tungsten-alloy-Copper (Mo/TiW/Cu)-trilayer TESs studied here. All the pixels measured had transition temperatures in the range of 120-170 mK. In addition the superconducting wiring inside the cryostat is made of NbTi-wires, the SQUIDs are made of Niobium and the bonding wires across the system are aluminium, with transition temperatures of approximately 10 K, 9 K and 1.5 K, respectively. All of these temperatures are reachable with a ^{3}He-^{4}He-dilution refrigerator. A plastic dilution refrigerator (PDR) that was used is operated inside a liquid helium bath to create a low ambient temperature. The sample stage itself is inside a vacuum jacket so the only direct heat load from the 4.2 K bath is through radiation. A temperature of 1.5 K easily reached by having a chamber that is being pumped constantly and refilled from the liquid helium bath. The heat of evaporation from a small chamber, called the 1 K pot, is enough to counteract the heat load from the ambient bath as well as the heat load from upper cryostat parts and wiring. To reach the base temperatures of the dilution refrigerator, the coldest place in the refrigerator is where the two isotopes of helium mix, see Figure 16. This mixing can produce cooling because the isotopes phase separate at low temperatures, and by pumping ^{3}He atoms across the liquid phase boundary from ^{3}He rich to ^{3}He poor phase, the larger enthalpy in the ^{3}He poor phase leads to cooling. The cooling power at temperatures lower than 100 mK stops being proportional to the concentration since the concentration of ^{3}He in ^{4}He stabilizes at 6.6%, in other words ^{3}He has finite solubility even at absolute zero. This mixing is made continuous by circulating ^{3}He by pumping the ^{3}He at $T \approx 0.7$ K (still) where only ^{3}He will evaporate. The evaporated is returned through a condensing line where it is reliquefied [36]. The schematics of the cold stages of the PDR are shown in Figure 17 and the ^{3}He-^{4}He phase diagram is shown in Figure 16.
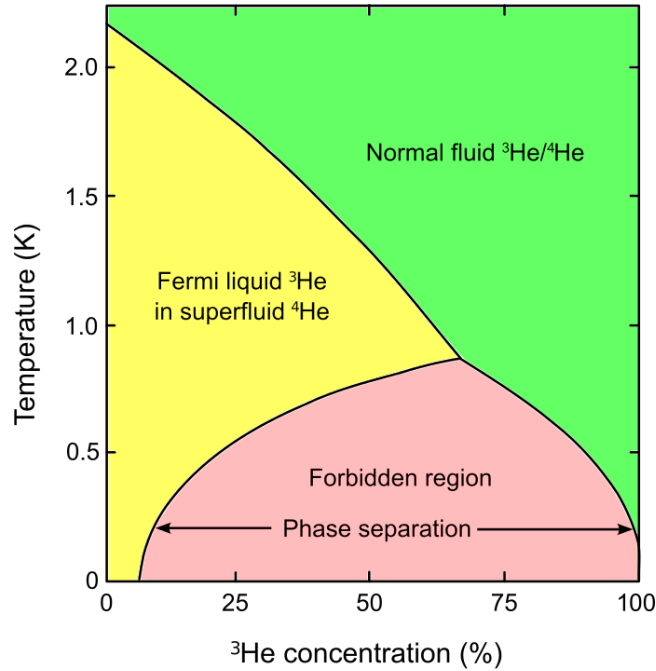
Figure 16. ^{3}He-^{4}He phase diagram, plotted as ^{3}He concentration and temperature in saturated vapour pressure. Inside the green region, both isotopes are normal fluids. In the yellow region it is more favourable for the ^{3}He to dilute into the superfluid ^{4}He than it is to stay in separate phases. Below 0.867 K, the point where all regions meet a phase separation in the system takes place so that points in the forbidden zone are not allowed, but the concentrations of the two phases are given by the forbidden boundary. If low energy ^{3}He molecules are added and high energy ones are extracted, this phase separation can be used as a cooling method.

3.2 Shielding against excess noise

The measurement room used is located on the bottom floor of Nanoscience Center. The room is a large Faraday cage in order to attenuate most of the electromagnetic radiation. The room is also grounded, and there is a possibility of using many of the electronics from outside the room by feeding the signal through filtered inputs. The dewar where the cryostat is submerged provides more attenuation against the EM-radiation from the electronics inside the shielding room, although some noise due to vibrations from the evaporating cryogen might occur. The dewar and the cryostat are also detached from any additional ground connections in order to prevent ground loops, only one ground is provided, connected from the shielded room wall to the refrigerator body. For outgoing lines, coaxial cables are used, and where possible, pairs of coaxial cables have been home made as a twisted pair. DC batteries with regulators are used as stable voltage sources, and a radiofrequency voltage box is
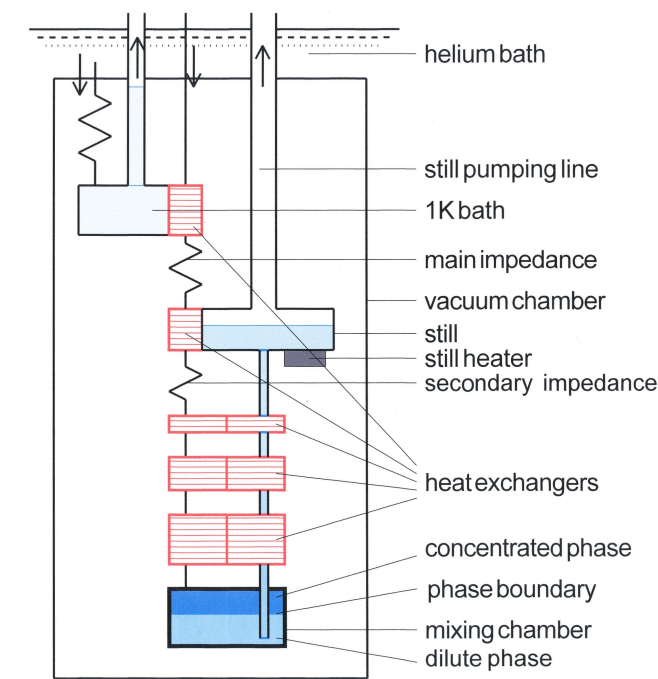
Figure 17. The schematic of the dilution refrigerator. The vacuum jacket is submerged in a liquid helium bath. From outside the vacuum jacket, a so called pot line refills the 1 K bath through an impedance. The 1 K (1.5 K due to heat load) temperature of this bath is reached by evaporative cooling, by pumping to low pressure. The heat which is extracted in the process is used to cool down the incoming ^{3}He gas. The warm gas is liquefied at the first heat exchanger and impedance, and after this it is cooled down by outgoing ^{3}He in the heat exchangers at the plastic part. Once the liquid ^{3}He reaches the mixing chamber, the two helium isotopes phase separate, and by forcing mixing (circulation) this process extracts heat from the liquid and the surroundings. The ^{3}He dilute mixture moves up a small capillary into the still through heat exchangers and warms up. At the still the mixture is heated to $T \approx 0.7$ K, therefore mostly ^{3}He is evaporated and circulated back to the incoming gas line.

used to create a sweep of voltages with known and constant step size.

In order to shield the very sensitive SQUIDs from changes in the ambient magnetic field, two stage shielding is in place. For the series array at 1.5 K pot stage, a superconducting lead shield is placed inside a μ-metal, Cryoperm, shield[1]. For the input SQUID at the sample stage at temperatures well below the T_c of the aluminium, a superconducting aluminium shield is placed inside Cryoperm shielding [37]. The μ-metal shield provides most of the attenuation of sudden changes in magnetic fields, but the superconducting shielding, both of which are type I superconductors, are

---

[1]http://www.vacuumschmelze.com/en/products/materials-parts/soft-magnetic/nickel-iron/cryoperm/cryoperm-physical-properties.html, 23.5.2017

used to further attenuate as well as counteract any sudden changes due to the nature of the Meissner effect. This combination and order of the shields is used to prevent the superconducting shields from trapping flux inside them during cooldown. The most sensitive lines inside the cryostat have been hidden inside a stainless steel mesh shield and teflon tubing in order to protect the lines and attenuate the pick up of radio frequencies inside the mesh.

3.3   SQUID chain

The schematic of the SQUID amplifier chain, which was provided by NIST [38], can be seen in Figure 18. A TES pixel is coupled to the input SQUID through a superconducting input coil on the input SQUID chip, Figure 19. The biased input SQUID reacts to the changes in flux through the SQUID loop, which originate from the input coil. The change in flux generates a change in the current through the series resistance and input SQUID and series array coupling coil. The series array, Figure 20, is used to amplify the small change picked up by the input SQUID, and the amplified signal is amplified again at room temperature with a room temperature preamplifier. The signal is then read by the Flux-Locked Loop (FLL) control electronics. The FLL signal is sent both to the feedback coil to null the flux through the SQUID, and to the room temperature remote controller, see Figure 21. The feedback output signal from FLL electronics to the remote controller can be read by either an oscilloscope or a Digital to Analog Converter (DAC)-card which is optically connected to the PC, to reduce noise sources from outside the EMR-shielded room. Both the input SQUID as well as the series array must be biased for every measurement, and due to subtle changes in the local magnetic field during the cooldown and changes throughout the cooldown, the bias voltage needed for the optimal modulation depth can slightly change.

The preamplifier, provided by SRON[39], works in three different modes. Direct (DIR-), Current-Voltage (IV-), and Full-Amp (FA)-mode. DIR- and IV-modes are dc-coupled and the FA-mode is ac-coupled. Compared to the DIR-mode, the IV- and FA-modes have higher voltage amplifications, which are measured in section 4.2. Other than coupling difference and the amplification between IV and FA, the FA-mode is offset in such a way that it is assumed that the incoming signal gives a positive pulse to the system, hence giving a higher dynamic range for positive pulses compared to the IV-mode.
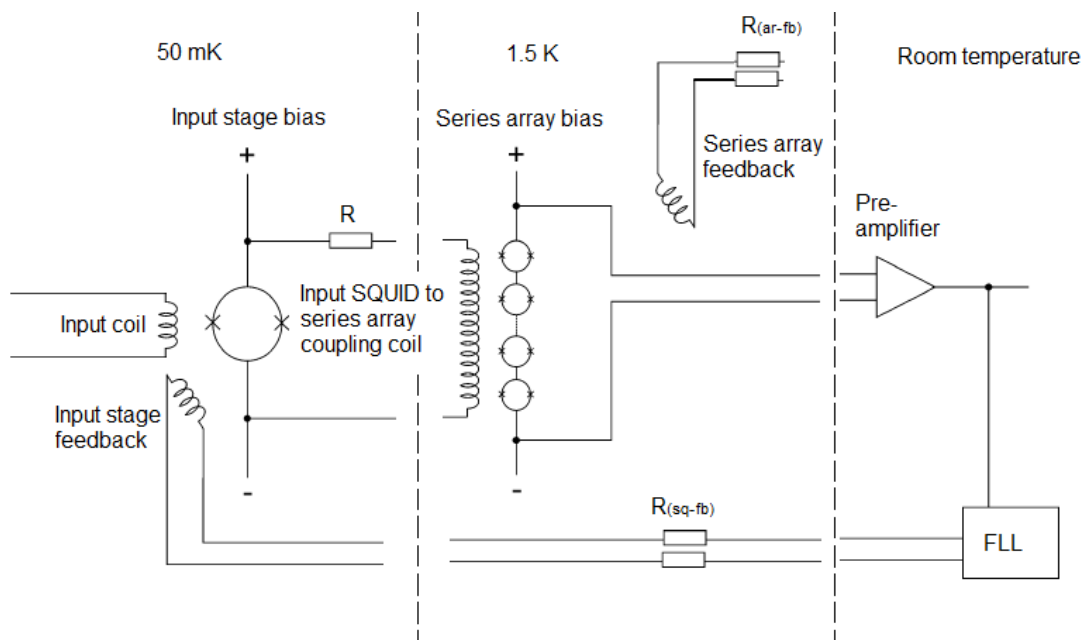
Figure 18. The input circuit of the measured device is coupled to the input SQUID with an input coil. The input SQUID is biased with a measurement dependent optimal bias voltage, and its output is coupled to the series array in the $1.5\,\text{K}$ stage with a 2nd stage input coil. The series array of 100 SQUIDS is also biased with a measurement dependent bias voltage. The output of the series array is connected to the room temperature preamplifier and its output is connected to the SQUID control electronics and flux-locked loop (FLL) controller, which is shown in Figure 21. Both the input SQUID and the series array can be controlled by feedback coils, but only the input stage feedback coil is used in measurements. The series array feedback coil is only used to check that the SQUID array is working properly. The flux-locked loop controller reads the output of the preamplifier which is then used to null the magnetic flux through the input SQUID and thus linearize the response.

38
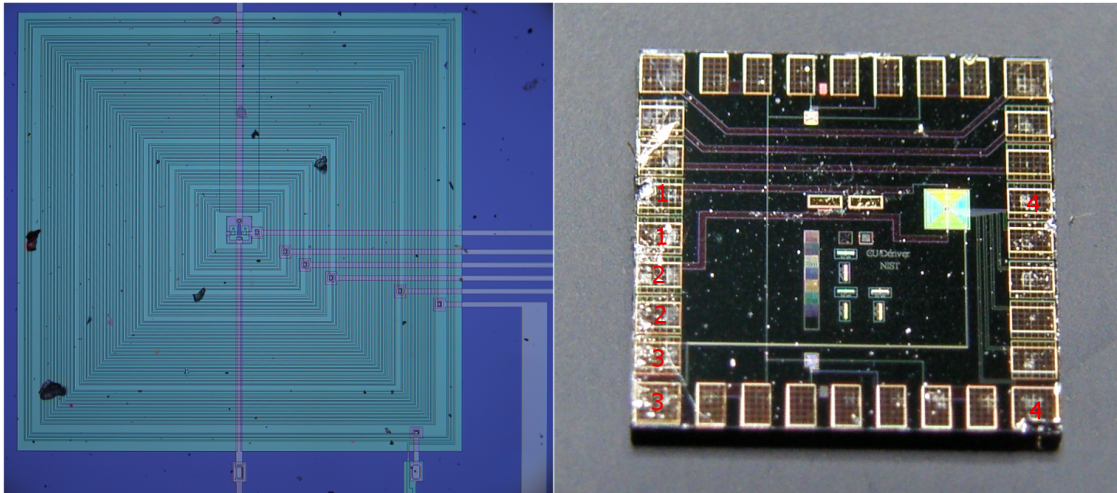
Figure 19. On the left the, a microscope close up of the input stage SQUID, and on the right a macro picture of the whole input SQUID chip. On the right: positive pads (1, bias/output), negative pads (2, bias/output), feedback pads (3), and input pads with multiple possibilities of input coil turns (4).
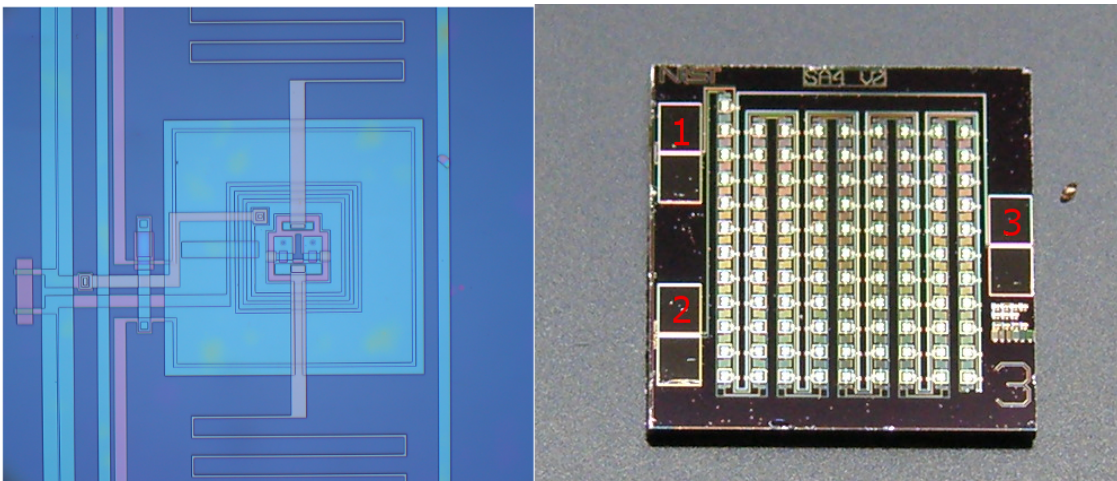

Figure 20. On the left, a microscope close up of one of the 100 SQUIDs in the series array, and on the right macro picture of the whole series array chip. On the right: bias and output pads (1), feedback pads (2), and input pads (3).

3.4 Measurement equipment

The SQUIDs are operated by the room temperature electronics provided by SRON [39], see Figure 21. The power supply unit is connected to an isolation transformer to isolate the SQUID systems ground from the rest of the system. The output of the SQUID remote controller is connected to a spectrum analyzer, Agilent 89410A, see Figure 22, a lock-in amplifier, or a DAQ-card, NI PXI-6281, depending on what is measured. The spectrum analyzer data will be saved to a floppy disc and the DAQ-card is connected to the recording PC via a optical cable.

For transition temperature measurements one lock-in amplifier, Stanford Model SR830 DSP see Figure 23, was used as well as the Ithaco 1201 low noise preamplifier, see Figure 24. The temperature of the sample stage is measured with an calibrated Ruthenium-Oxide (RuOx)-resistor. It is measured as a four wire probe measurement constantly throughout the cooldown, using a resistance bridge and its preamplifier, Figure 25. The measurement connections are discussed later in section 5.1. The oscilloscope used throughout the measurements and preparations was Tektronix TBS 1102B-EDU. The resistance bridge used in the temperature measurements was a Picowatt AVS-47A Resistance Bridge. The hardware PID-controller used in some of the measurements was a Picowatt TS-530 Temperature Controller, see Figure 26. As will be seen later, there is a noticeable difference if the hardware PID (proportional, integral, derivative) controller is used or even connected to the temperature readout. Due to this problem, the software solution, see appendix B, was implemented.

The bias voltages were provided by the SRON-electronics for the SQUID, and regulated dc-batteries and rf-voltage box for the TES. The SRON-electronics provided stable biasing for the SQUID, and the rf-voltage box gave the most stable (least drift in voltage) bias for the TES at the transition, out of all the possibilities available.

For the determination of shunt resistance, the Keithley 6221 dc and ac current source and the Keithley 2182A nanovoltmeter were used, see Figure 27.

3.5 X-Array TES chip

The X-Array TES chip measured was part of a larger project started in 2013 [40]. The chip XA05 F2 was a sample where there is no absorber for the TESs, and there are three different pixel radii $45\,\mu$m, $35\,\mu$m, and $25\,\mu$m. The composition of the Corbino geometry pixel is shown in Figure 28. There are total of 256 pixels in the array, as shown Figure 29, and they are divided into eigth quadrants with respect to their bonding pads. In the measured chip however, pixels from only three of the eight quadrants were measured. Two of those had $35\,\mu$m and one with $25\,\mu$m sized pixels. In Figure 29, gold platforms which can be used to thermalize the chip better
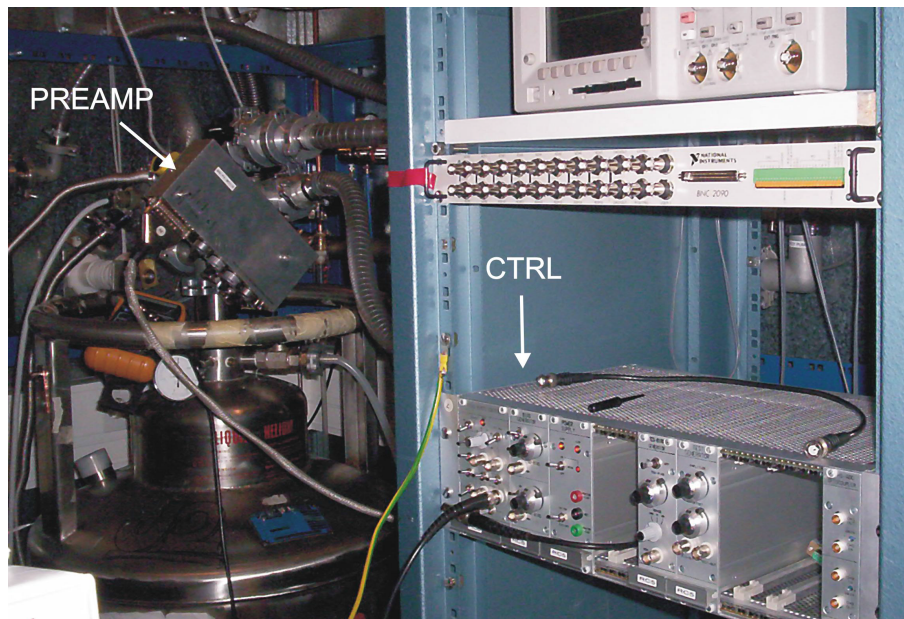
Figure 21. Plastic dilution refrigerator inside a helium dewar. Preamplifier is attached to the cryostat, and the controller electronics can be seen on the right side of the picture in the rack. Modules from left to right: Remote controller, SQ/AR bias generator, power supply, TES-bias generator, test generator and hs-adc optocoupler.
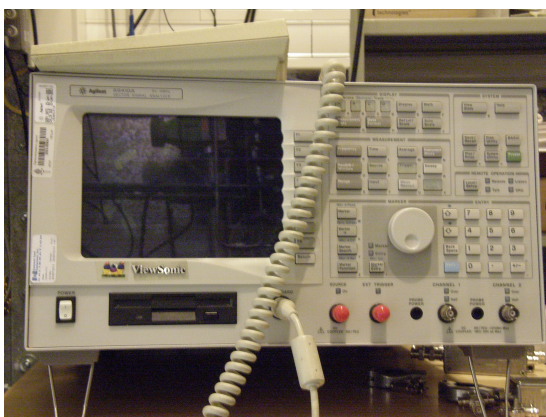
Figure 22. Agilent 89410A spectrum analyzer.
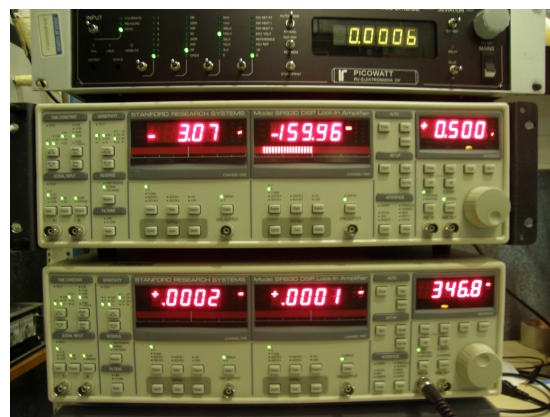
Figure 23. Stanford Model SR830 DSP lock-in amplifier.

Figure 24. Above Agilent 33250A function generator and below Ithaco 1201 low noise pre amplifier.
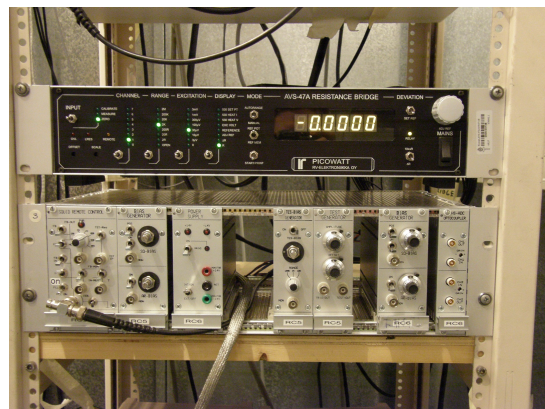
Figure 25. Above AVS-47A resistance bridge and below the SQUID-electronics provided by SRON [39].

Figure 26. Above the TS-530 Temperature controller and below the AVS-47 resistance bridge.

Figure 27. Above Keithley 6221 dc and ac current source and below Keithley 2182A nanovoltmeter.
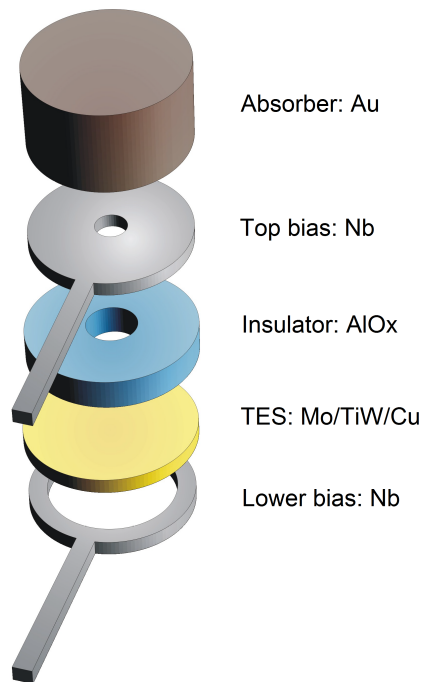
Figure 28. Blowup figure of the Corbino geometry TES. In the measured pixels the absorber was not implemented.

to the sample stage can also be seen.
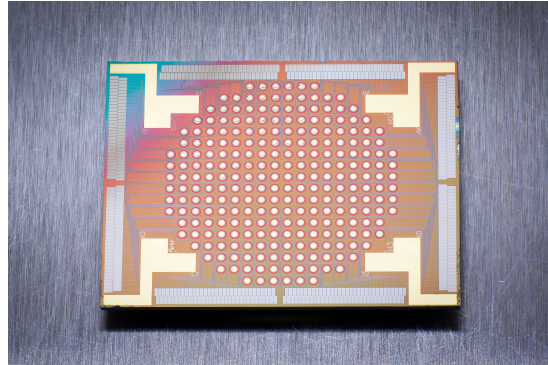
Figure 29. Picture of a similar chip to what was measured. Contrary to the measured chip, the chip in figure has gold absorbers covering all the TES pixels.

4 SQUID measurements, analysis and results

4.1 Modulation and flux-locked loop

The general measurement setup for the whole SQUID system can be seen in Figure 18. The first order of business is to see if the SQUIDs are indeed working properly and that they have not trapped flux during the cooldown. This is done by measuring the modulation curve for the series array as well as the input SQUID. The driving electronics for the SQUID were shown in section 3.4 and the room temperature electronics by SRON can be seen in Figure 25.

4.1.1 Series array bias optimization

The output of an ac-signal generator (Agilent 33250A/tektronix AFG3102, see Figure 24) is connected to the signal line of the SQUID remote controller and the mechanical switches are FC to SI, X to SIG and Y to in-mon, see Figure 30. Everything else is not connected. Output is then taken from the remote Y and is connected by a coaxial cable to a oscilloscope Y, and the reference signal from the function generator is connected also to the oscilloscope X. Now the signal travels from SIG into the series array feedback coil directly, and the output is preamplified and can be read from the Y output, see Figure 30. Biasing for the series array is taken from the bias generator, the second box from on the left in Figure 25, which is connected to the back of the remote controller with a short coaxial cable. The remote controller is in its turn connected to the preamplifier which is connected to the cryostat lines, providing bias and feedback to the series array. Now a triangular signal is applied from the function generator to the series array feedback coil. This signal has high enough frequency so the whole width of the signal can be seen in real time, and a small amplitude in order not to damage the feedback coil, usually $100\,\mathrm{Hz}$ and 1-1.2 V peak to peak ramp wave was used. Then one starts to increase the bias voltage for the series array. As can be seen in Figure 31, the modulation starts developing peaks, but some parts stay flat (blue line). These peaks correspond to a flux where there is voltage difference across the Josephson junction array and the flats correspond to the array being fully in the superconducting state. A maximum depth of the modulation curve can be found, which means that the amplitude of the curve reaches a maximum, see $V = 645\,\mathrm{mV}$ in Figure 31. If the bias voltage is increased futher, the modulation depth decreases.
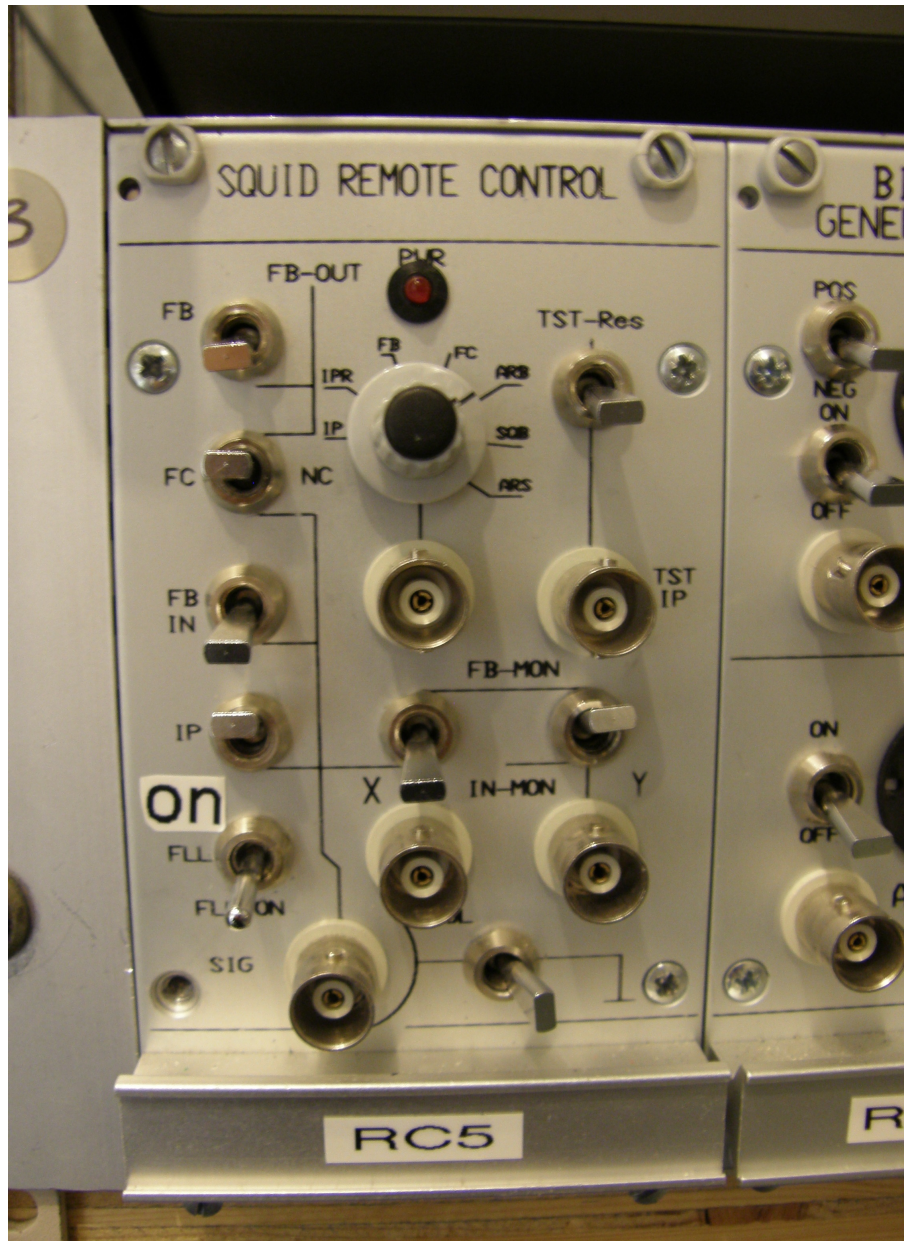
Figure 30. Close up image of the SQUID remote controller. On the left, the signal line. Outside signal can be used, for example ac-signal to produce the modulation curve in the optimization phase, see section 4.1.1, or the feedback can be controlled in FLL, see section 4.1.5. Bottom right, output selection (Y). The How-To is explained in text.
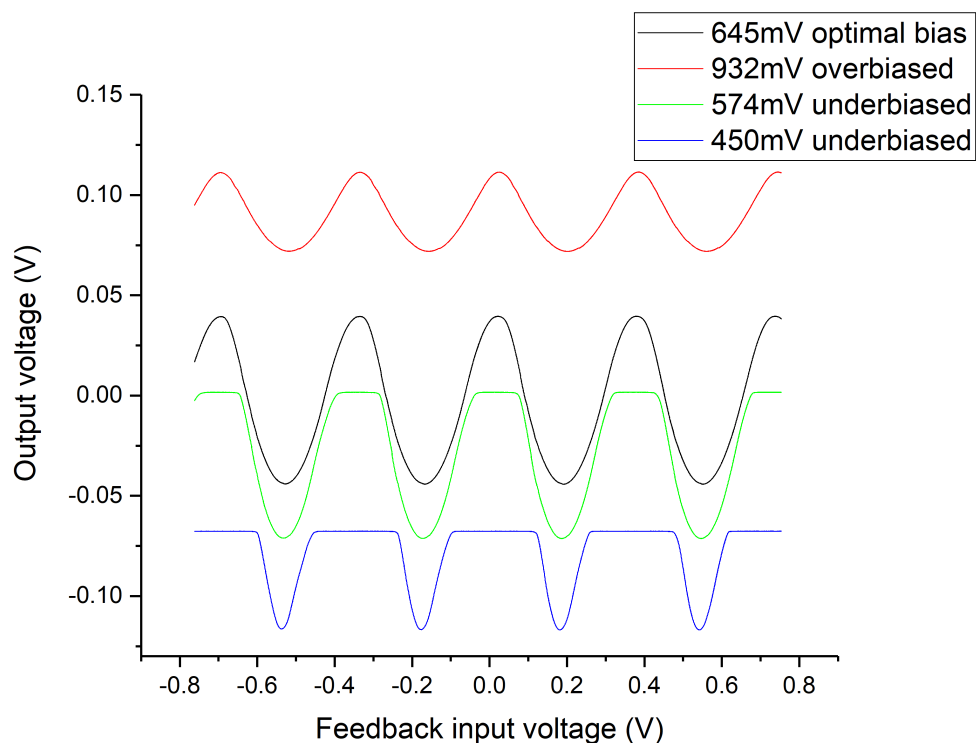
Figure 31. The modulation of the series array, different bias values are shown. The curves are offset to show the modulation and peak behavior more clearly. The modulation begins to show peaks once the bias voltage has been increased enough for the generated bias current to become larger than the critical current of the junctions. (blue and green lines). The flats disappear once the bias voltage is increased even further, and there is an optimal value where the flats are not present and the depth of the modulation output voltage is maximized (black line). If the bias voltage is increased even higher, the superconductivity of the tunnel junctions starts to be suppressed and the modulation depth decreases (red line).

4.1.2   Series array $V - \Phi$ measurement

After the optimal array bias voltage has been found, the function generator output and the remote controller output are connected to a DAQ-card instead of the oscilloscope, this transfers the data through an optical cable to the recording PC. Usually a much smaller frequency is used when recording, due to the speed limitations of the DAQ-card. 4 mHz was used throughout the measurements unless otherwise stated. Figure 31 shows an example of the optimal, under- and overbiased modulation curves for the series array.

4.1.3   Input SQUID bias optimization

Measuring the modulation for the input SQUID is more or less the same process. The series array bias is left at the optimal value, but the function generator input is changed from the series array feedback coil to the input SQUID feedback coil through changed settings at the remote controller. The switches are then FC to NC, X to SIG, Y to in-mon, FB-IN to SIG, FB to FB out. Now the signal travels from the SIG into the feedback controller (FBC), which attenuates the signal and directs it to the input SQUID feedback circuit, and the output of the SQUID chain is read again after preamplification. Now the output signal from the function generator goes into the input feedback coil, and the modulation of the input SQUID is amplified by the series array. The amplification is not purely linear, and the modulation curve for the total SQUID chain can be sinusoidal, see Figure 32, or quite different from a simple sinusoidal shape, see Figure 36 in section 4.2.1. The function generator signal is turned on again and increased to around 2.2 V to see the full nature of the modulation, not just one peak. The bias voltage of the input SQUID is then increased, with similar behaviour happening as it did with the series array. Peaks start to develop once the threshold for critical current is overcome. Again, modulations with different bias voltages are recorded with the PC. Although the series array bias voltage was optimal in the first case, it might be that for the total modulation curve this needs to be adjusted slightly, see Figure 33.

4.1.4   Input SQUID $V - \Phi$ measurement

Now that the optimal bias voltages has been found, the function generator output and the SQUID remote controller output are connected to a DAQ-card which transfers the data through an optical cable to the recording PC. Usually a much smaller frequency is used when recording, due to the limitations of the DAQ-card, 4 mHz is used throughout the measurements unless otherwise stated. Figure 32 shows the optimal, under and over biased modulation curves for the total modulation. Figure 33 shows the effect of series array bias for the total modulation.
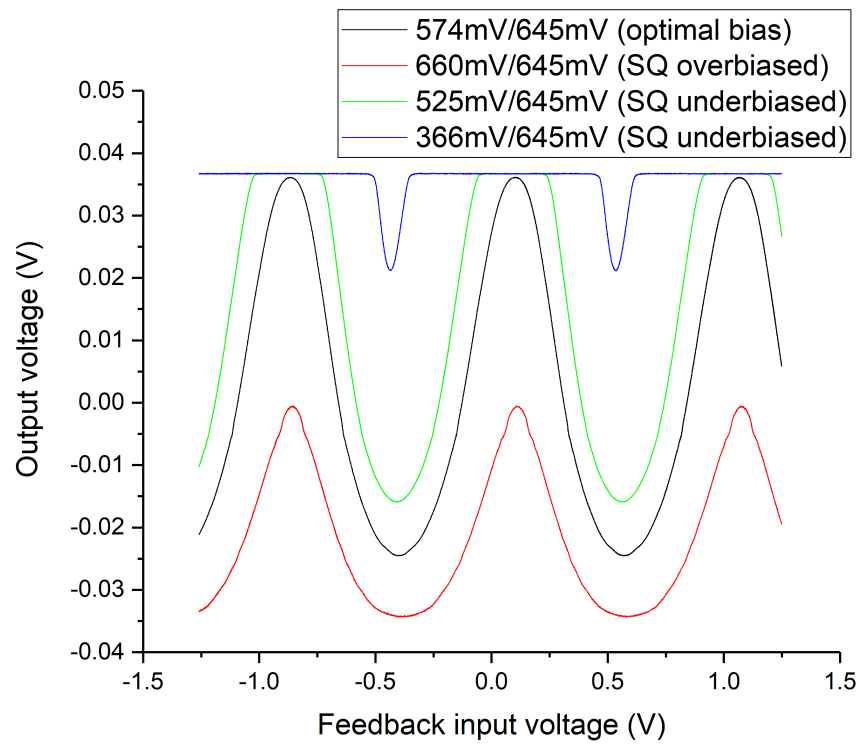
Figure 32. The modulation of the total SQUID chain with optimal series array bias and varying input SQUID bias. The total modulation starts developing peaks (blue line) once the bias voltage is increased. The peaks flats diminish (green line) and at the end disappear and the maximum modulation depth is found (black line). The suppressing of supercurrent at high bias voltages decreases the modulation depth.
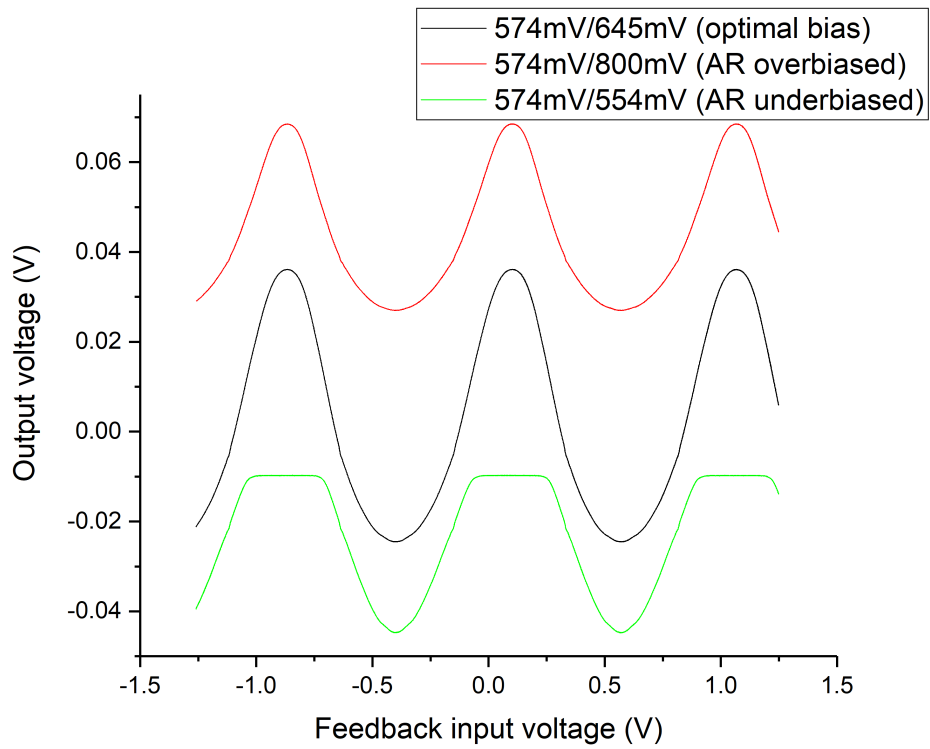
Figure 33. The modulation of the total SQUID chain with varying series array bias and optimal input SQUID bias. If the series array bias is not optimal, it can be the limiting factor, as seen in the red and green lines.

4.1.5 Flux-locking the input SQUID

Now that the modulation of the total SQUID chain has been recorded and the optimal values are found for the current measurement, the input SQUID is set to operate in FLL-mode. The dc offset on the preamplifier can be used to move the modulation curve to a more convenient position on the oscilloscope screen, for example for the modulation curve to have its midpoint at the origin of the oscilloscope, in order to make the input SQUID working point determination a little easier. Next the feedback signal that was used to determine the optimal bias voltages is removed and a dc bias voltage supply is connected to the signal line, see Figure 30. The dc bias voltage is varied so that the working point of the input SQUID is at the steepest part of the increasing side and in the lower half of the modulation curve, in order to maximize the dynamic range of the SQUID chain. The TES-bias module is used for the working point biasing, see fourth module from the left in Figure 25. It is uncalibrated, but the absolute value of the working point bias is irrelevant, as it only serves the purpose to bias the input SQUID and holds no value in terms of measurement results. Now the following switch changes are made to the remote controller in order: FLL to On, Y to FB-MON and FB-IN to OFF, also the TES-bias is removed from the remote controller signal input. Now the signal is generated by flux through the input SQUID, and then preamplified by the series array as well as the preamplifier, and then the FBC sends this signal to both the input SQUID feedback coil to null the flux which generated the signal, and a copy, which it amplifies with mode dependent (DIR, IV, FA) amplification and this signal can be read from Y. When Y is flipped from IN-MON to FB-MON the position of the dot in the oscilloscope might change due to the rapid change or shock into the SQUID circuit. This only poses a problem if the SQUID FLL unlocks. Unlocking can be seen from two factors: there is a led indicator on the preamplifier that shows if the FLL lock is lost, and the sample stage temperature starts increasing due to rapid oscillations in the SQUID. Now depending on what is going to be measured next, the switch on the preamplifier can be set to DIR, IV or FA.

4.2 Mutual inductance and amplification

The mutual inductances between the different coupling coils and the SQUIDs are important parameters that can be used to find out the total amplification of the SQUID chain *in situ*. The amplification of the SQUID chain is different every cooldown and every time the SQUIDs are in FLL-mode. If the lock is lost, the amplification may change slightly for the new locked position.

50
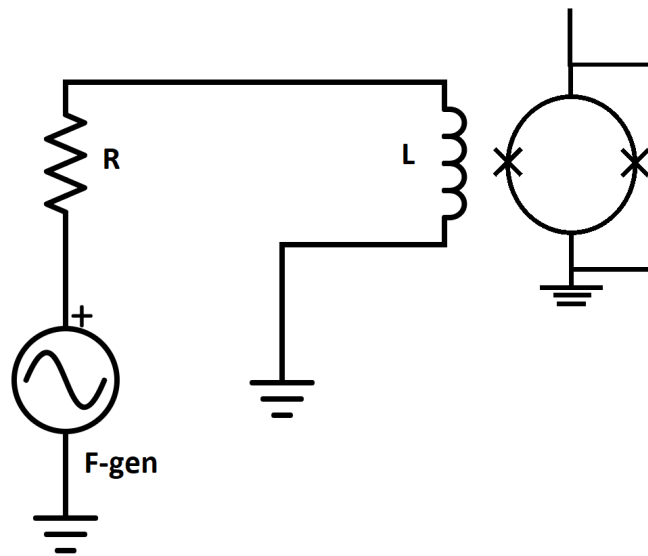
Figure 34. The measurement setup for mutual inductances and gain determination between DIR-, IV- and FA-modes. For mutual inductances the input circuit represents input coupling coil coupling to the input SQUID, input stage feedback coupling coil coupling to the input SQUID, or series array feedback coil coupling to the series array. For the preamplifier gain setup, the input circuit is connected to the input coupling coil of the input SQUID, and the variable part is the mode switch at the preamplifier.
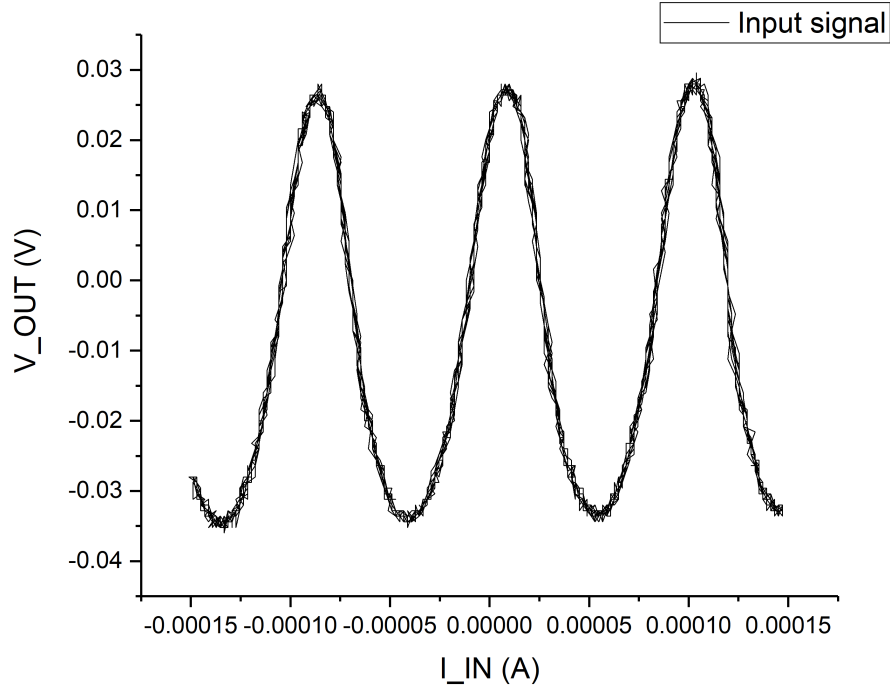
Figure 35. The mutual inductance of the input coupling coil can be determined empirically from the plot, $M = \Phi_0/P$, where P is the period of modulation in current units, see [10]. Mutual inductance of the input coupling coil is $M_{IN}^{SQ} = 21.5\,\text{pH}$.

4.2.1 Mutual inductances of the coupling coils

The measurement is simple, following the circuit diagram in Figure 34. The input and output voltages are measured for each case, and with known resistances in the input circuit, the input voltage can be converted into input current. For the feedback coupling coils, for both the series array and the input SQUID, the preamplifier was taken out of the setup, and a voltage amplifier (Ithaco 1201 low noise pre amp) was used to amplify the output voltage from the series array. An ac signal, $1\,\text{Hz}$ $V_{pp} = 700\,\text{mV}$, was produced by Agilent 33250A function generator in order to have a known input signal. For the input SQUID coil, the measurement was carried out with the preamplifier, but with a known input signal with $V_{pp} = 1500\,\text{mV}$ due to higher resistance in the circuit.

The mutual inductances for each of the three coupling coils, input-, input SQUID feedback-, and series array feedback coil can be determined by an empirical method. The determination of mutual inductance is $M = \frac{\Phi_0}{P}$, where P is the period of current modulation in current units [10], shown in Figures 35, 36 and 37.

52
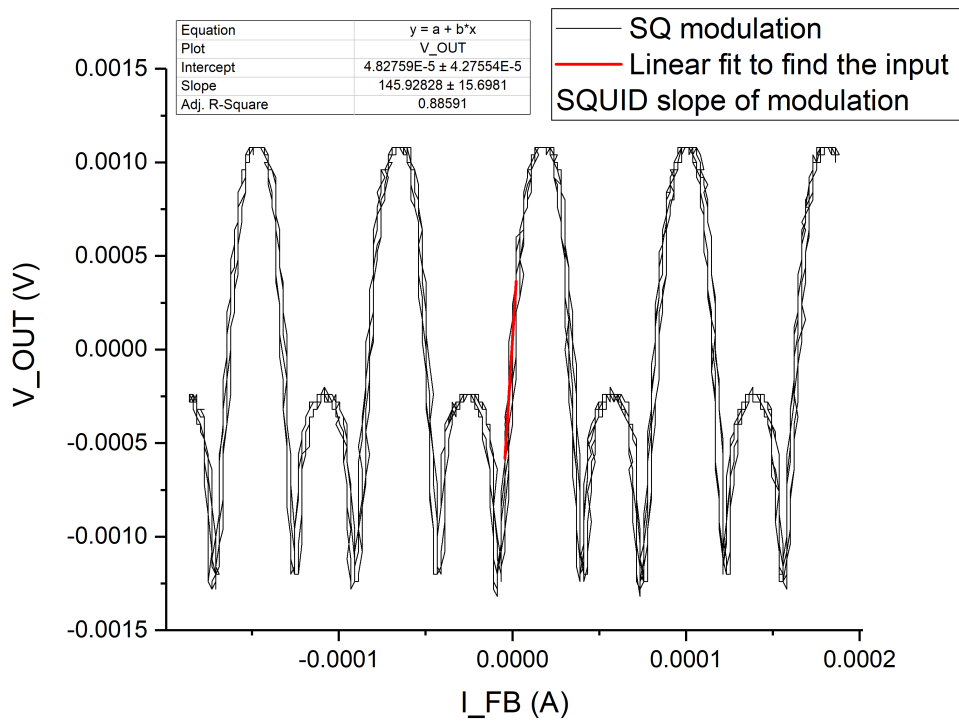
Figure 36. Mutual inductance of the input SQUID feedback coupling coil can be seen from the plot, $M = \Phi_0/P$, where P is the period of modulation in current units, see [10]. Mutual inductance of the input SQUID feedback coupling coil is $M_{IN}^{SQ} = 25.1\,\mathrm{pH}$. The slope of the modulation with the input current mutual inductance can be used to determine the gain of the SQUID, see section 4.2.3 for more details.

Equation	y = a + b*x
Plot	V_OUT
Intercept	-0.00117 ± 1.70955E-5
Slope	39.12089 ± 0.77387
Adj. R-Square	0.98839

Figure 37. Mutual inductance of the series array feedback coupling coil can be seen from the plot, $M = \Phi_0/P$, where P is the period of modulation in current units, see [10]. Mutual inductance of the series array feedback coupling coil is $M_{IN}^{SQ} = 9.2\,\text{pH}$. The slope of the modulation with the input current mutual inductance can be used to determine the gain of the SQUID, see section 4.2.3 for more details.
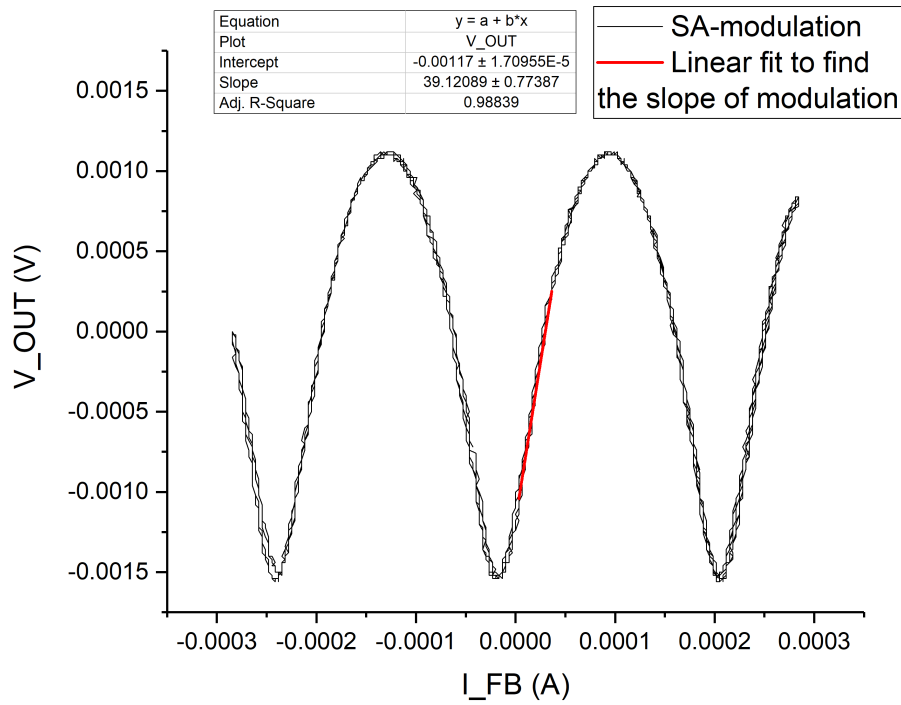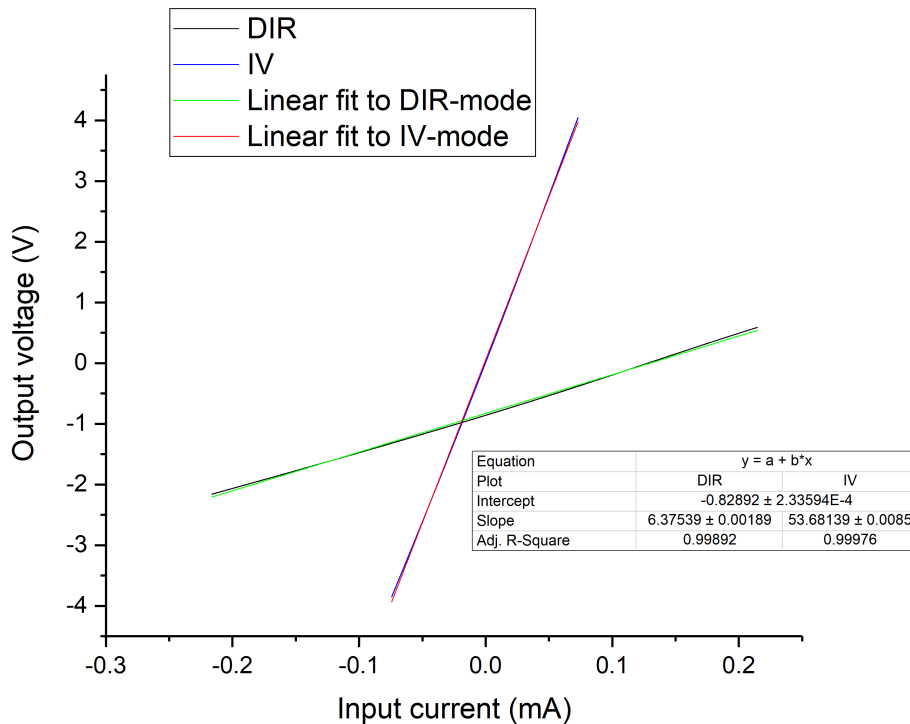
Figure 38. Measured gains of DIR- and IV-modes. The gain between the two modes can be found when dividing IV-mode with DIR-mode slope. This gives 8.42.

4.2.2 Room temperature amplification

The total gain of the preamplifier in FLL is determined in a few steps. First, the pre-amplifier has a specific gain which stays constant, 97.7. Then there is a attenuation depending on the load impedance, to a $50\,\Omega$ load it is 0.058 and to a $1\,M\Omega$ load it is 0.23. If a measurement is carried out in IV- or FA mode, there is also another factor. For IV mode, there is a constant factor of 8.42, which is the amplification factor between DIR and IV, see Figure 38. For FA, there is an amplification of 68.25, see Figure 39. For a typical measurement of noise, preamplifier in FA-mode, the total amplification of the external chain to a $1\,M\Omega$ load is 1533.6. The DIR and IV-mode amplifications to the same load are 22.5 and 189.2, respectively.

The signal gain of the SQUID chain can be measured when the SQUID is in FLL. The measurement circuit can be seen in Figure 34. The function generator is connected to the input coil of the input SQUID through a bias resistor. First the function generator and remote controller outputs are connected to an oscilloscope to see that the small frequency input signal indeed provides a slope. A $R_0 = 9974\,\Omega$ resistor was used to have small enough bias currents into the input coil. The gain setting on the preamplifier (potentiometer) was set to exactly 5.00 and was kept

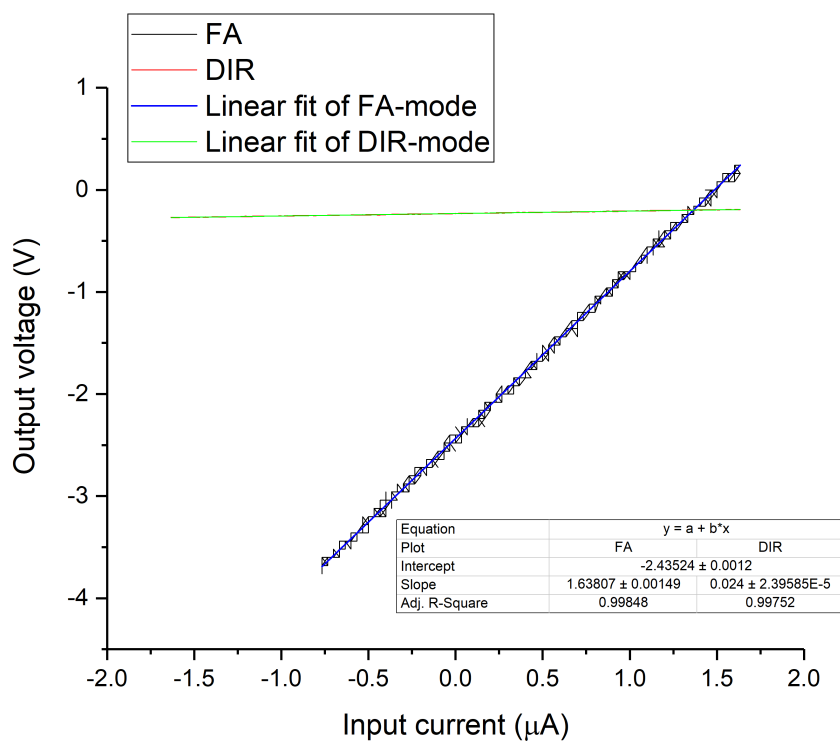| Equation	y = a + b*x	
Plot	FA	DIR
Intercept	-2.43524 ± 0.0012	
Slope	1.63807 ± 0.00149	0.024 ± 2.39585E-5
Adj. R-Square	0.99848	0.99752

Figure 39. Measured gains of DIR- and FA-modes. The gain between the two modes can be found when dividing FA- mode with DIR-mode slope. This gives 68.25.

there throughout all the measurements. It was found that with input voltages above 750 mV in the IV-mode that the SQUID was hitting the output limits and the FLL started unlocking. The gain was also measured in the DIR-mode. The input voltage from the function generator as well as the output voltage from the remote controller is recorded by PC. The recorded data can be seen in Figure 38. Later the relation between DIR- and FA-modes was measured. The input circuit for that is shown in Figure 14, except the bias voltage source is changed to a function generator with an ac signal, and the current through the TES side of the circuit is calculated from Kirchoff's laws. The input signal was $V_{pp} = 200$ mV, 200 Hz.

4.2.3 Empirical determination of SQUID amplification

The SQUID is used as a flux-to-voltage transformer and the amplification factor can be measured *in-situ*. Due to the fact that input currents cannot always be known or measured directly, but the input flux can be determined from measuring the modulation of the feedback coil, the currents can be determined from the output voltages.

The input flux has the following relation

$$\phi_{in} = M_{in}I_{in} = M_{FB}I_{FB}, \tag{49}$$

where $M_{in/FB}$ is the mutual inductance of the input coil and the SQUID, and feedback coil and the SQUID, and $I_{in/FB}$ are the currents through the coils. Because the feedback coil is used to null the flux through the SQUID, the input flux is same for both cases, hence the equality between input and feedback equations. The SQUID gain can be defined as:

$$G_{SQUID} = \frac{\partial V_{out}}{\partial I_{in}} = \frac{\partial V_{out}}{\partial \phi_{in}}M_{in}. \tag{50}$$

Both of these factors will be determined empirically, but only the flux-to-voltage differential is dependent on the measurement. The mutual inductances of the coils and the SQUID can be found from the modulation curves of the SQUID, with the relation

$$M = \frac{\phi_0}{P}, \tag{51}$$

where the P is one period of modulation in current units, as discussed in section 4.2.1. The differential can be further opened to produce empirically measurable observables:

$$\frac{\partial V_{out}}{\partial \phi_{in}} = \frac{\partial V_{out}}{\partial V_{FB}}\frac{\partial V_{FB}}{\partial \phi_{in}}, \tag{52}$$

where the first differential is the slope of the modulation at the working point of the SQUID and the second is the flux to voltage dependency of the modulation, if the change of flux is Φ_0 then the second differential is the period of modulation. Hence it can be seen that the input flux can be determined from the modulation of the

feedback circuit. Hence measuring the modulation curve, the amplification of the SQUID can be determined.

The total amplification of the SQUID chain is then found by multiplying both of the the the amplification factors together, which results in current to voltage amplification $G_{tot} = G_{PA} \cdot G_{SQUID}$. Calculating the total amplification from Figure 32 optimal bias would end up

$$G_{tot} = G_{PA}^{FA} \cdot G_{SQUID} = G_{PA}^{FA} \cdot \frac{\partial V_{out}}{\partial V_{FB}} \cdot \frac{\partial V_{FB}}{\partial \phi_{in}} \cdot M_{in}$$

$$= 97.7 \cdot 0.23 \cdot 68.25 \cdot 0.2 \cdot 0.96 \frac{V}{\Phi_0} \cdot 21.5 \, \text{pH} = 3061358.6 \frac{V}{A}$$

where the slope from the modulation curve was estimated to be 0.2 between 0 and 0.1 V output voltages and the period of modulation is 0.96 V. Typically the SQUID amplification was between 700 and 2000 V/A for a good measurement, and during the measurements the total amplification was 1-3 $\cdot 10^6$V/A for FA-mode with a 1 MΩ load.

4.3   SQUID noise

4.3.1   SQUID noise measurements

The SQUID noise measurements were done for all but the first measurement with an open loop. The measurement circuit is shown in Figure 18, and the Agilent 89410A Spectrum analyzer was used to record the spectrum. The first measurement, see Figure 40, had input circuit corresponding to Figure 34, i.e. a function generator at the input. There were three cooldowns for the SQUID noise measurements, runs 175, 177, and 185[2]. For each measurement the preparations are the same. First, measure the modulation of the total SQUID chain, in order to find the amplification, see section 4.2. Second, lock the SQUID (FLL). Last, connect the spectrum analyzer into the output of the SQUID remote controller (Y). A predefined set of settings are used in all the measurements, which define the averaging (500 points), 1601 points per spectrum, and the output units of the spectrum (V^2/Hz). This is done by loading a state from a floppy disk always after turning the spectrum analyzer on. The spectra are measured in six parts, 5-100Hz, and every decade between 100 Hz and 10 MHz. The spectra are saved onto a floppy disc and the raw data is transformed into ASCII form.

For measurements in run 175, the input SQUID input coupling coil was connected to the cryostat lines, and this made it possible to add a series resistance and to measure the noise induced cut-off by introducing a signal into the circuit. For Figure 40,

---

[2]The number bears no other meaning than is the running number used to keep track of the cryostat cooldowns, hence the jump between the noise measurement numbers.

there was an input signal ($10\,\mathrm{mV}_{rms}$, white noise) generated by the Agilent 33250A function generator, which was connected to a series resistor with $9997\,\Omega$ resistance. The wire resistance in the circuit was $R_{wires} = 204.5\,\Omega$. For the measurement in Figure 41 the series resistance was disconnected, and the input circuit had two floating ends of the wires. The measurement temperature for both of these measurements was $91\,\mathrm{mK}$. The effects of these resistances is discussed in 4.3.2.

Between the runs 175 and 177, the connection between the input SQUID input coupling coil and the cryostat lines was removed. Measurements were done in a similar way as for the run 175 without input signal. The measurement temperature was again $91\,\mathrm{mK}$.

Between the runs 177 and 185, there was again differences made for the input SQUID input circuit. The wire length was increased, with the same NbTi superconducting wiring discussed in section 3.1, however the ends still remained floating. The measuring temperature for run 185 was $620\,\mathrm{mK}$ due to cooldown problems.

4.3.2 SQUID noise analysis

For simplest circuits, the cut-off frequency is inversely proportional to the time constant, and the relations for RC and RL circuits are the following

$$f_c = \frac{1}{2\pi\tau_{RC}} = \frac{1}{2\pi RC},\tag{53}$$

$$f_c = \frac{1}{2\pi\tau_{RL}} = \frac{R}{2\pi L}.\tag{54}$$

Thus the following fits can be used to determine the cut-off frequencies from the spectra:

$$I_N = \frac{I_{white-noise}}{\sqrt{1 + \left(\frac{2\pi f}{RC}\right)^2}},\tag{55}$$

$$I_N = \frac{I_{white-noise}}{\sqrt{1 + \left(\frac{2\pi f L}{R}\right)^2}},\tag{56}$$

where $I_{white-noise}$ is the current white noise level. In fitting, the following substitution has been made $A = f_c = \frac{1}{2\pi\tau}$ in order to get the cutoff frequency as the parameter A. The fit gives a white noise level $85\,\mathrm{pA}/\sqrt{\mathrm{Hz}}$, see Figure 40, which is the correct order of magnitude as the calculated value is $10\,\mathrm{mV}_{rms}/(10201.5\,\Omega \cdot \sqrt{50\,\mathrm{MHz}}) \approx 140\,\mathrm{pA}/\sqrt{\mathrm{Hz}}$, where $50\,\mathrm{MHz}$ is the noise bandwidth of Agilent 33250A. The real value of the L_{IN} is not known, but is in the order of magnitude tens or few hundreds of nH [10] for both, the series array input inductance as well the input SQUID input inductance. If the simplest RL circuit would hold, equation (56), we
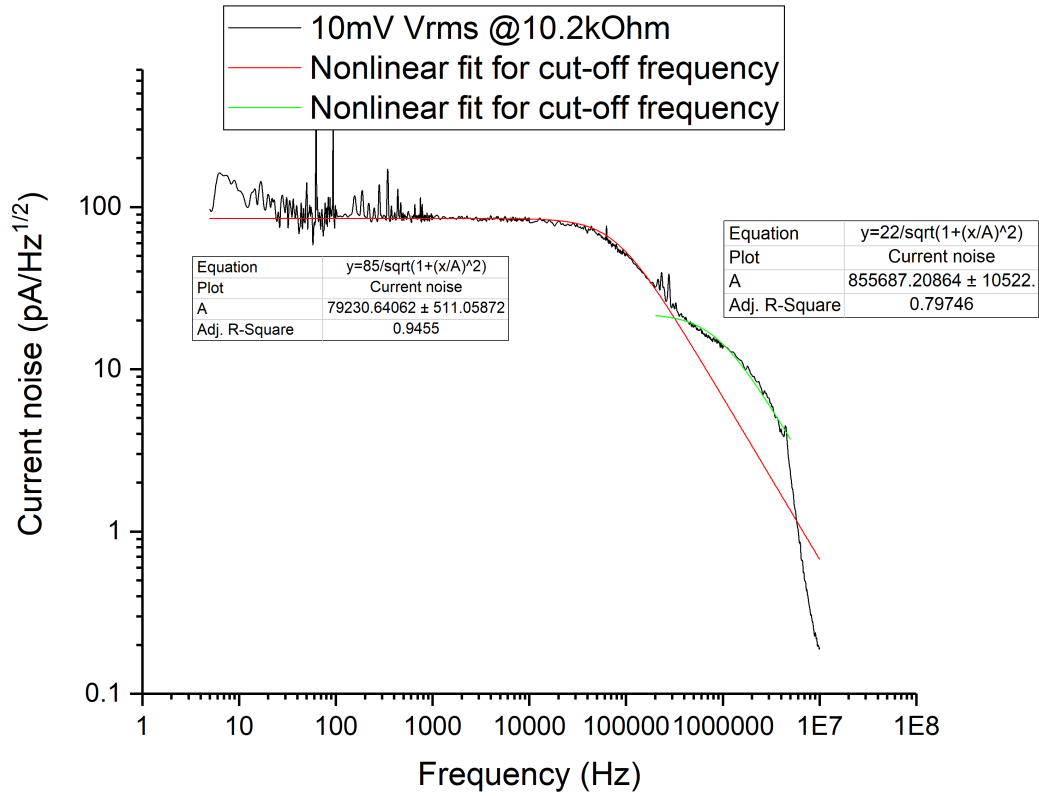
Figure 40. Measured SQUID noise spectrum with input circuit as in Figure 34 with $10\,\text{mV}_{rms}$ input white noise signal and $9997\,\Omega$ bias resistor and $204.5\,\Omega$ wire resistance. Two cut-offs are fitted at $79.2\,\text{kHz}$ and $855.7\,\text{kHz}$. The last cut-off around $5.4\,\text{MHz}$ is due to the preamplifier, which is not fitted. Fitting function $y = \frac{y_0}{\sqrt{1+\frac{x^2}{A^2}}}$ was used, where y_0 is the white noise level, and $A = \frac{2\pi}{\tau} = f_c$.

60
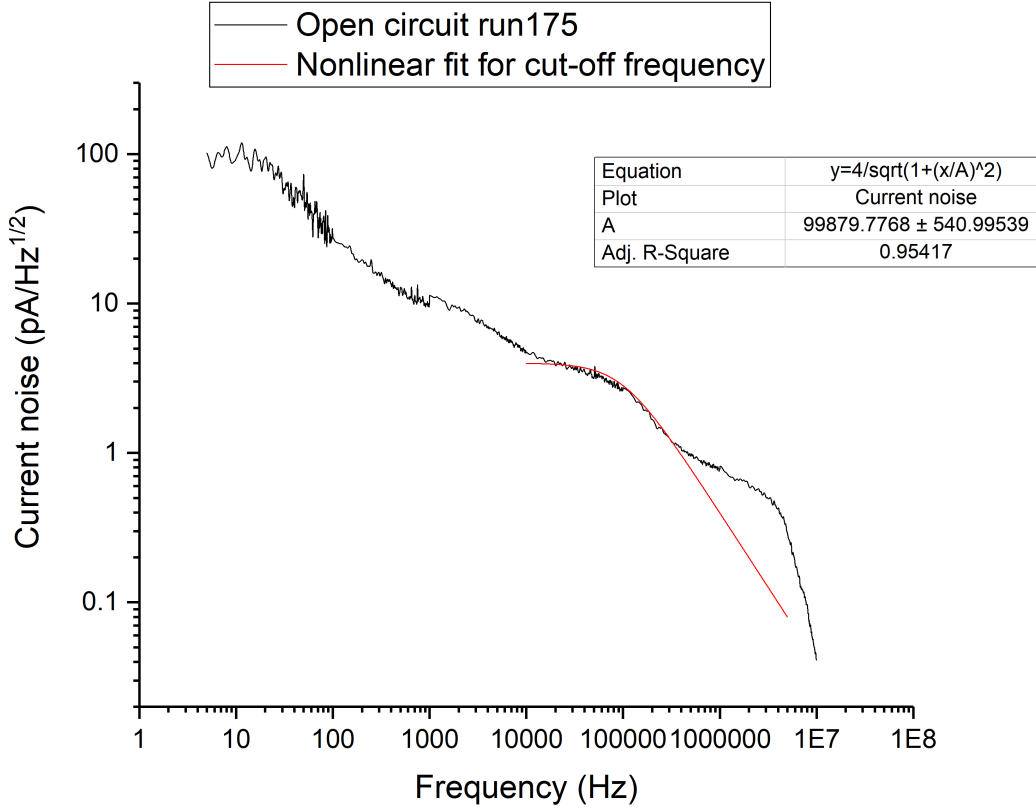
Figure 41. Measured SQUID noise spectrum with an open input circuit loop, cryostat wiring connected. At least two cut-offs are visible, 99.9 kHz, which is fitted, and the cut-off from the preamplifier around 5.4 MHz. There is a lot of $1/f$-noise visible in the measurement. Fitting function $y = \dfrac{y_0}{\sqrt{1+\frac{x^2}{A^2}}}$ was used, where y_0 is the white noise level, and $A = \frac{2\pi}{\tau} = f_c$.

could calculate L_{in} from the cut-off frequency value. However, neither cut-off in Figure 40 gives a realistic value for L. We must conclude that a more complex circuit model is needed to understand Figure 40.

The cut-off at 855.7 kHz in Figure 40 is could be due to the τ_{RL} of the input SQUID to series array coupling circuit. The series resistance in the circuit is $R_{SQ-SA} = 0.44\,\Omega$, while leads to an estimate $L_{SA} = 82\,nH$ which is reasonable as the series array coupling coil inductance. The last cutoff at 5.4 MHz is due to the room temperature preamplifier. The 855.7 kHz cut-off can perhaps be attributed to the array input response, due to the lack of this cut-off in the non-biased measurements.

The intrinsic series array noise floor can be seen in Figure 41, at $f >$ 100 kHz, being approximately $1\,\mathrm{pA}/\sqrt{\mathrm{Hz}}$. However, this noise floor was not reach in later measurements. The noise level around 100 kHz cut-off in Figure 41 is tentatively consistent
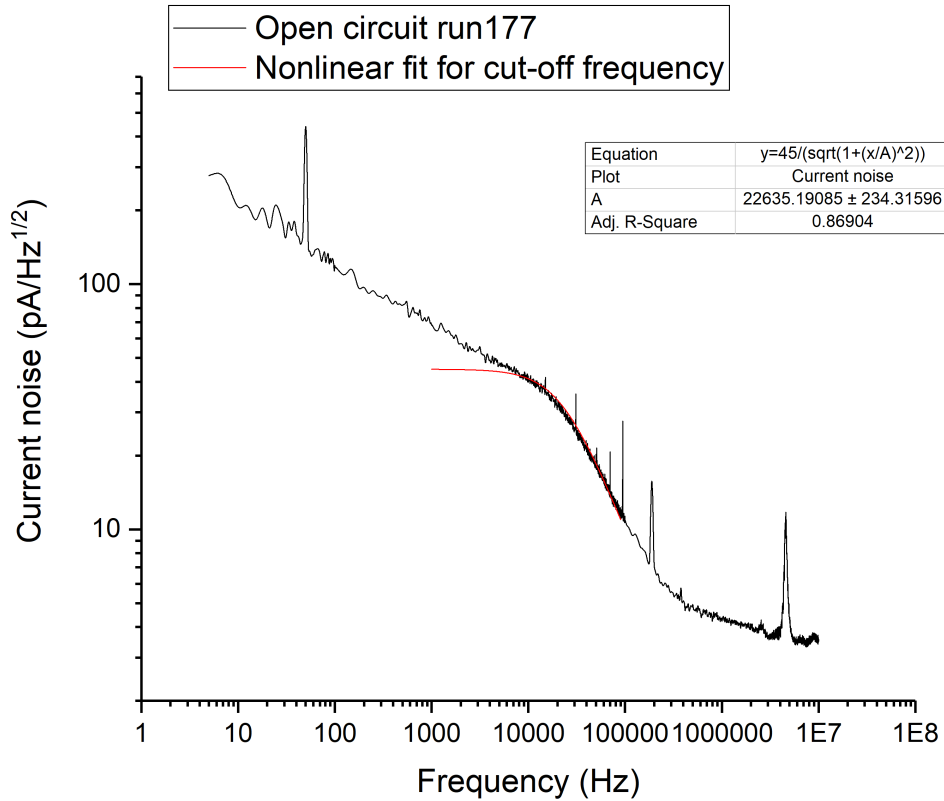
Figure 42. Measured SQUID noise spectrum with an open input circuit loop, no wiring connected. Only one clear cut-off is visible at 22.6 kHz, and a resonance is found at around 5.4 MHz. Fitting function $y = \dfrac{y_0}{\sqrt{1+\frac{x^2}{A^2}}}$ was used, where y_0 is the white noise level, and $A = \frac{2\pi}{\tau} = f_c$.

with Johnson noise from the combination of the resistor between the input SQUID output and the series array input coil plus the input SQUID dynamical resistance. For the temperature 91 mK and a total resistance of 1.4 Ω, equation (33) results in noise level of $1.9\,\text{pA}/\sqrt{\text{Hz}}$. This summed with the series array noise floor is slightly less than the to the cut-off noise level in Figure 41. Noise below 100 kHz looks like $1/f$-noise, whose source is currently unknown.

In Figure 42, there is only one cut-off found around 20 kHz. Finding a resistance value which would generate the noise level present at the cut-off at 91 mK temperature can be found with equation (33), giving $R = 2.48\,\text{m}\Omega$. If it is in parallel with the input coil, its inductance can be evaluated to be 17 nH, which is still a reasonable value. However, there is no other direct evidence of such a shorting of the input coil, and, as can be seen in Figure 43, such cut-off was not present later. Suprisingly, the overall noise level is much higher than before.
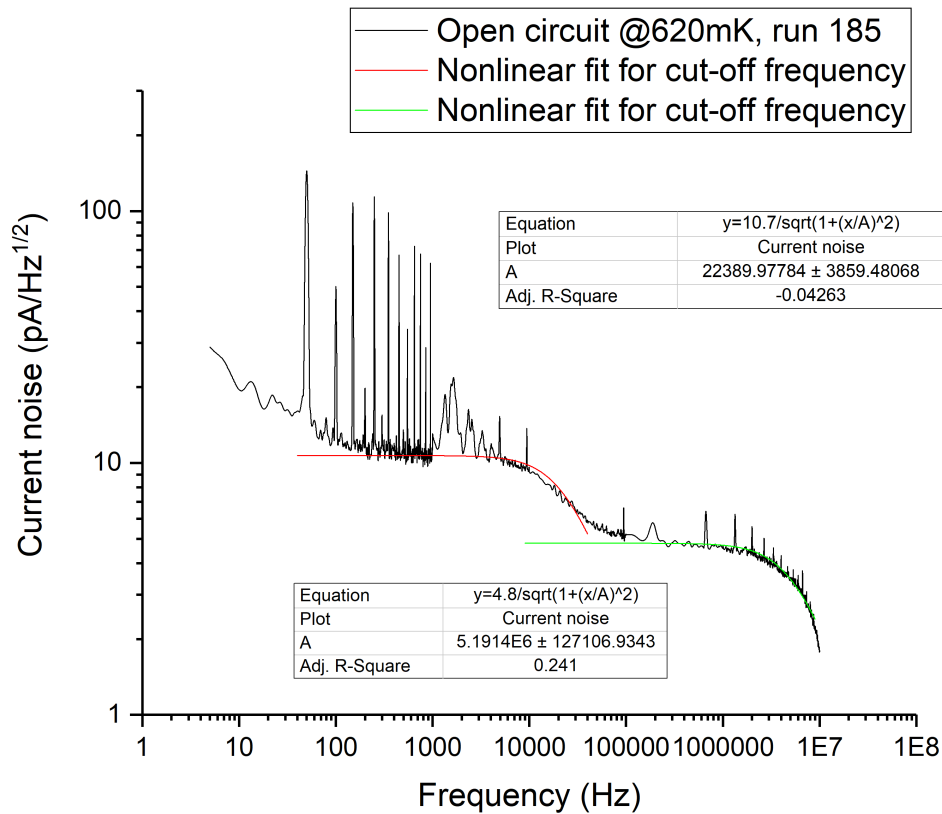
Figure 43. Measured SQUID noise spectrum with an open input circuit loop. Two cut-offs are fitted at $22.4\,\mathrm{kHz}$ and $5.4\,\mathrm{MHz}$. The circuit shows $1/f$-noise below $100\,\mathrm{Hz}$ frequencies. Fitting function $y = \dfrac{y_0}{\sqrt{1 + \frac{x^2}{A^2}}}$ was used, where y_0 is the white noise level, and $A = \frac{2\pi}{\tau} = f_c$.

In run 185, see Figure 43, after resoldering some of the wire connections, the overall noise level went down significantly, showing much less $1/f$-noise. The two white-noise plateaus are fitted, giving $10.7\,\mathrm{pA}/\sqrt{\mathrm{Hz}}$ below $22\,\mathrm{kHz}$, and $4.8\,\mathrm{pA}/\sqrt{\mathrm{Hz}}$ below $5\,\mathrm{MHz}$. As already calculated earlier, these noise levels can perhaps be explained by the input SQUID Johnson noise and the series array Johnson noise.

For all the noise measurements, a peak at $50\,\mathrm{Hz}$ and its multiples can be seen to some extent. This is due to the electronic interference from the powering of all the equipment, even though care has been taken in order to reduce these peaks to a minimum.

4.4   Problems and unknowns

One of the bigger difficulties during the analysis was that the design parameters of the SQUIDs were unknown, especially the input inductance. The resistors added to the circuits outside the SQUID chips were measured or known from prior measurements.

In some of the SQUID noise measurements, there seemed to be shortcircuited somewhere in the input SQUID input circuit, as mentioned in section 4.3.2. It was not clear at the time of measurement, due to an unknown change in the output file of the Spectrum analyzer. It was later discovered that the output units from the Agilent 89410A had changed from Linear $(\mathrm{V}/\sqrt{\mathrm{Hz}})$ to quadratic $(\mathrm{V}^2/\mathrm{Hz})$ at service, which accidentally resulted in lower current noise values, and was not questioned at the time. However, all the plots given above and below have now been corrected to take the correct output values from the spectrum analyzer into account.

One major difficulty during the measurements was that the modulation depth of the two SQUIDs sometimes decreased to a constant[3] value which was roughly 1/10th of the original value. This was most likely caused by a bad contact in series array wiring or a ground contact in the input SQUID lines, but it was never fully understood, nor did we find the explicit reason for it. However, this only happened during the reported measurements 175 and 177. The problem occurred randomly, and once the modulation depth was reduced, no method was found to recover the modulation back to the original value.

Looking at Figures 40, 41, 42 and 43, there is some clearly visible $1/f$ noise. However, the cause for high $1/f$-noise seemed to have vanished after run 177, when the sample stage was modified to fit the large X-Array TES chip on it. The final SQUID noise measurement, see figure 43, gave a reasonable result of white noise level $11\,\mathrm{pA}/\sqrt{\mathrm{Hz}}$ with $1/f$-noise visible below $100\,\mathrm{Hz}$. Such SQUID can be effectively used for TES readout. However, lower noise floor is preferred.

---

[3]Constant value in the sense that it was independent of the measurement/cooldown.
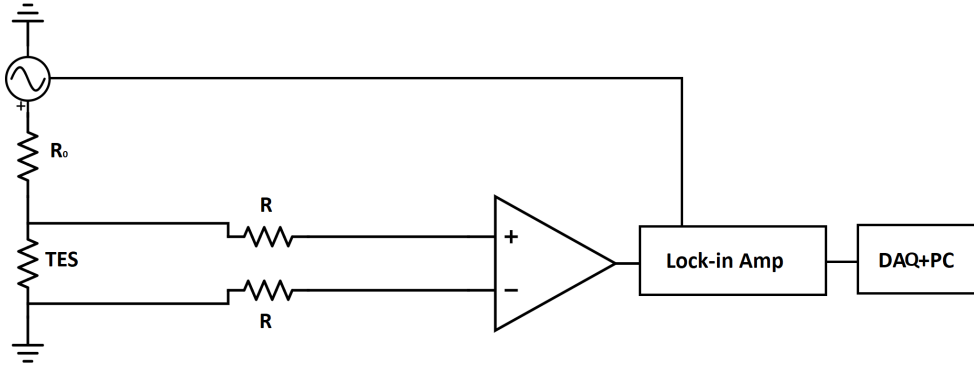
Figure 44. The measurement setup for T_c measurements of TESs. An ac current is applied through the TES and the voltage across is measured at the same frequency versus bath temperature.

5 TES measurements, analysis and results

5.1 Transition temperature

5.1.1 Transition temperature measurement

The first properties to measure for a TES are the transition temperature and the normal state resistance, which are found in the same measurement. The resistance of the TES is measured as a function of the sample stage temperature. This measurement needs to be done slow enough so that the temperature of the stage is the same as the temperature of the thin film TES on the TES array chip. The TES resistance is measured in the four probe configuration. The circuit can be seen in Figure 44, where an ac signal is applied from a Stanford lock-in amplifier through a bias resistor $R_0 = 9974\,\Omega$, and the voltage across the TES is amplified with Ithaco 1201 low noise preamplifier and then measured with the lock in amplifier. The lock-in measures the in-phase ac voltage across the sample, V_m, from which the resistance of the sample $R_S = \frac{V_m}{I_b} = \frac{V_m}{V_{out}R_0}$ can be calculated. The lock-in outputs a signal between -10 and 10 V corresponding to the percentage of the measurement range, and the signal is read by the DAQ-card and PC.

For a typical measurement the lock-in settings were: 1 s time constant, 200 μV sensitivity, 17.662 Hz, 0.25 V sinusoidal ac voltage. For the preamplifier following settings were used, gain 1000, high pass filter 0.1 Hz and low pass filter 1 kHz, AC-

AC coupling. For two pixels, the sensitivity range of lock-in had to be increased due to the output was hitting the $10\,\mathrm{V}$ limit sometimes when the TES was in normal state. For BY16 and BY30 $500\,\mu\mathrm{V}$ sensitivity was used.

The transition of one pixel was measured by the SQUID readout, see Figure 14. The measurement method was to bias the TES pixel with bias current generated by $5.5\,\mathrm{mV}$ dc bias voltage input to the same $R_0 = 9974\,\Omega$ bias resistor. The bias voltage, the output of the SQUID readout and the bath temperature were measured. The bias voltage is measured only to find if there is drift in the bias voltage supply, which was $\pm 10\,\mu\mathrm{V}$.

5.1.2   Transition temperature analysis

The measured transition temperature curves are collected in Figure 45, where it can be seen that there are two groups of transition temperatures. The positions of the measured pixels on the array chip are shown in Figure 46. The transition temperature of a TES pixel is defined here as the resistance of the TES film is half of the normal state resistance, $R/R_n = 0.5$. However, the transition temperature differences are not related to the pixel size, but rather to the cooldown. Pixels with $T_c \approx 157\,\mathrm{mK}$ were measured during cooldown 186 and the pixels with $T_c \approx 135\,\mathrm{mK}$ during cooldown 188. This shifted T_c could be related to thermal contact differences of the runs. The TES chip is connected to the sample stage by Apiezon N vacuum grease[4], and to better thermalize the chip to the sample stage, low temperature GE varnish[5] is also used to glue the gold platforms on the chip, see Figure 29, onto the sample stage copper platform. However, the effect of thermal cycling on these materials in multiple cooldowns are unknown. The contact between these thermalizing materials and the sample stage and the TES chip might degrade, which would lead to lower bath temperatures needed for the transition temperature to occur.

The shift in the transition temperatures is 15-20 mK. The overall resolution of the TES array would be increased if all the T_cs are similar. Considering only the first group of pixels with measured T_cs around $157\,\mathrm{mK}$, the standard deviation is only $1.5\,\mathrm{mK}$ (pixels AX07, AX11, AY19, AY24 and BY31). If all pixels are considered, the standard deviation becomes $11.9\,\mathrm{mK}$. Similar TES arrays have been measured earlier by Mikko Palosaari [40], where the standard deviation of the T_cs was $7.5\,\mathrm{mK}$. From Table 1 the calculated average transition temperatures and standard deviations here are $T_c = 157.9 \pm 1.5\,\mathrm{mK}$ for the first cooldown and $T_c = 148.1 \pm 11.9\,\mathrm{mK}$ for all the measured pixels (AX04 excluded). The array measured in reference [40] is however a bit different which might also explain why there is more variance in the results. The chip measured in reference [40] had the same dimensions as AX and AY pixels measured in this thesis, but there was a 2 μm gold absorber layer added.

---

[4]http://www.apiezon.com/products/vacuum-greases/n-grease 24.10.2017
[5]https://www.cryospares.co.uk/GE-Low-Temperature-Varnish-p/c5-101.htm 24.10.2017

Figure 47 shows the measured transition temperatures in reference [40]. No definite grouping of T_cs can be observed.

Some pixels have also been measured from this TES array by M. Palosaari. These values are also collected in Figure 46 to show the same position of the measured pixels. The pixels of interest here are in the AX, AY quadrant. T_cs from pixels measured by M. Palosaari are consistently much lower than the pixels measured by the author. One of the pixels show 38.1 mK difference in T_c, 121.3 mK vs. 159.4 mK. The reason for this shift is unknown, but could be due to aging processes or a worse thermal contact between the chip and the sample stage as discussed above. The transition of pixel AX04 was also measured while connected to the SQUID readout, see Figure 48. The T_c is in the same range as the rest of the pixels measured in the cooldown 186.
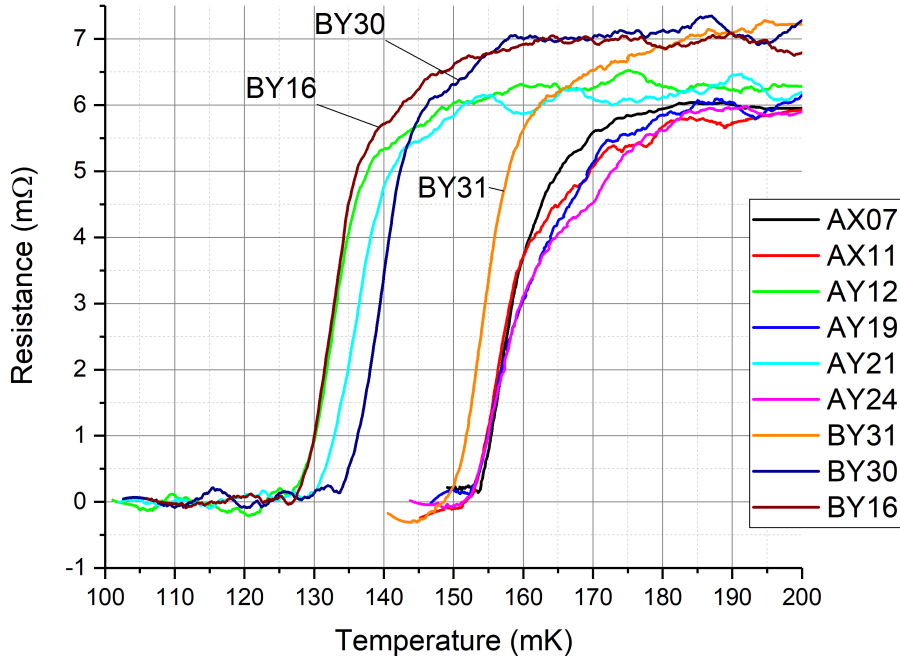
Figure 45. Measured transition temperatures for the TES array studied. Only two different sized pixels were measured, A or B, see Table 1.

The normal state resistances of these pixels are pixel size dependent, see Figure 45. The values are listed in the Table 1, and the $R_n = 5.9 \pm 0.5\,m\Omega$ is the average value and standard deviation for AX, AY pixels and $R_n = 6.8 \pm 0.2\,m\Omega$ for the BY pixels. Pixel AX04 has been excluded from these calculations, having much higher R_n. Its T_c-measurement showed a strange T_c, dependent on the direction of temperature gradient. Different T_c with warming up and cooling down across the

68

Figure 46. Measured transition temperatures mapped on the chip, color coded by measurement. Red pixels were measured during one cooldown, and the orange pixels were measured in another cooldown. Black ones are from reference [40]. The yellow was determined when the pixel was connected to the SQUID.
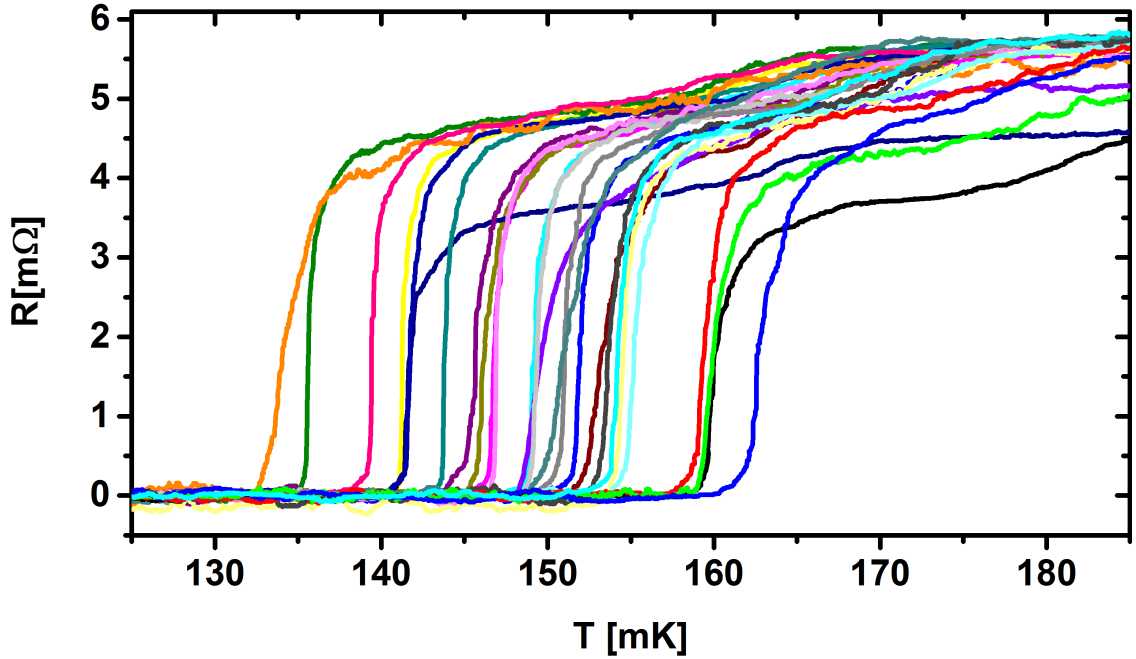
Figure 47. Transition temperatures of a chip from the same wafer. Data from reference [41]. Transitions are more scattered compared to Figure 45.

transition was seen, Figure 48. The measured transition temperature values for the TESs are also collected in the Table 1.

Table 1. Parameters of the measured X-Array TES pixels. T_c and R_n were measured, radii are design values.

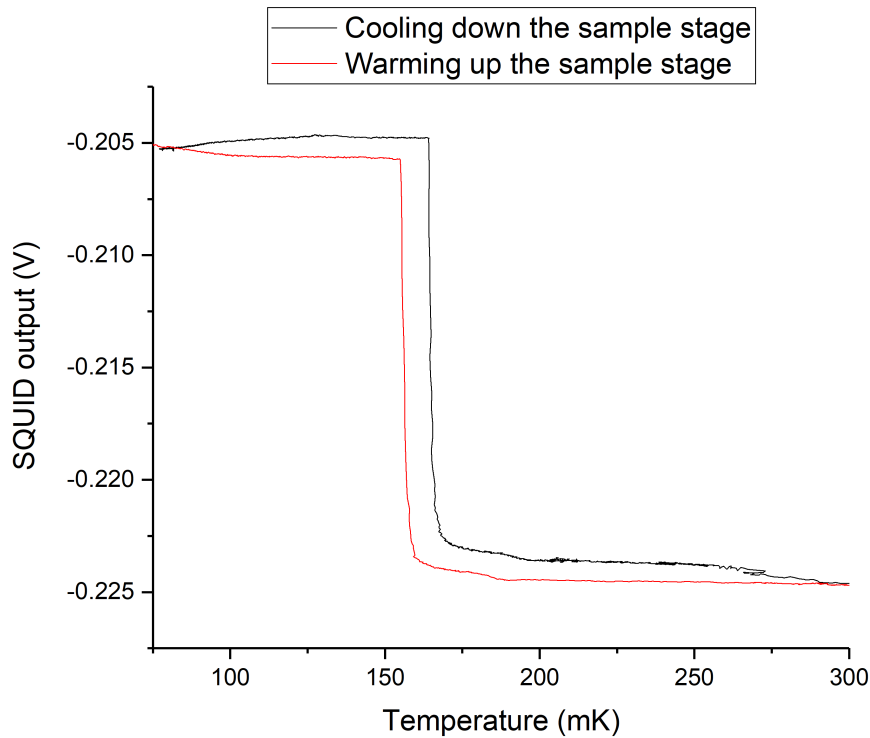| Pixel	T_c [mK]	R_n [mΩ]	Top bias inner r [μm]	Insulator inner r [μm]	TES r [μm]
AX04	156-165	23	35	45	190
AX07	158.4	6.0	35	45	190
AX11	157.8	5.2	35	45	190
AY12	133.5	6.5	35	45	190
AY19	159.4	5.8	35	45	190
AY21	136.6	6.4	35	45	190
AY24	159.0	5.6	35	45	190
BY16	155.1	7.0	25	35	190
BY30	139.9	6.6	25	35	190
BY31	133.4	6.8	25	35	190

Figure 48. The transition of AX04 pixel measured with the SQUID readout chain. The transition is seen as a rapid increase of the output signal of the SQUID readout due to the reduction of resistance at the transition temperature. Hysteretic behaviour is seen as the transition happens at diffferent stage temperatures depending on the sign of the temperature gradient. Black line represents the transition while cooling down and red line represents the transition when warming up.

5.2 Probe current dependency on T_c

One of the measurements was to find out how probing current affects the transition temperature of the TES. The measurement was carried out with pixel AY12 as a T_c measurement, see 5.1.1, and the only variable in the system was the probing current. The bath temperature was lowered until the TES turned superconductive, and temperature was then increased until the TES was fully in the normal state. This was repeated with multiple different probing currents ranging 7-75 μA, see Figure 49. We see that the transition moves down with increasing probe current, by a few mK. The observed shift is approximately consistent with $\beta = \frac{I_0}{R_0} \frac{\partial R}{\partial I}\big|_{T_0} \approx 1$. No hysteresis was seen.
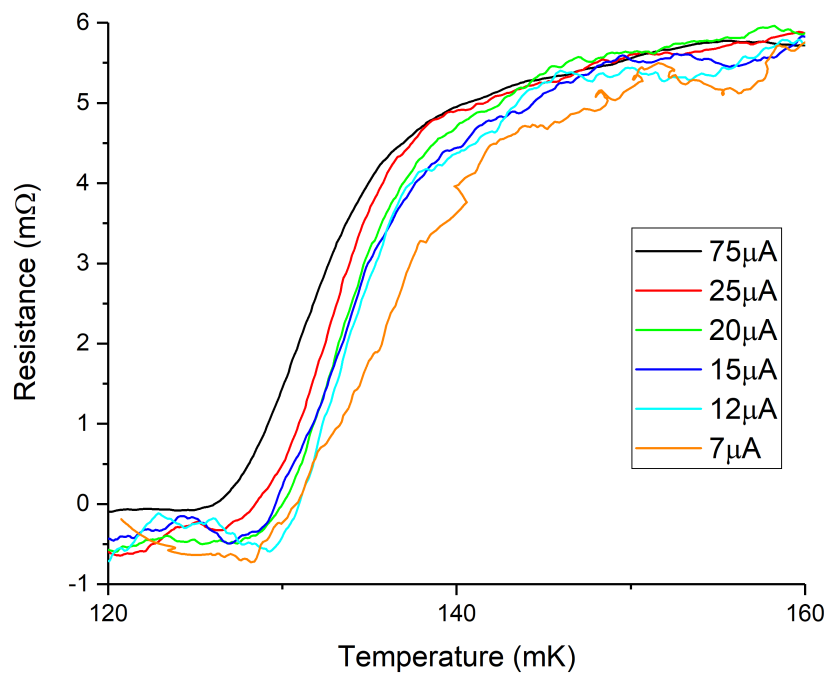
Figure 49. The probing current dependency on TES transition temperature (pixel AY12). Higher probing current shifts the T_c down, as predicted by a finite β.

5.3 Shunt resistor in the SQUID input circuit

The shunt resistor is an important part of the measurement circuit of the TES characterization, see Figure 14. Its measurement was carried out by a delta pulse method, see Figure 50 for circuit diagram, in order to accurately measure a very small resistance value. The delta pulse method is a similar measurement to any four probe resistance measurement, but the probing current is applied in fast pulses rather than having a constant current, hence the name delta pulse method. A square current pulse of duration $110\,\mu s$ with $20\,ms$ delay between pulses is produced by the current source, and the nanovoltmeter measures the voltage differential across the resistor. The Keithley 6221 dc and ac current source and the Keithley 2182A nanovoltmeter are connected by a linking cable, and the current source calculates the resistance value measured by the pulse on its screen.

The measurement was done at multiple temperatures, see Figure 51, to find out if there is some temperature dependency of the shunt resistor at low temperatures. For each temperature and probing current combination, the pulses were started, and the temperature was left to stabilize for 5 minutes. Next, the resistance value from Keithley 6221 dc and ac current source was recorded together with the temperature, once every 30 seconds for 10 consecutive times. The average resistance over the temperature scale from $94\,mK$ to $4.2K$ was $R_{shunt} = 229.7\mu\Omega$, and for the measurement range at where the TES parameters ($T = 100-200\,mK$) are determined, the average was $R_{shunt} = 230.1\mu\Omega$, see Figure 52. The lowest probing current run, $1\,mA$ pulses at $94\,mK$, had higher noise than the rest of the measurements, and was not taken into account for the below $200\,mK$ average.

5.4 TES current-voltage characteristics

5.4.1 TES current-voltage measurement

The current voltage characteristics of the TES pixel AX04 were measured at a few different bath temperatures by the measurement circuit shown in Figure 53. A home made rf-voltagebox was used to create increasing voltages by a step function with a step size of $0.000976801\,V$ and possible output multipliers 1x, 2x, and 5x. The rf-voltagebox was powered by car batteries in order to provide a stable power source for it.

The measurement for the IV-characteristics is performed by decreasing the output voltage of the rf-voltagebox step by step and measuring the temperature, output voltage of the rf-voltagebox, and the output voltage of the SQUID chain in FLL. For the measured IV-characteristics at bath temperatures 70, 85, and $89\,mK$ are plotted in Figures 54, 55, and 56, respectively.
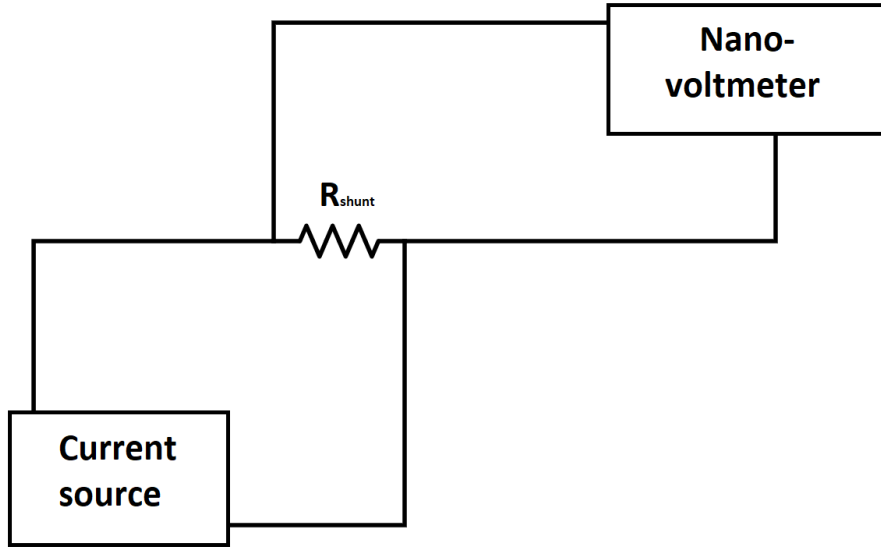
Figure 50. The delta pulse measurement setup. Keithley 6221 dc and ac current source provides current pulses, which are measured by the Keithley 2182A nanovoltmeter to calculate the resistance.

5.4.2 Amplification from the IV-characteristics

The amplification of the SQUID system can be evaluated from the IV-characteristics. With known resistance values of the input circuit, see Figure 14, and with the slopes of the normal state and the superconducting state IV-characteristics determined, the amplification can be calculated by the following equation:

$$G_{normal} = \left(\frac{\mathrm{d}V_{OUT}}{\mathrm{d}V_{IN}}\right)_N \cdot (R_{bias} + R_{wires})\frac{R_s + R_n + R_p}{R_s} \tag{57}$$

for the normal state gain, and

$$G_{superconducting} = \left(\frac{\mathrm{d}V_{OUT}}{\mathrm{d}V_{IN}}\right)_{Sc} \cdot (R_{bias} + R_{wires})\frac{R_s + R_p}{R_s} \tag{58}$$

for the superconductive state. Here R_{bias}, R_{wires}, R_n, R_s, and R_p are the bias resistor resistance, the wiring resistance, the normal state resistance of the TES, the shunt resistance and the parasitic resistance, respectively, see Figure 14. The first factors in the amplification equations are the slopes of the voltage to voltage conversion in the normal or in the superconducting state. The middle factor is the input circuit resistance so the amplification can be transformed to current to voltage amplification. The last is a current division of the load circuit depending on the TES state. With all known resistance values as well as the slopes of the two states, the amplifications from both equations should give the same result. Multiplying this intrinsic SQUID gain with the preamplifier setting amplification value (FA) should give the same amplification that one would get by measuring the modulation of the

Figure 51. Measurement data points for the shunt resistor connected in the TES circuit. Delta pulse method see Figure 50, was used to measure the resistance of the shunt resistor. Different probing currents were used to find the resistances at different temperatures, and averaging over all data points gives $229.7\,\mu\Omega$. It can be seen that one of the results, $1\,\mathrm{mA}$ pulses at $\sim 94\,\mathrm{mK}$ temperature had higher noise than the rest of the results, which indicates that a too low probe current was used.
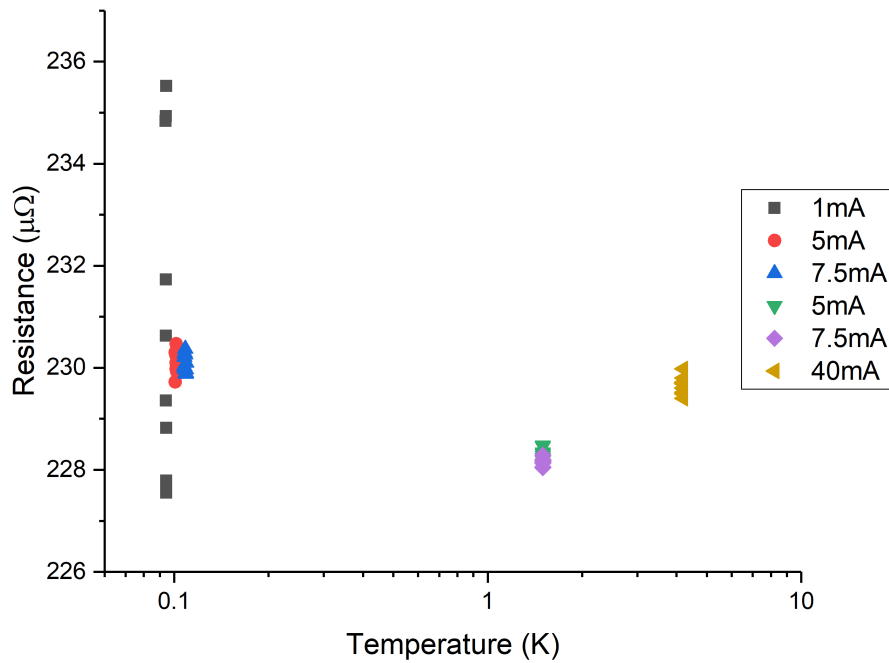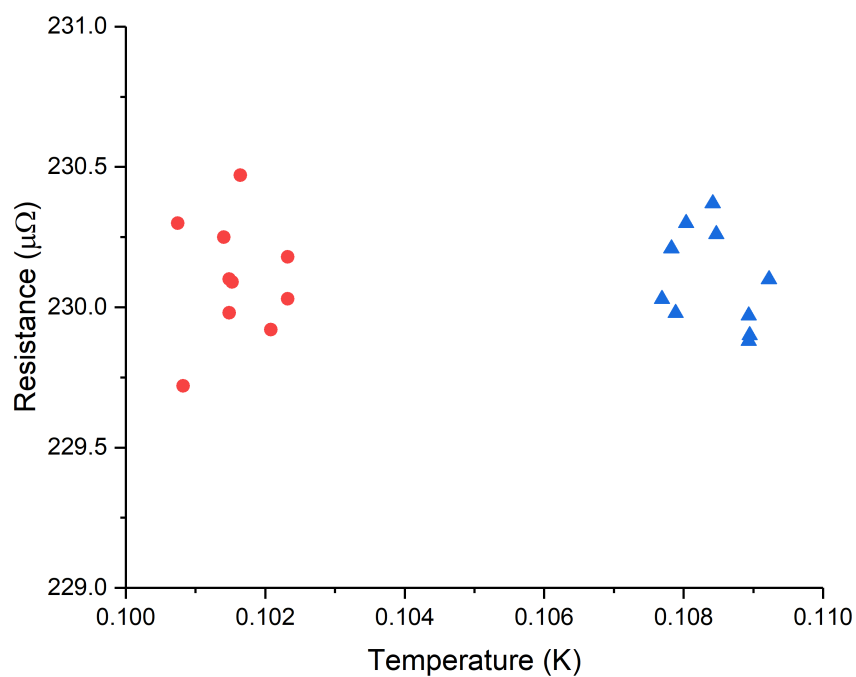
75

Figure 52. Measurement data points for the shunt resistor connected in the TES circuit. Delta pulse method see Figure 50, was used to measure the resistance of the shunt resistor. Two different probing currents with least noise below 200 mK temperature were used to find the resistances. The average of the resistance at close to measuring temperature was 230.1 $\mu\Omega$.
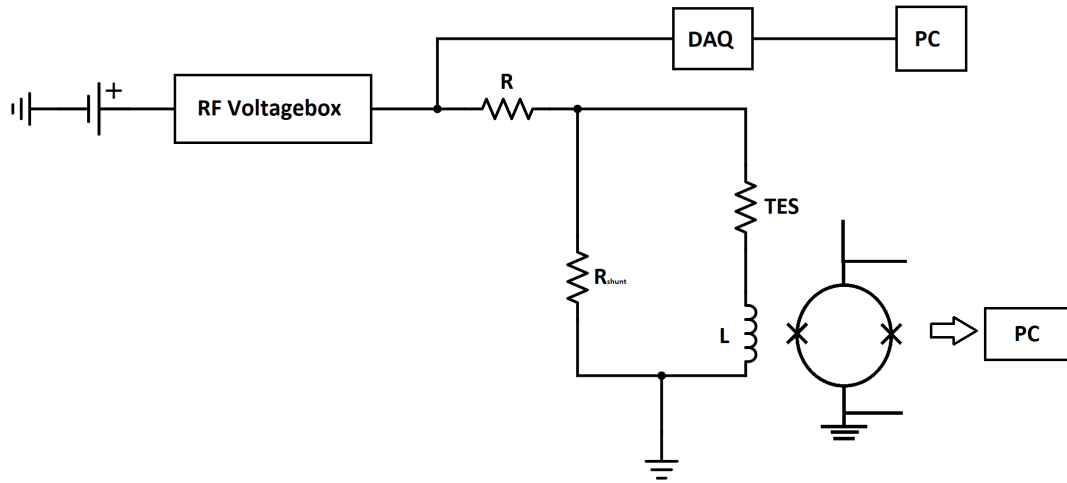
Figure 53. The measurement setup for TES current-voltage characteristics. The RF voltagebox is powered by car batteries, which is used to provide a stable stepped voltage to bias the TES. The varying bias voltage and the output of the SQUID is recorded.

Figure 54. Measured IV-characteristic of a TES (pixel AX04) at 70 mK temperature. The red slope is used in the calculations to find the normal state gain, and the green slope is the same for the superconducting state gain. The process of finding the gain through the IV-curve is explained in the text.
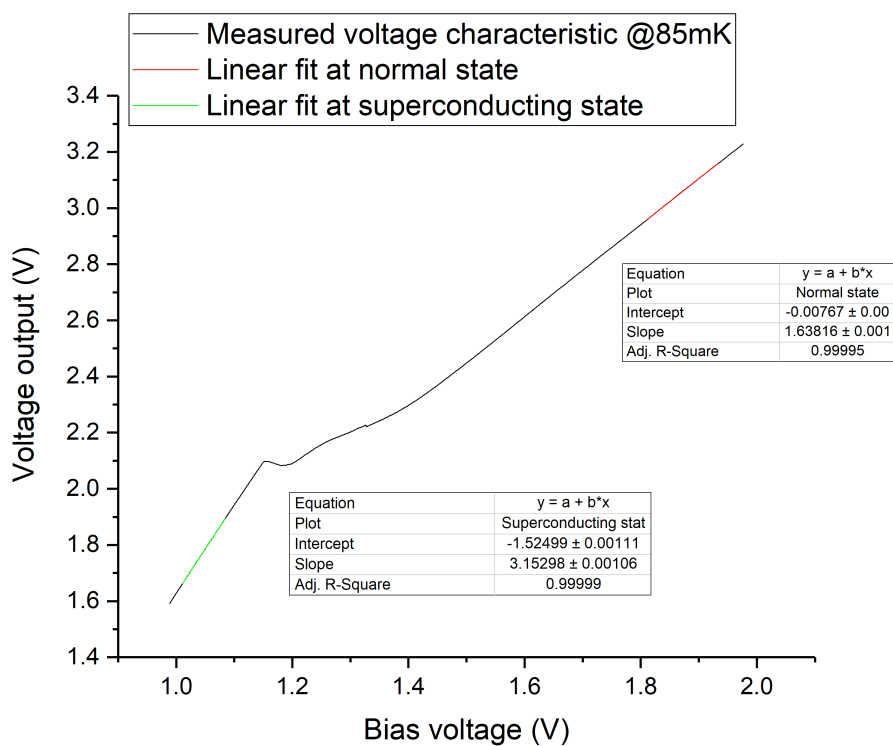
Figure 55. Measured IV-characteristic of a TES (pixel AX04) at 85 mK temperature. The red slope is used in the calculations to find the normal state gain and the green slope is the same for the superconducting state gain. The process of finding the gain through the IV-curve is explained in the text.
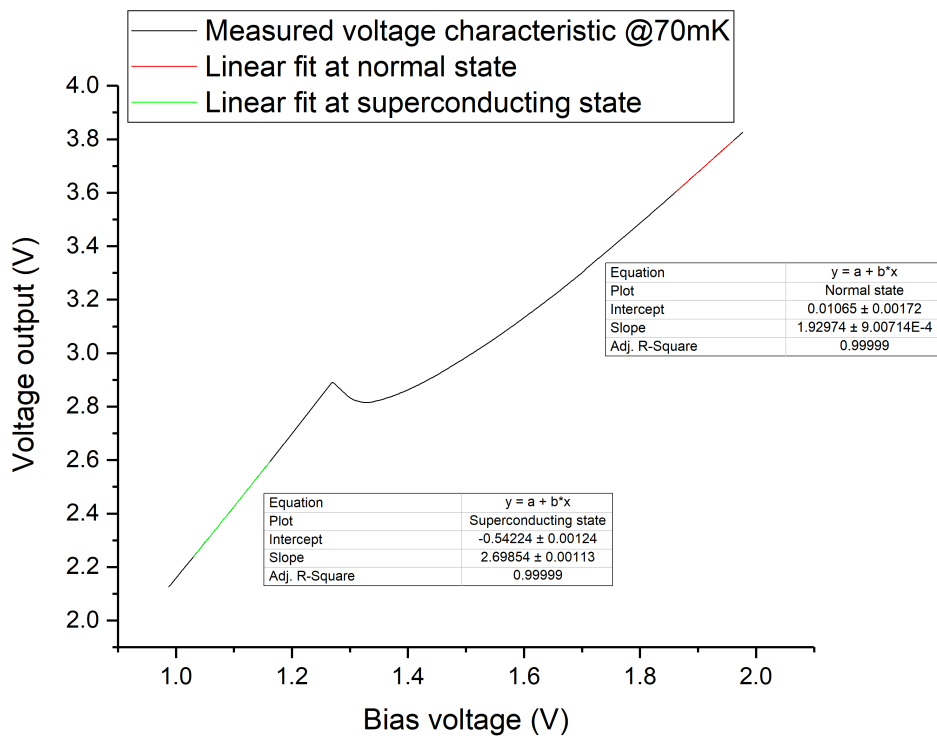
Figure 56. Measured IV-characteristic of a TES (pixel AX04) at 89 mK temperature. The red slope is used in the calculations to find the normal state gain and the green slope is the same for the superconducting state gain. The process of finding the gain through the IV-curve is explained in the text.
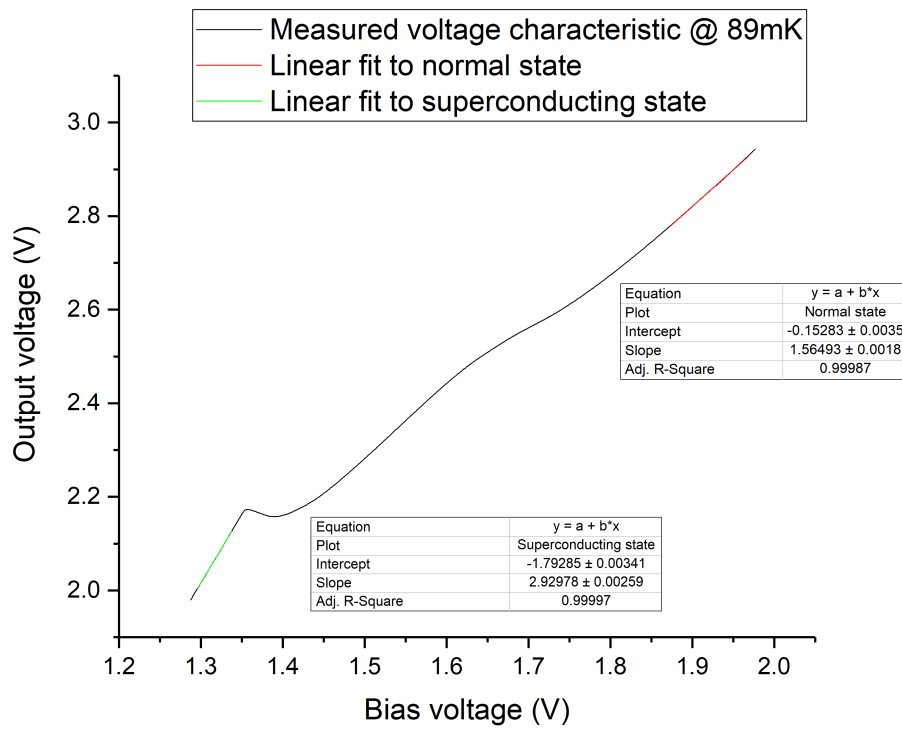
SQUID chain. This method decreases the time needed to setup the measurement if the SQUID FLL is lost, so that there is no need to measure the SQUID modulation and it can be locked immediately. One only needs to measure the IV-characteristics and and calculate the gain with the equations (57) and (58) above.

5.4.3   TES current-voltage analysis

The analysis of the TES IV-characteristics is done in the following way: the measured TES voltage-voltage characteristic is plotted, see Figure 54, and the slopes of the superconducting state and the normal state are found, as shown in section 5.4.2. A dc voltage offset is added to Y such that the superconducting state and the normal state part intercepts at origin. The offset corrected voltage values (TES bias V_{IN} and SQUID chain output V_{OUT}) are now used to find the TES voltage and current.

$$I_{TES} = \frac{V_{OUT}}{G_{normal}} = \frac{V_{OUT}}{G_{superconducting}}, \tag{59}$$

$$V_{TES} = R_s\left(\frac{V_{IN}}{R_{bias} + R_{wires}} - I_{TES}\right) - R_p I_{TES}. \tag{60}$$

The obtained AX04 pixel IV-characteristics are all plotted at three different temperatures in Figure 57. For a normal behaviour of IV-characteristics, the slopes of IV-characteristics measured at different T_{bath} at high bias voltages align, see Figure 58. This might be the case for Figure 57, if the measurement range would have been higher, and the IV-characteristics could have been measured to higher bias voltages. Another factor to consider is that the IV-characteristics has a region of negative differential conductance at low bias voltages, when the TES is in transition, see Figure 58. This behaviour is only slightly visible in our measurements, comparing Figures 57 and 58. The transitions should start with higher bias voltages for lower temperatures, but it is hard to say if 85 mK (red) or 89 mK (blue) transition starts earlier. But it is clear that the 70 mK (black) starts at the highest bias voltage.

5.5   TES noise

The same TES pixel (AX04) was measured at different bias voltages, and the measured noise spectra, together with the SQUID noise floor measured at 620 mK, is shown in Figure 59. The measurement circuit is again shown in Figure 14. The measurement was done by applying a constant bias voltage into the TES input circuit, and then measuring the noise from the SQUID output by the Agilent 89410A Spectrum Analyzer. The measurements were done at six different bias points, the fully superconducting state (black), three different bias values at transition (pink, blue and red), and two at the fully normal state (green and yellow). These noise
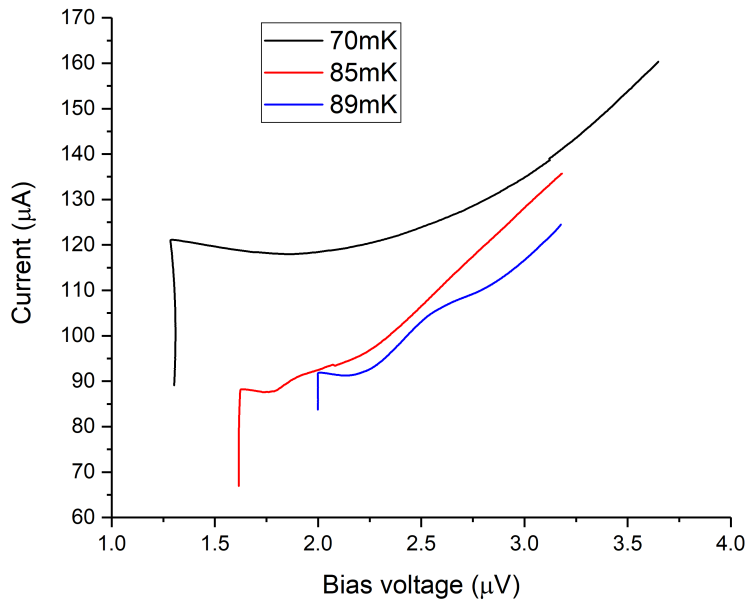
Figure 57. Measured TES IV-characteristics at three bath temperatures. There is noticeable difference between the 70 mK and the two other curves, since the 70 mK curve does not show peaking before the minimum. Also the high bias slope in the fully normal state might not align completely between the 70 mK and 89 mK results. The pixel was from the same chip as the one measured in this work.

measurements were carried out on two different days, hence the two different bath temperatures for these measurements.

When the bias voltage is low enough the TES is in the superconducting state and the noise floor of the circuit can be seen, black line in Figure 59. This noise is dominated by the Johnson noise of the shunt resistor. By increasing the bias voltage until the TES is in its transition, the noise levels rise (pink, blue, and red lines). This rise happens because in transition, the TES is now sensitive to thermal fluctuation noise. By still increasing the bias voltage until the TES is fully in the normal state, the noise levels decrease from the transition values, green and yellow lines. Now the noise is dominated by the TES Johnson noise. If the SQUID noise is well known and the noise floor is insignificant compared to the TES noise, the TES noise can be used with the complex impedance values to analyze the TES behaviour with more advanced thermal models [27, 28]. From Figure 59 it can be seen that the SQUID noise is insignificant in the region of interest below 10 kHz. The fact that the SQUID noise is higher than the TES noise measurement above 10 kHz is somewhat puzzling. One reason for this discrepancy is the high temperature of the SQUID noise measurement.
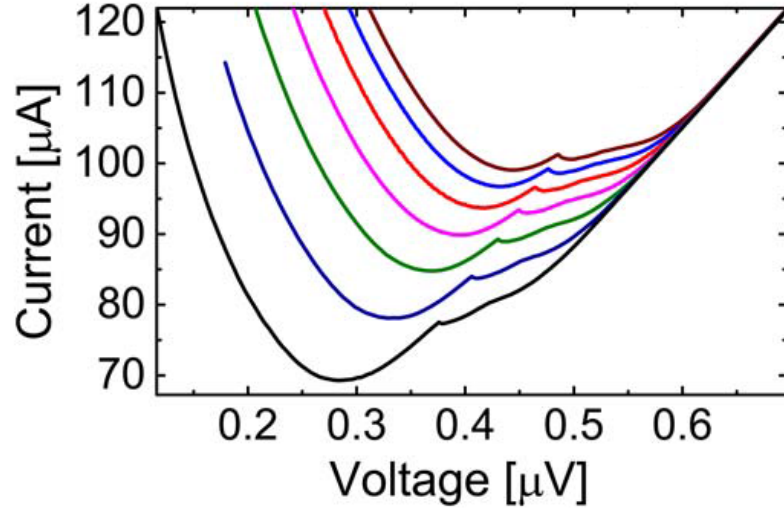
Figure 58. Collection of IV characteristics at different bath temperatures ranging from 70 (brown) to 130 mK (black), from reference [40]. All of the measurements show a peak on the right side of the current minima.

In Figure 60, the cut off frequency of the input circuit (Figure 14) can be found, and from this some circuit parameters could be evaluated. The fitting function for these cut off frequencies was

$$y = \frac{y_0}{\sqrt{1 + \frac{x^2}{A^2}}}, \tag{61}$$

where y_0 is the white noise level, and $A = \frac{2\pi}{\tau} = f_c$. Estimating wiring capacitance to be below $0.2\,\mathrm{nF}$, leads to cut-off frequencies above $f_c = 1\,\Omega/(2\pi \cdot 0.2\,\mathrm{nF}) \approx 800\,\mathrm{MHz}$ with resistances at $1\,\Omega$ and below, hence the cutoff frequency is determined by the τ_{LR}. With the input coil inductance estimated to be $17\,\mathrm{nH}$, the circuit resistances of the normal and superconducting states could be evaluated. For the fully superconducting state (black line in Figure 60), thus results in $R_{circuit} = 177\,\mu\Omega$ and the fully normal state (blue line) results in $R_{circuit} = 360\,\mu\Omega$. However, these values are much below the normal state resistance of the TES, $\approx 23\,\mathrm{m}\Omega$. Thus, L_{IN} could be much higher according to this data. Better measurement of L_{IN} is again highly desirable.
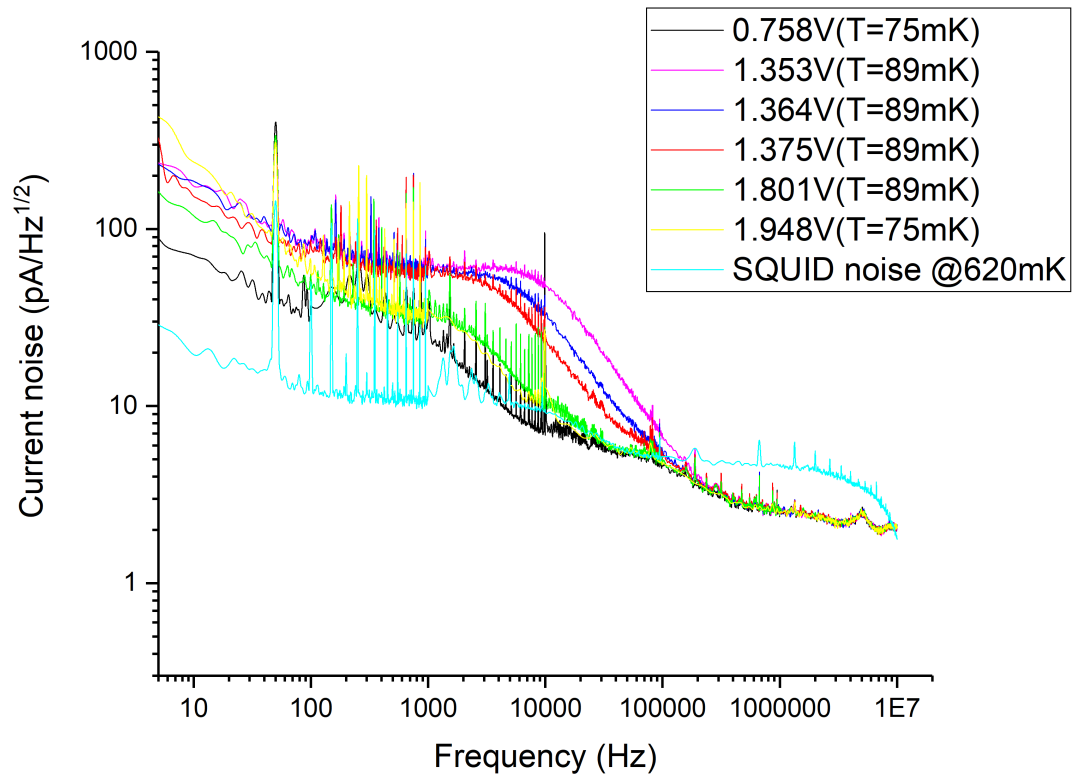
Figure 59. Measured TES (AX04) noise spectra at different bias voltages. The peaks in 0.1-10 kHz are interference due to an errant extra connection to the DAQ-card. These are only visible in some spectra, as the source was found and the extra connection remove for remaining measurements. The overall noise is increased when the TES is at its transition due to responsivity increase.

Inside the figure, the fit parameter boxes read:

Equation	y=62/sqrt(1+(x/A)^2)
Plot	Current noise,1.364V
A	6280.03587 ± 64.7069
Adj. R-Square	0.82699

Equation	y=35/sqrt(1+(x/A)^2)
Plot	Current noise,1.801V
A	2867.36336 ± 82.1231
Adj. R-Square	0.41267

Equation	y=35/sqrt(1+(x/A)^2)
Plot	Current noise,0.758V
A	1411.89237 ± 27.857
Adj. R-Square	0.66239

Legend:
- 0.758V(T=75mK)
- Nonlinear fit to 0.758V TES bias
- 1.364V(T=89mK)
- Nonlinear fit to 1.364V TES bias
- 1.801V(T=89mK)
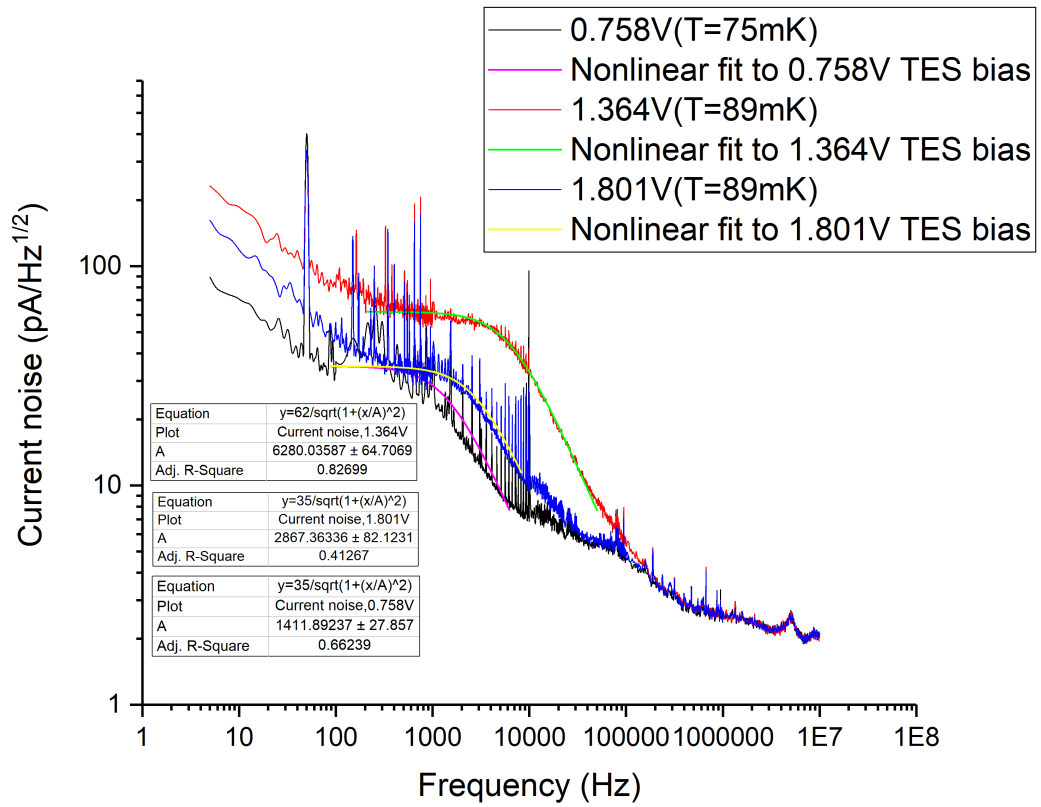- Nonlinear fit to 1.801V TES bias

Figure 60. Measured TES noise spectra with nonlinear fits to find the cut off frequencies at different bias voltages. Fitting function $y = \dfrac{y_0}{\sqrt{1+\frac{x^2}{A^2}}}$ was used, where y_0 is the white noise level, and $A = \frac{2\pi}{\tau} = f_c$.

5.6 Problems and unknowns

5.6.1 Temperature stability and limits

One of the difficulties during the measurements was that the temperature stabilization method affected the actual measurement, see Figure 61. Two methods were used to stabilize the temperature, during these measurements. First, a hardware solution, TS-530 Temperature controller, see Figure 26. This provided a stable temperature, but proved to alter the temperature reading on the resistance bridge. Figure 61 shows an example of the effect of the connection between the temperature controller and the resistance bridge. Even if a software based solution is used to actually control the temperature the temperature readout is altered if the controller is just connected to the resistance bridge.

The transition varies as much as 70 mV simply due to the connection to the PID-controller. This input voltage variation (70 mV) corresponds to 70 μA, see Figure 61, and even higher variation was observed, up to 200 mV. Measurement temperature was 89 mK.
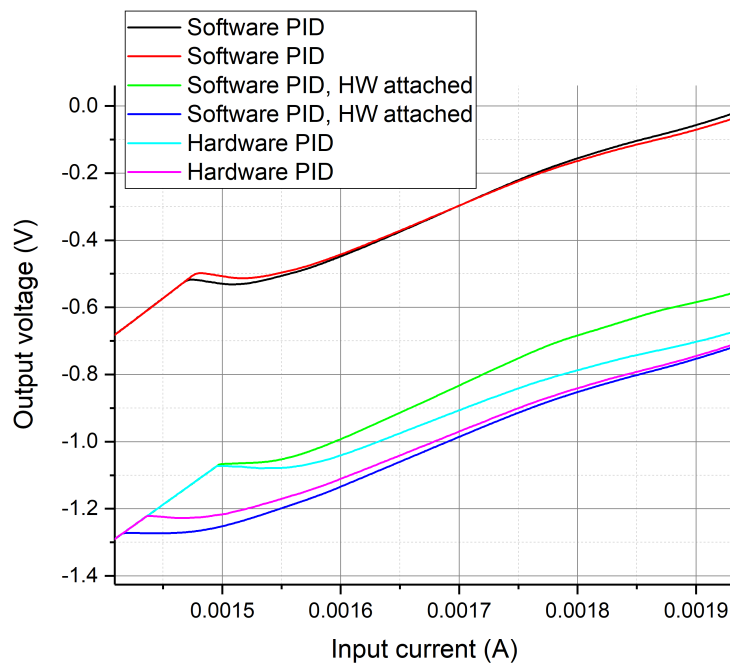

Figure 61. The influence of using the hardware PID solution. The IV-characteristic is shifted to higher input current, which means lower bath temperature for the same pixel. The difference in output voltage is due to different SQUID readout amplification between the two sets of curves.

During some cooldowns, when the measurements lasted for multiple days, the

limits of the dilution refrigerator became apparent. Once the amount of liquid helium in the dewar dropped low enough, the cooling power of the cryostat decreased. This is visible is in Figure 59, where some of the spectra are measured at higher temperatures than the others. Another problem due to the limits of the cryostat was that the still pumping line started leaking, and could not be fixed in the timeframe of this thesis. It was still however possible to cool down to $4.2\,\mathrm{K}$, just by inserting the cryostat into the dewar.

5.6.2 Normal state resistances

One of the problems during the measurements was that the TES that was measured by the SQUID circuit, pixel AX04, did not behave as a textbook pixel would. After the measurement run when the pixel was measured, the cryostat could not reach temperatures below $4.2\,\mathrm{K}$, as explained above, and the normal state resistance of AX04 was measured only at $4.2\,\mathrm{K}$. At the same time another pixel, whose T_c and R_n at transition were known, was measured to find out if and how much the resistance changes from $4.2\,\mathrm{K}$ to just above T_c. The resistances of the two pixels at $4.2\,\mathrm{K}$ with different probing currents have been plotted in Figure 62. Since the value of pixel AY12 is approximately the same, both near the transition as well as at $4.2\,\mathrm{K}$, the pixel AX04 R_n can be approximated to be $23\,\mathrm{m\Omega}$ just above the T_c. This is four times the value of any of the pixels measured, and AX04 can be considered to be bad pixel, to some extent. It was quite unlucky that we managed to measure IV-characteristics and noise, but not the normal state resistance from that pixel before the cryostat problems began.
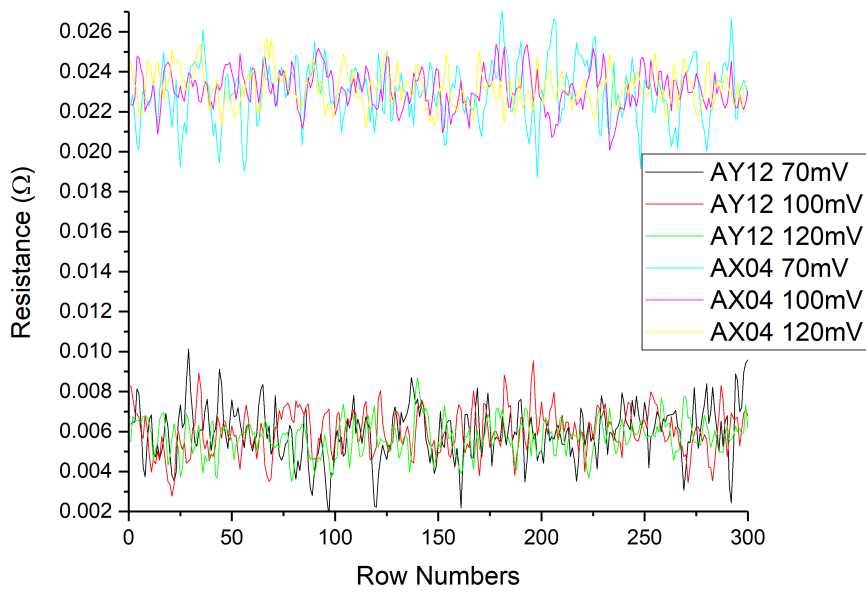
Figure 62. Two pixels measured at $4.2\,\mathrm{K}$ temperature, after the cryostat was unable to cool down to $0.1\,\mathrm{K}$ to measure the T_c of AX04 pixel. The resistance of pixel AY12 is approximately the same at $4.2\,\mathrm{K}$ as well as at just over T_c, $>140\,\mathrm{mK}$. The normal state resistance of pixel AX04 is unknown right above T_c, but considering the change of resistance for pixel AY12, it can be estimated to be in the $23\,\mathrm{m\Omega}$ range.

6 Conclusions

Even though there were difficulties from the start, unknown design parameters, cooldown problems, valuable knowledge was found from the measurements. The two components of interest, the dc-SQUID and TESs were measured.

To summarize the measurements for the dc-SQUID, the newly installed two-stage SQUID setup was characterized by measuring its modulation behaviour, see section 4.1. The mutual inductances were measured, and the amplification factor for the whole SQUID chain was determined, see section 4.2. The determined amplification factors are off course dependent on the preamplifier settings, but for the settings detailed in the section 4.2, the preamplifier factors ended up to be 1533.6 for FA-mode, 189.2 for IV-mode, and 22.5 for DIR-mode into a $1\,\text{M}\Omega$ load. The typical current-to-voltage amplification values for the measurements were $1\text{-}3\cdot10^6\,\text{V/A}$ for the FA-mode, depending on the modulation of the measurement. In general, the SQUID amplification alone, calculated by equation (50) was 700-2000 V/A. The noise characteristics were also measured, and some $1/f$-noise is visible in all of the measurements. Also a possible ground contact made the measurements prior to run 185 have a higher noise floor due to Johnson noise of the resistance into the ground. The noise floors of the input SQUID and series array are approximately $10.7\,\text{pA}/\sqrt{\text{Hz}}$ for the input SQUID and $4.8\,\text{pA}/\sqrt{\text{Hz}}$, but those were determined at $620\,\text{mK}$ so lower values are expected in the future.

The transition temperature measurements were done on multiple pixels and have been collected in Table 1. The normal state resistances were $R_n = 5.9 \pm 0.5\,\text{m}\Omega$ for the size A pixels, and $R_n = 6.8 \pm 0.2\,\text{m}\Omega$ for the size B pixels. The transition temperatures were placed in two groups, with about $20\,\text{mK}$ shift in temperature between the two measurements. The probable reason for this is that the thermal contact between the sample stage and the TES chip degraded. The transition temperatures for the higher T_c group are $T_c = 157.9 \pm 1.5\,\text{mK}$ and for the total group $T_c = 148.1 \pm 11.9\,\text{mK}$. The probing current effect on the transition temperature was also studied with one pixel (AY12), and the result was consistent with known values of the dependence of transition current (β parameter). The transition temperature for one pixel (AX04) was measured by the SQUID readout, fitting the other T_cs in the cooldown. The normal state resistance of this pixel was measured later and shown to have approximately four times higher R_n to other pixels of same size.

Also the TES IV-characteristic was measured for one pixel, and this measurement needed to have a known and very small shunt resistor $R_s = 230.1\,\mu\Omega$. The results

for the IV-characteristics were however somewhat lackluster, due to the pixel having odd behaviour. This is most likely due to the pixel having some non-ideality, which could be argued from the much higher normal state resistance compared to the rest of the measured pixels.

The last measurements were the noise of the TES, and it was seen that the noise behaves as was to be expected, and the SQUID noise floor can be evaluated to be insignificant in the frequency region of interest.

The overall conclusion is that valuable data and knowledge was gained from the newly installed system and the X-Array TESs, but due to problems during the measurements and lack of certain design parameters, more measurements are needed to fully understand some behaviour seen in the measurements.

References

[1] H. K. Onnes. The superconductivity of mercury. Comm. Phys. Lab. Univ. Leiden, 120b, 122b, 124c, 1911.

[2] C. Enss. *Cryogenic Particle Detection*, volume 99. Springer-Verlag Berlin Heidelberg, 2005.

[3] J. N. Ullom and D. A. Bennett. Review of superconducting transition-edge sensors for x-ray and gamma-ray spectroscopy. *Superconductor Science and Technology*, 28(084003), 2015.

[4] R. den Hartog et al. Low-noise readout of tes deterctors with baseband feedback frequency domain multiplexing. *Journal of Low Temperature Physics*, 167:652–657, 2012.

[5] R. den Hartog et al. Requirements for the detectors and read-out of athena x-ifu. Proc. SPIE 9144, Space Telescopes and Instrumentation, 2014. Ultraviolet to Gamma Ray, 91445Q.

[6] B. D. Josephson. Possible new effects in superconductive tunneling*. *Physics Letters*, 1:251–253, 1962.

[7] D. Drung. High-tc and low-tc dc squid electronics. *Superconductor Science and Technology*, 16:1320–1336, 2003.

[8] T. S. Lee et al. High-tc squid microscope for room temperature samples. *IEEE Trans Applied superconductivity*, 7:3147–3150, 1997.

[9] A. I. Ahonen. 122-channel squid instrument for investigating the magnetic signals from the human brain. *Physica Scripta*, 49:198–205, 1993.

[10] R. P. Welty. *Integrated SQUID Array Amplifiers*. PhD thesis, University of Colorado, 1995.

[11] K.D Irwin and M. E. Huber. Squid operational amplifier. *IEEE Trans Applied Superconductivity*, 11:1265–1270, 2001.

[12] J. L. Walsh. A closed set of normal orthogonal functions. *American Journal of Mathematics*, 45:5–24, 1923.

[13] K.D. Irwin et al. Self-biasing cryogenic particle detectors utilizing electrothermal feedback and a squid readout. *IEEE Trans Applied superconductivity*, 5:2690–2693, 1995.

[14] K.D. Irwin and K. W. Lehnert. Microware squid multiplexer. *Applied Physics Letters*, 85:2107–9, 2004.

[15] M. Tinkham. *Inrtoduction to superconductivity.* Dover publications, Inc, 2 edition, 1975,1996.

[16] J. R. Schrieffer. *Theory of superconductivity.* J. R. Schrieffer, 2 edition, 1964,1999.

[17] T. van Duzer and C. W. Turner. *Principles of superconductive devices and circuits.* Prentice Hall PTR, 1999.

[18] J. Clarke and A. I. Braginski. *The SQUID Handbook, volume 1: Fundamentals and Technology of SQUIDs and SQUID systems.* Wiley-VCH, 1 edition, 2006.

[19] H. B. Callen and T. A. Welton. Irreversibility and generalized noise*. *Physical Review*, 83:34–40, 1951.

[20] R. Kubo. Statistical-mechanical theory of irreversible processes. i. general theory and simple applications to magnetic and conduction problems. *Journal of the Physica Society of Japan*, 12:570–586, 1957.

[21] T. T. Heikkilä. *The Physics of Nanoelectronics: Transport and Fluctuation Phenomena at Low Temperatures.* Oxford University Press, 2013.

[22] S. Lipschutz M. R. Spiegel and J. Liu. *Mathematical Handbook of Formulas and Tables.* The McGraw-Hill companies, 2009.

[23] C. T. Rogers and R. A. Buhrman. Composition of 1/f noise in metal-insulator-metal tunnel junctions. *Physical Review Letters*, 53:1272–1275, 1984.

[24] M. Galeazzi and D. McCammon. Microcalorimeter and bolometer model. *Journal of Applied Physics*, 93:4856–4869, 2003.

[25] M. Lindeman. *Microcalorimetry and the transition-edge sensor.* PhD thesis, University of California, 2000.

[26] I. J. Maasilta. Complex impedance, responsivity and noise of transition-edge sensors: Analytical solutions for two- and three-block thermal models. *AIP Advances*, 2(042110), 2012.

[27] K. Kinnunen. *Studies of Transition-Edge Sensor Physics: Thermal Models and Noise.* PhD thesis, University of Jyväskylä, 2011.

[28] I. J. Maasilta and K. M. Kinnunen. New analysis method for i-v and complex impedance data of transition-edge sensors. AIP conference proceedings 1185:38-41, 2009.

[29] K. D. Irwin et al. Thermal-response time of superconducting transition-edge microcalorimeters. *Journal of Applied Physics*, 83:3978–3985, 1998.

[30] H. F. C. Hoevers et al. Thermal fluctuation noise in a voltage biased superconducting transition edge thermometer. *Journal of Applied Physics*, 77:4422–4424, 2000.

[31] C. M. Knoedler. Phase-slip shot noise contribution to excess noise in superconducting bolometers. *Journal of Applied Physcis*, 54:2773–2776, 1983.

[32] G. Fraser. On the nature of superconducting-to-normal transition in transition edge sensors. *Nuclear Instruments and Methods*, 523:234–245, 2004.

[33] M. Lindeman et al. Percolation model of excess electrical noise in transition-edge sensors. *Nuclear Instruments and Methods*, 559:715–717, 2006.

[34] M. R. J. Palosaari K. M. Kinnunen and I. J. Maasilta. Normal metal-superconductor decoupling as a source of thermal fluctuatioon noise in transition-edge sensors. *Journal of Applied Physics*, 112(034515), 2012.

[35] S. R. Bandler et al. Performance of tes x-ray microcalorimeters with novel absorber design. *Journal of Low Temperature Physics*, 151:400–405, 2008.

[36] F. Pobell. *Matter and methods at low temperatures.* Springer-Verlag Berlin Heidelberg, 3 edition, 1992,2007.

[37] Ari Helenius. Sample stage for ling-cryostat. Special assignement, Univesity of Jyväskylä, 2016.

[38] Boulder Quantum sensors group, NIST. `https://www.nist.gov/pml/quantum-electromagnetics/quantum-sensors` (14.10.2017).

[39] SRON Stichting Ruimte Onderzoek Nederland. `www.sron.nl`(14.10.2017).

[40] M. Palosaari et al. Large 256-pixel x-ray transition-edge sensor arrrays with mo/tiw/cu trilayers. *IEEE Trans Applied superconductivity*, 25:1–4, 2015.

[41] M. Palosaari. *Development and applications of transition-edge sensors.* PhD thesis, University of Jyväskylä, 2015.

[42] K. J. Åström and T. Hågglund. *PID Controllers: Theory, Design and Tuning.* International Society of Automation, 1995.

Appendices

A Derivation of α_{tot}

Assuming small signal limit, the relationship between the three steepness parameters can be evaluated by expanding the TES resistance to first order

$$R(T,I) \cong R_0 + \frac{\partial R}{\partial T}\delta T + \frac{\partial R}{\partial I}\delta I. \tag{62}$$

Using equations (40) and (41), we get

$$\mathrm{d}R = \alpha\frac{R_0}{T_0}\mathrm{d}T + \beta\frac{R_0}{I_0}\mathrm{d}I. \tag{63}$$

Expanding Joule power $P = I^2R$:

$$P(R,I) = P_0 + \frac{\partial P}{\partial R}\delta R + \frac{\partial P}{\partial I}\delta I = P_0 + I_0^2\delta R + 2I_0R_0\delta I \tag{64}$$

$$\Rightarrow \mathrm{d}P = I_0^2\mathrm{d}R + 2I_0R_0\mathrm{d}I = \alpha\frac{P_0}{T_0}\mathrm{d}T + I_0R_0(2+\beta)\mathrm{d}I. \tag{65}$$

from which $\mathrm{d}I$

$$\mathrm{d}I = \frac{\mathrm{d}P - \alpha\frac{P_0}{T_0}\mathrm{d}T}{I_0R_0(2+\beta)}. \tag{66}$$

If we introduce thermal conductances

$$g_0 = nKT_0^{n-1} \tag{67}$$
$$g_S = nKT_S^{n-1} \tag{68}$$

the steady state Joule power can be written as

$$P_0 = K(T_0^n - T_S^n) = \frac{g_0T_0}{n} - \frac{g_ST_S}{n} = \frac{g_0T_0}{n}(1 - \frac{g_ST_s}{g_0T_0}) = \frac{g_0T_0}{n}(1 - \frac{T_S^n}{T_0^n}). \tag{69}$$

By defining a new variable

$$\phi = 1 - \left(\frac{T_s}{T_0}\right)^n, \tag{70}$$

equation (69) gives a useful relation

$$\frac{g_0T_0}{P_0} = \frac{n}{\phi}. \tag{71}$$

Using this relation the Joule power can be expanded also as

$$P_J \approx P_0 + \frac{\partial P_J}{\partial T}\delta T + \frac{\partial P_J}{\partial T_S}\delta T_S$$

$$\Rightarrow \mathrm{d}P_J = nKT_0^{n-1}\mathrm{d}T_0 - nKT_S^{n-1}\mathrm{d}T_S = g_0\mathrm{d}T - g_S\mathrm{d}T_S \tag{72}$$

and combining equations (66) and (72) we get

$$\mathrm{d}I = \frac{(g_0 - \frac{\alpha P_0}{T_0})\mathrm{d}T - g_S\mathrm{d}T_S}{I_0 R_0(2+\beta)}. \tag{73}$$

Inserting this into equation (63) and requiring that the bath temperature T_S is constant we get

$$\mathrm{d}R = (2\alpha + \beta\frac{g_0 T_0}{P_0})\frac{R_0\mathrm{d}T}{T_0(2+\beta)}. \tag{74}$$

Rearranging equation (74), wer finally get the connection between α_{tot}, α and β [27, 28]:

$$\alpha_{tot} = \frac{T_0}{R_0}\frac{\mathrm{d}R}{\mathrm{d}T} = \frac{2\alpha + \frac{n}{\phi}\beta}{2+\beta}. \tag{75}$$
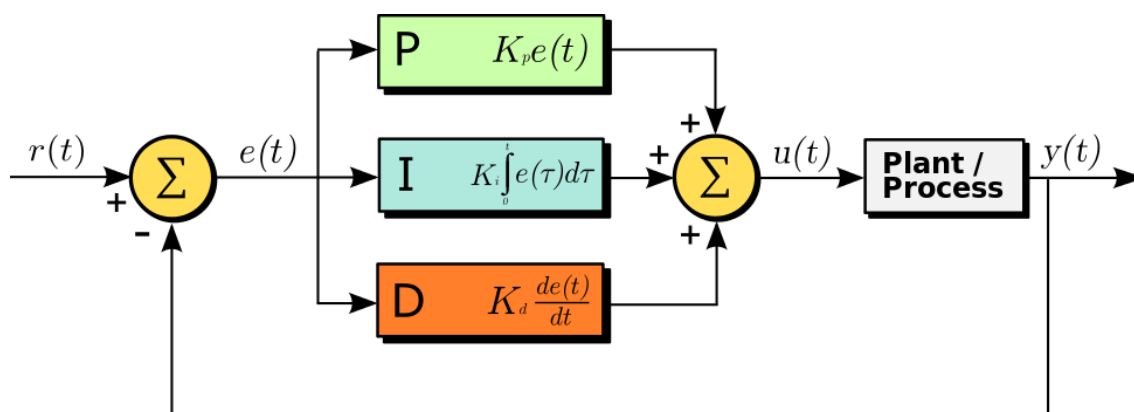
Figure 63. Block diagram of the PID controller. By Arturo Urquizo - http://commons.wikimedia.org/wiki/File:PID.svg, CC BY-SA 3.0, `https:// commons.wikimedia.org/w/index.php?curid=17633925`

B PID controller

Proportional, integral, derivative controller is a component which stabilizes the chosen value by oscillating around the wanted value. Proportional is the error which comes from the value and the measured value. Integral is the error before the "present", i.e. the error accumulated in the past. Derivative can be considered the predicted or future error. It is proportional to the derivative of the current error. One representation of this procedure can be seen in Figure 63, which is then given in mathematical form as[42]:

$$u(t) = K_\mathrm{p}e(t) + K_\mathrm{i} \int_0^t e(\tau)\mathrm{d}\tau + K_\mathrm{d}\frac{\mathrm{d}e(t)}{\mathrm{d}t}, \tag{76}$$

where, $K_\mathrm{p}, K_\mathrm{i}$ and K_d are all positive, representing the proportional, integral and derivative terms respectively. Functions $r(t), e(t), u(t)$ and $y(t)$ are the measured or input signal, the error signal, the error sum and the output signal, respectively. The software for the IV-measurements was built with Labview 2010 version. The changes made for the Labview measurement software were to allow the temperature to be controlled by the software instead of the hardware PID controller. The data is read from the overall data array at the top (indicated by the red arrow), and the temperature value is separated and directed to a value selector (true/false loop on the top right, green arrow). These equations determine the temperature value, since the temperature equation depends on the temperature range.

The integration and derivation times can be input in the program interface (blue arrow). Once the value is calculated and compared, the DAQ assistant outputs
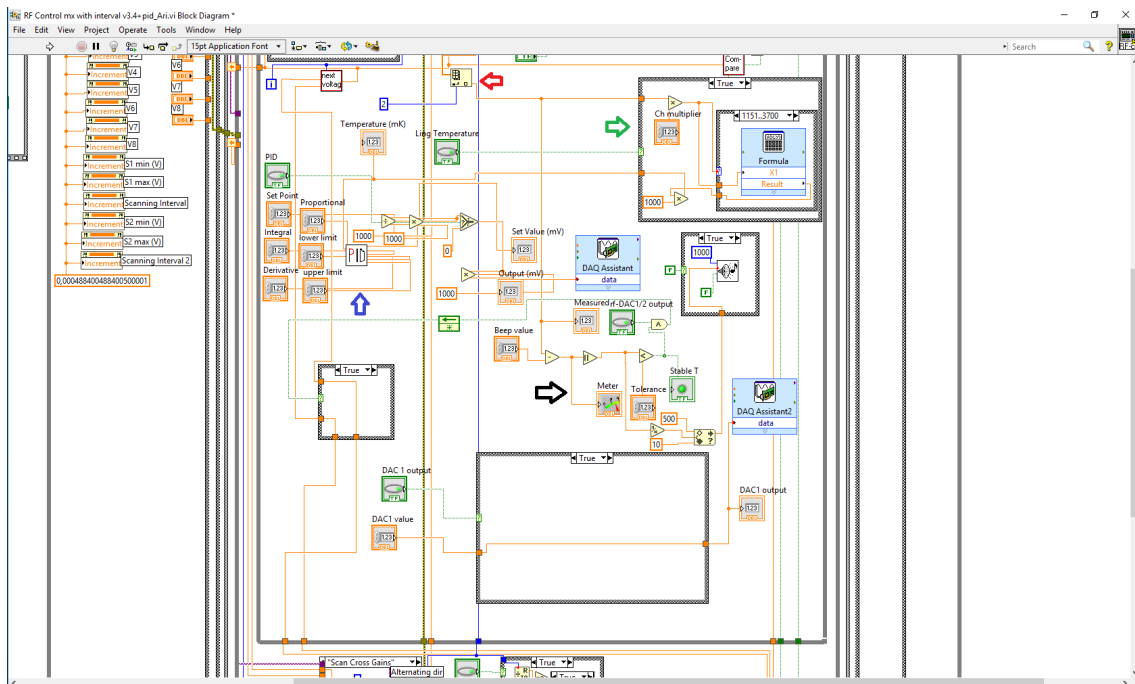
Figure 64. PID changes to the Labview code. Loops in true. Red arrow points to the array that chooses the temperature out of the data, green arrow points to the loop that is used to determine the temperature, blue arrow points to the PID mechanics and black arrow points towards the tolerance check and beeper.

the determined value in mV. This voltage is directed to the sample stage resistor, which heats up the sample stage by a given heating power. The temperature controller works by the same schedule as the rest of the measurement program, which means that there is a certain slowness in the PID system coming outside of the PID circuit. There is also an option to use a tolerance value and a beeper (black arrow), to stop recording data if the value gets too far from the desired temperature.

The second DAC output (DAC 1 output) can be used as the still heater, giving a stable output voltage, which can be manually changed during the measurement. On the false side of the loops, outputs give 0 out, and for the temperature of the sample stage is given as 9999, which means that PID notices this as too big value and cuts off the heating voltage on the next round.
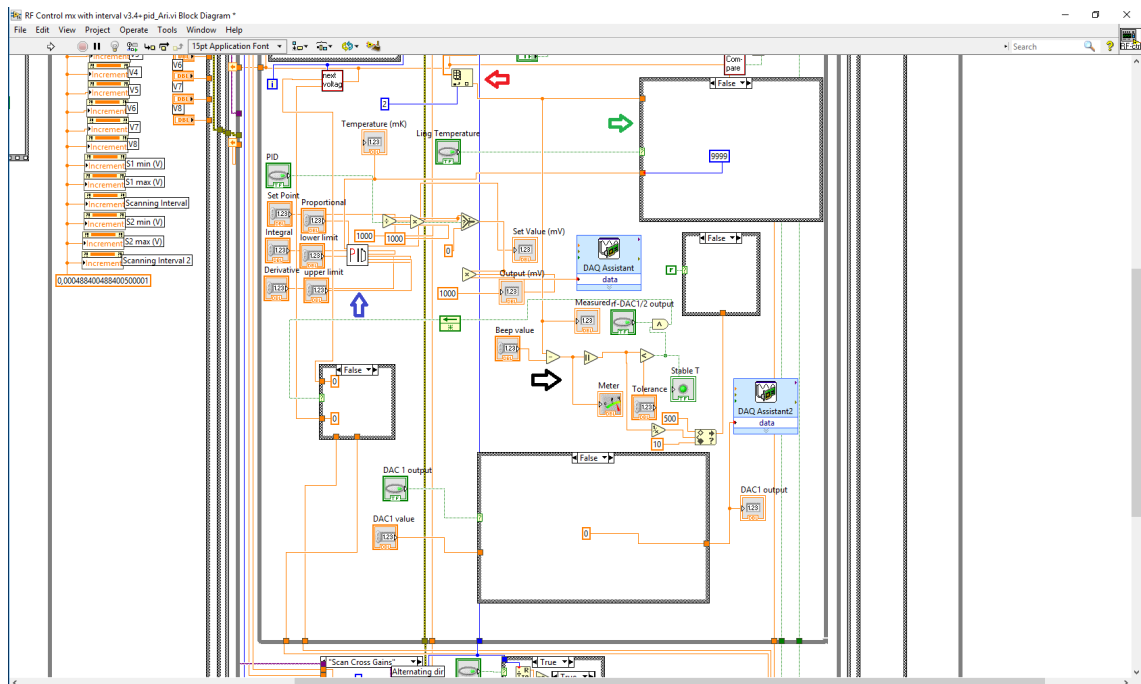
Figure 65. PID changes to the Labview code. Loops in false. Red arrow points to the array that chooses the temperature out of the data, green arrow points to the loop that is used to determine the temperature, blue arrow points to the PID mechanics and black arrow points towards the tolerance check and beeper.